DYNAMIC ANTENNA ARRAY FOR ACTIVE INCOHERENT MILLIMETER-WAVE SENSING

By

Daniel S. Chen

A THESIS

Submitted to
Michigan State University
in partial fulfillment of the requirements
for the degree of

Electrical and Computer Engineering – Master of Science

2021

ABSTRACT

DYNAMIC ANTENNA ARRAY
FOR ACTIVE INCOHERENT MILLIMETER-WAVE SENSING

By

Daniel S. Chen

The need for fast and reliable sensing at millimeter-wave frequencies has been increasing dramatically in recent years for a wide range of applications. Imaging has been of particular interest since the wavelengths at millimeter-wave frequencies provide good resolution and are capable to propagate through obscurants such as smoke, clouds, and clothing with negligible attenuation. While various implementations for millimeter-wave imaging have been developed, the new technique of active incoherent millimeter-wave (AIM) imaging is of particular interest because it solves fundamental limitations inherent in other approaches. Furthermore, AIM enables imaging with significantly fewer elements than phased arrays and costs less than passive imagers. This is enabled by actively transmitting noise signals, allowing the system to capture scene information in the spatial frequency domain.

In this work, I explore the use of array dynamics to further reduce the hardware requirements of AIM imaging by introducing a new degree of freedom in the array design. By dynamically changing the locations of receiving antennas in a sparse array through motions, the spatial frequency domain can be efficiently sampled using as few as two antennas. In this thesis, I demonstrate the use of array dynamics to generate imagery and show a new concept for imageless object identification based on sampling unique spatial frequency features associated with physical shapes of objects. This non-imaging approach further reduces the required number of antennas.

The designed rotational dynamic antenna array operates at 38 GHz and leverages noise transmitting sources as required by the AIM technique. Two receivers are designed with adjustable distance in-between, enabling a sparse linear array to be synthesized. Simulation and experimental measurements using the AIM based rotational dynamic antenna array are discussed for imaging and imageless classification.

TABLE OF CONTENTS

LIST OF TABLES

LIST OF FIGURES

CHAPTER 1

INTRODUCTION

An active incoherent millimeter-wave (AIM) based dynamic antenna array sensing system concept is presented in this work, which can either be designed for imaging applications or imageless detection of sharp-edged structures/objects. Motivations to leverage array dynamics for sensing systems' design are: to further reduce the required antennas (hardware cost) when comparing to conventional imaging approaches that use filled or sparse antenna array design; and to investigate a special use case of identifying sharp-edged structures/objects using specific array dynamics that focuses on acquiring only the desirable information for classification, which requires far less data when comparing to the minimum amount that are required to reconstruct quality imagery. The realization of the presented dynamic antenna array including the hardware design and signal processing is described in detail. Simulations and measurements of simple targets are also presented and discussed for each of the two aforementioned use cases.

1.1 Image-aided Decision Process

Many modern applications rely on image-aided decision processes that can be accomplished either by knowledgeable experts and/or other automated techniques. Image-aided decision processes range from industrial applications that utilize non-destructive evaluation (NDE) or testing (NDT) of defects in materials such as aluminum [7], ceramic tiles [8], and multi-layer materials [9]; to medical applications such as determining abnormalities in human skin [10], detecting breast cancer [11–14], and supporting the multiple stages of healthcare continuum to enable accurate diagnosis, timely prognosis, and subsequent planning for treatment and medication [15]; and remote sensing applications that seek to identify targets of interest from the sensed imagery such as synthetic aperture radar (SAR) [16, 17] or inverse synthetic aperture radar (ISAR) [18]. While decisions made by knowledgeable experts are results of extensive practices and experiences, automated decision processes frequently incorporate image processing classification techniques includ-

ing pattern matching [19] and feature tracking such as recognizing saliency information [20, 21], and structural and/or textural information [22]; leveraging dictionary learning methods to effectively discriminate one class of image pixels from another for polarimetric SAR images [23]; and utilizing deep learning for classification [24]. Furthermore, there are techniques that take advantages of multiple methods in conjunction such as co-processing two images that are sensed with different imaging mechanisms (i.e., infrared and visible spectrum) [25]; using multiple classifiers as in the case for automatic target recognition (ATR) [16]; combining object-based image analysis (OBIA) and convolutional neural networks (CNN) [26] for remote sensing image classification; and classifying medical images using deep learning and handcrafted visual features [27].

1.2 Existing Imaging Approaches

Understanding the importance of imagery and how they affect the decision processes in various disciplines, it is then reasonable to discuss how images can be acquired and formed. Imagery from the aforementioned image-aided decision processes are generally obtained using imaging systems that operate based on different sensing mechanisms with most of them being electromagnetic based systems. Toward the higher segment of the electromagnetic spectrum are systems using optical sensors [12, 28–31]. Residing slightly below the optical frequency band are the infrared based imaging systems where imagery is recovered by sensing the thermally-induced electromagnetic emissions from the scene [10, 32–36]. However, signals in the optical and infrared wavelengths can be significantly attenuated when propagating through media such as smoke, fog, clothing, and other materials commonly found in buildings [37, 38] which can narrow the application to specific or more controlled scenarios. This is one reason that microwave and millimeter-wave frequencies have been used for sensing application as they are more capable to penetrate through the aforementioned obscurants. Furthermore, the frequency bands of microwave and millimeter-wave also ensure reasonable image resolution because their wavelengths are sufficiently small which are similar to optical and infrared bands. These aspects have contributed to the growing interest in using microwave and millimeter-wave systems for imaging [11, 39] and re-

mote sensing [40–42]. One inevitable consideration for designing microwave and millimeter-wave imaging systems is the associated cost which can be related to the required hardware resources. Common microwave and millimeter-wave imaging systems can utilize scanning capabilities via mechanical and/or electrical implementations which can have inherent hardware burdens and significant data acquisition time when comparing to recent metasurface apertures approach [43, 44]. Furthermore, synthesizing a larger aperture to achieve greater reconstructed image resolution requires significant amount of antenna elements which are generally used to form traditional phased arrays and/or focal-plane arrays [45–51].

1.3 Contributions of this Work

In this work, an interferometric imaging-based sensing concept is presented that utilizes a dynamic antenna array with rotational dynamics to sample spatial frequency domain information. The discussed dynamic antenna array sensing technique is built on the recently developed active incoherent millimeter-wave (AIM) imaging works [52–54]. The fundamentals of interferometric imaging theory and the enabling factors that motivate the study of the dynamic antenna array concept are discussed in Chapter 2 along with further discussion on the dynamic antenna array design and implementation. Furthermore, two sensing use cases are presented with discussion of both simulation and measurement-based studies. The first is to utilize a sparse linear antenna array in conjunction with rotational dynamics to acquire images of simple target(s) which will be covered in Chapter 3. This is illustrated in Fig. 1.1 where the objective is to reconstruct the scene, the region highlighted in green. In Chapter 4, a second use case is discussed where the objective is to leverage dynamically acquired sampling points in the spatial frequency domain to identify responses that are particular to sharp edges, which can resemble man-made structures and/or objects in the spatial domain. The identification of sharp edges directly in the spatial frequency domain therefore requires no full image reconstruction which mitigates the usage of the aforementioned computationally expensive methods to examine full image for identification of structures/objects. The proposed imageless spatial frequency domain classification between man-made and non-man-

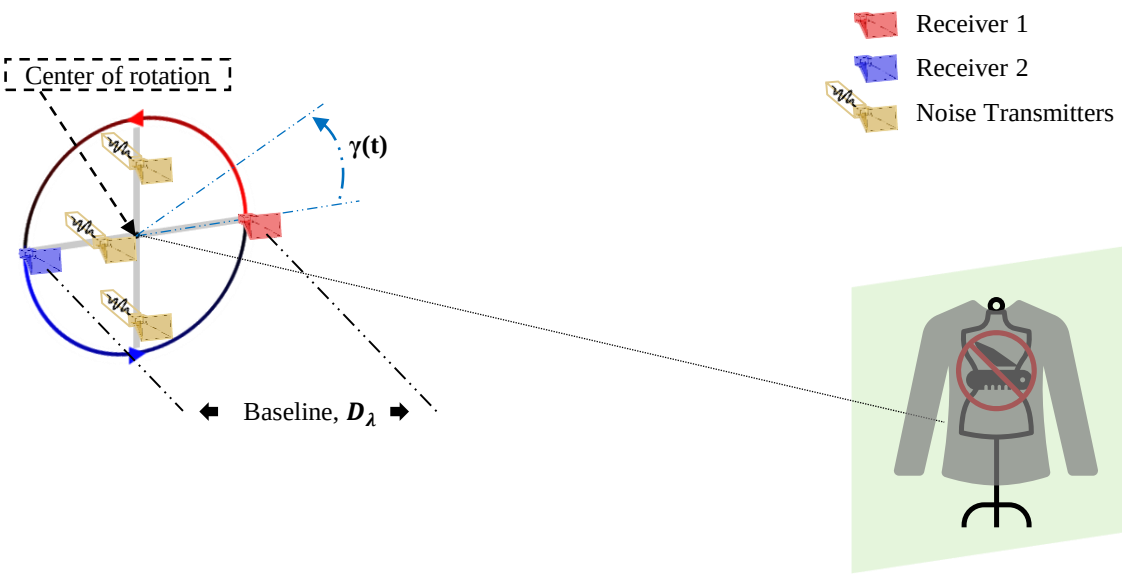

Figure 1.1: Illustration of the rotational dynamic antenna array sensing concept. The proposed dynamic-antenna-array-based sensing concept can be used for imaging applications (i.e., forming an imagery that comprises all detail within the scene as highlighted in green) or imageless detection of structures/objects (i.e., identification of sharp edge related structures/objects existence in the scene highlighted in green without image reconstruction).

made structures/objects therefore requires significantly less sampling points such that an image cannot be possibly reconstructed. Furthermore, for near range application such as contraband detection, where privacy issue is of concerned, a detection method that requires no imagery can prove beneficial.

CHAPTER 2

MOTIVATION OF SPATIAL FREQUENCY SAMPLING USING DYNAMIC ANTENNA ARRAY

In this chapter, the motivation to pursue spatial frequency domain sampling using a dynamic antenna array is discussed in detail. Spatial frequency domain sampling is important for interferometric imaging techniques. The specific sampling function in the spatial frequency domain is highly dependent on a given antenna array design that is affected by the number of elements and the placements of individual antennas. Motivated by this relationship between the antenna array and the sampling function, the concept to leverage array dynamics as an additional antenna array design consideration is discussed. Furthermore, actual experimental setups using the rotational dynamic antenna array are introduced which were used for measurements that will be further discussed in Chapter 3 and Chapter 4.

2.1 Interferometric Imaging

Interferometric imaging was developed for radio astronomy applications where a sparse array, comprising of radiometric receivers, is utilized to generate imagery of the scene of interest instead of using real aperture systems [45, 55]. In general, an interferometric imaging array comprises multiple correlation pairs where the output of the received signals are cross-correlated. Interferometric based imagers do not require mechanically and/or electrically based scanning capability which are commonly implemented in imagers. Another benefit of interferometric imagers is that the image resolution is equivalent to a fully filled phased array assuming both share the same maximum dimension and hence both the physical implementation and operation of an interferometric-based imager can be done more efficiently [37]. Because of these advantages, recent research has been directed to utilizing interferometric imagers for security related applications such as contraband detection as a sparse array implementation can be more cost effective. In this section, the basic theory of interferometric imaging is discussed.

2.1.1 Image Reconstruction and Fourier Domain Sampling

Spatial frequency domain image formation requires that the radiation from the scene of interest is spatially and temporally incoherent for successful image reconstruction per the Van Cittert-Zernike theorem [56, 57]. To better understand how the spatio-temporally incoherent condition is satisfied, interferometric imaging systems can be grouped into to two distinct categories in terms of sensing mode: passive and active. For passive interferometers, the signals maybe intrinsically generated by the scene via thermal means, or by externally generated signals that are unrelated to the passive interferometers [55, 58–60]. However, this type of interferometers encounters sensitivity issues due to extremely low power of radiations from the scene. A common resolution is to implement highly sensitive receiving components with wide bandwidth which are generally not cost effective. Furthermore, the required integration time can be on the order of seconds. The active incoherent millimeter-wave (AIM) technique [52–54] was developed and rigorously studied to counter the aforementioned bottlenecks of passive mode interferometers. The AIM technique implements noise generating sources as transmitters to illuminate the scene of interest with spatio-temporally incoherent signals to satisfy the above-mentioned image reconstruction criteria where the backscattered signals mimic the intrinsic thermal radiation but ensuring received power level with orders of magnitude more compared to that of the passive mode interferometers.

As outlined in Fig. 2.1, the scene intensity is the spatial representation based on the received signal powers at different region of the scene. The scene visibility is the representation of the scene intensity in the spatial frequency domain. The point spread function, also known as the synthesized beam of the imaging systems, is the Fourier transform of the visibility sampling function, or filter, that is synthesized based on the sparse antenna array formation of interferometric imagers which will be discussed later. The collection of spatial frequency samples, or the filtered scene visibility, from the interferometric imagers are then processed using the Fourier transform relationship to obtain reconstructions of the scene intensity.

As briefly introduced above, interferometric imagers sample information of spatial frequencies that are the Fourier-transformed domain of the scene intensity. The scene intensity can

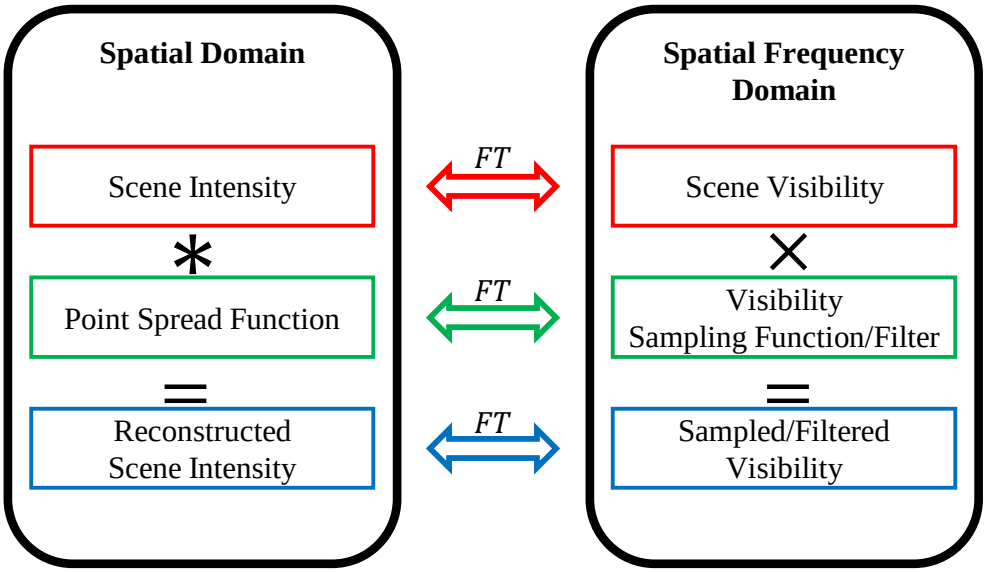

Figure 2.1: Overview of the relationships between spatial and spatial frequency domain. The scene intensity is proportional to the power of signals coming from the scene and is related through Fourier transform to the scene visibility. The point spread function, also known as the synthesized beam of the system, is the Fourier transform of the sampling function synthesized by the interferometric imaging sparse array. The reconstructed scene intensity is the Fourier transform pair of the sampled/filtered scene visibility.

be expressed as $I(\alpha, \beta)$, where $\alpha = \sin\theta\cos\phi$ and $\beta = \sin\theta\sin\phi$ are defined as the directional cosines. The information residing in the spatial frequency domain is the visibility of the scene and commonly expressed as $V(u, v)$, where u and v represent the two dimensions in the spatial frequency domain. This Fourier transformation relationship as introduced in Fig. 2.1 can be represented by

$$V(u,v) = \iint_{-\infty}^{+\infty} I(\alpha,\beta) e^{j2\pi(u\alpha+v\beta)} d\alpha d\beta. \tag{2.1}$$

Suppose that the measured visibility (noted as the sampled/filtered scene visibility in Fig 2.1) is the product between $V(u, v)$ and $S_i(u, v)$ (ideal sampling of the entire spatial frequency domain), then the reconstructed scene intensity, $I_r(\alpha, \beta)$ can be represented by

$$I_r(\alpha,\beta) = \iint_{-\infty}^{+\infty} V(u,v) S_i(u,v) e^{-j2\pi(u\alpha+v\beta)} du dv. \tag{2.2}$$

However, in practice, the visibility cannot be sampled continuously, that is, the introduced formulations above ((2.1) and (2.2)) need to be modified to accommodate the discrete sampling nature. For a given sparse interferometric imaging array that comprises multiple receiving antennas, the cross-correlation of the received signals for a unique antenna pair represents a unique sampling point in the spatial frequency domain where the visibility resides. The uniqueness of an antenna pair is defined by the antenna baseline separation, D, and their orientation with respect to the scene of interest. As shown in Fig. 2.2, a specific baseline separation corresponds to a unique interferometric radiation pattern where the sinusoidal pattern maps to a specific spatial frequency. For the two-dimensional case, the orientation of a given antenna pair within the interferometric imaging array also contributes to the particular spatial frequency information being sampled. Shown as a comparison in Fig. 2.3, the unique interferometer radiation patterns generated are different for the two pairs of antennas sharing same baseline separation at different configurations (i.e., horizontally versus vertically mounted). By configuring the sparse interferometric imaging array with large unique baseline combinations, an adequate number of unique visibility samples can be acquired which enables sufficient reconstruction of the scene intensity via inverse Fourier transform. For the two-dimensional interferometric imaging process, unique u's and v's are related to the result of cross-correlating information received at individual antenna locations that are distributed in the x and y dimensions such that $u = D_x/\lambda \text{ rad}^{-1}$ and $v = D_y/\lambda \text{ rad}^{-1}$, where the quantities D_x and D_y are the projected baselines in the x and y dimensions for a particular antenna pair with wavelength of the received radiation, $\lambda = c/f$. The complete collection of all discretely sampled two-dimensional spatial frequencies is referred as the sampling function that can be represented by

$$S(u,v) = \sum_{n=1}^{N}\sum_{m=1}^{M} \delta(u-u_n)\delta(v-v_m), \tag{2.3}$$

where the product between N and M specifies the maximum number of spatial frequency domain information that the particular interferometric imaging array can measured and $\delta(\cdot)$ is the delta function. The discretely sampled/filtered scene visibility can be expressed as $V_s(u,v) = V(u,v)\cdot S(u,v)$, which is the product between the scene visibility and the discrete spatial frequency

sampling function similar to the continuous case as demonstrated in (2.2). The reconstruction of the intended scene intensity can thus be recovered by

$$I_r(\alpha, \beta) = \sum_{n=1}^{N} \sum_{m=1}^{M} V(u_n, v_m) e^{-j2\pi(u_n\alpha + v_m\beta)}. \tag{2.4}$$

The associated spatial resolution of the interferometric imaging technique can be characterized by the null-to-null beamdwidth of the response due to the largest antenna baseline separation available in the imaging array in each dimension. For a one-dimensional linear array where the largest antenna baseline separation is $D_{1D,max}$, the associated null-to-null beamdwidth can be represented by

$$\theta_{NNBW} \approx 2\frac{2}{D_{1D,max}}. \tag{2.5}$$

Considering the two-dimensional case where x and y are used to describe the horizontal and vertical dimensions, the spatial resolution for each of the two axes of an interferometric imaging array can thus be represented by

$$\Delta\theta_{x,y} \approx \theta_{NNBW}^{(x,y)}. \tag{2.6}$$

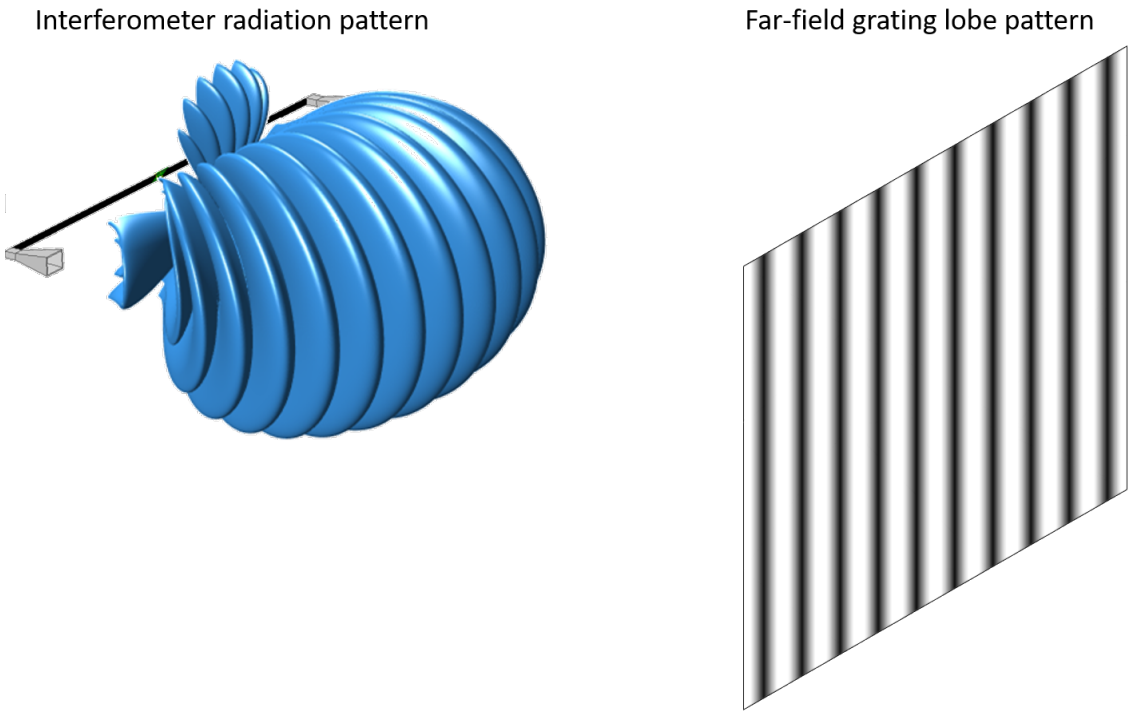

Figure 2.2: Interferometric radiation pattern and the projected pattern in the far field. The sinusoidal pattern maps to a specific spatial frequency. [1].

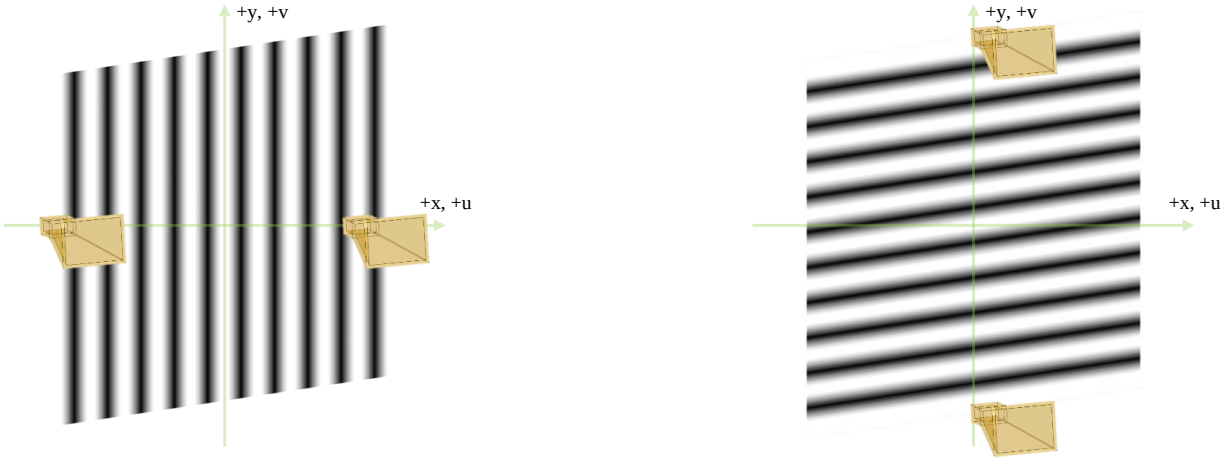

(a) (b)

Figure 2.3: The interferometric radiation pattern also depends on the orientation of an antenna pair. (a) Horizontal orientation. (b) Vertical orientation.

2.1.2 Common (Static) Antenna Array Designs

With the knowledge of how the baseline separation and orientation of all antennas are uniquely configured to maximize the two parameters N and M from (2.3) and (2.4), it is helpful to discuss some common interferometric antenna array configurations. To better distinguish these conventional array designs from the dynamic antenna array concept that will be discussed later, these common interferometric antenna arrays are considered static which means the antenna arrays do not accommodate any dynamic mobility nor do the antennas moved relatively within the static array.

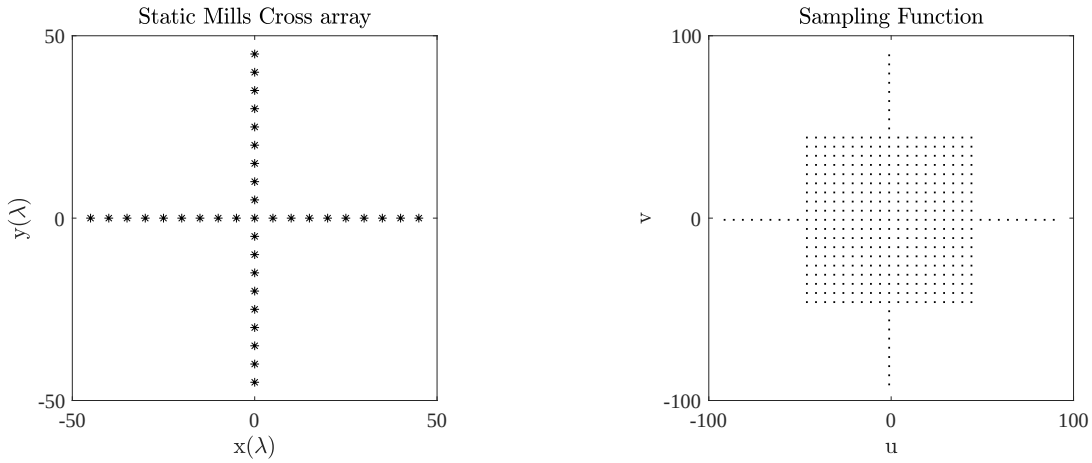

(a) (b)

Figure 2.4: (a) Array configuration of a 37-element Mills Cross array with an equal inter-element spacing of 5λ and a maximum dimension of 95λ. (b) The corresponding sampling function that has 397 unique spatial frequency sampling points.

Three examples of common static interferometric antenna arrays are shown in Figs. 2.4, 2.5, and 2.6 along with their corresponding spatial frequency domain sampling function to the side. These configurations are the Mills Cross array (Fig. 2.4), the T-array (Fig. 2.5), and the Y-array (Fig. 2.6). Each of the three configurations assumes an equal inter-element spacing of 5λ and a maximum dimension of 95λ. For the presented Mills Cross array in Fig. 2.4(a), there is a total of 37 receiving antennas for the array configuration where a total of 397 unique spatial frequency sampling point can be generated (Fig. 2.4(b)). By removing the top nine receiving antennas from the Mills Cross Array, is another common array configuration showing a 28-element T-array

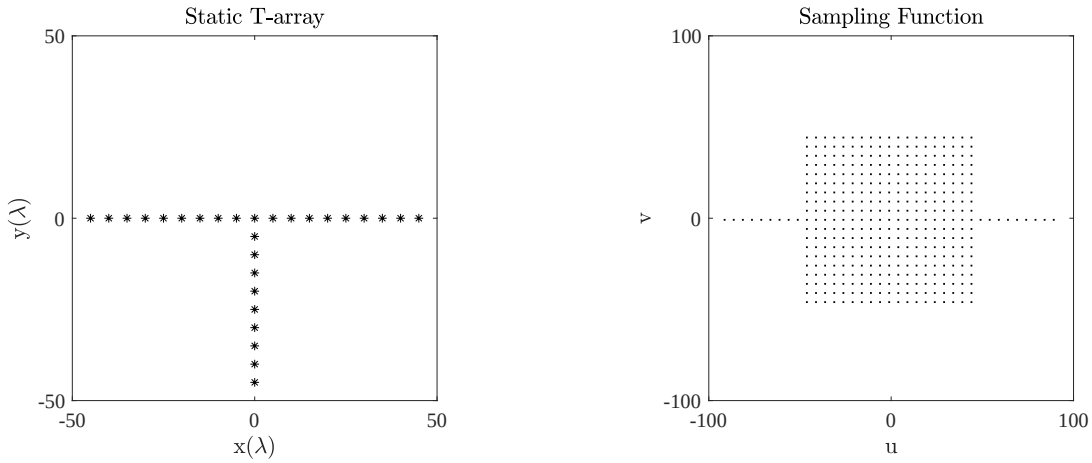

(a) (b)

Figure 2.5: (a) Array configuration of a 28-element T-array with an equal inter-element spacing of 5λ and a maximum dimension of 95λ. (b) The corresponding sampling function that has 379 unique spatial frequency sampling points.

in Fig. 2.5(a) where the number of unique spatial frequency sampling points is 379. Comparing the examples between the T-array and the Mills Cross array, a hardware reduction of nine antennas only accounted for 18 less unique spatial frequency sampling points which can be considered as a reasonable design trade off. Shown in Fig. 2.6(a) is another array configuration commonly known as the Y-array that also has a 28-element array configuration. By bending the top portion of the T-array to form Arm1 and Arm2 of the Y-array, more unique baselines and orientations are now available from the Y-array. This is shown by its associated sampling function in Fig. 2.6(b) with 541 unique spatial frequency sampling points, a significant improvement of additional 162 unique sampling points comparing to the aforementioned T-array configuration.

While the quantitative comparison of unique spatial frequency sampling points demonstrates the effectiveness of different design configurations of static interferometric antenna arrays, qualitative visual examples are also presented in Fig. 2.7 where the Michigan State University Spartan helmet is used as a simulated scene of interest for interferometric image reconstruction. Comparing Fig. 2.7(b) and (c), which corresponds to the 37-element Mills Cross array and the 28-element T-array, respectively, there are no significant differences between the two reconstructions. This is expected as the previously discussed reduction of 18 unique spatial frequency sampling

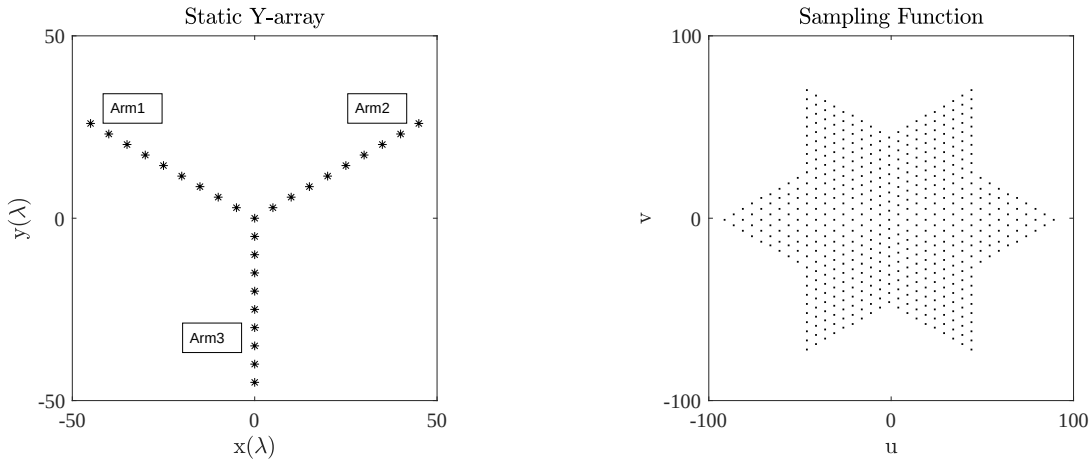

(a) (b)

Figure 2.6: (a) Array configuration of a 28-element Y-array with an equal inter-element spacing of 5λ and a maximum dimension of 95λ. (b) The corresponding sampling function that has 541 unique spatial frequency sampling points. [2].

points for the 28-element T-array do not contribute much to the overall reconstruction quality. The simulated reconstruction using the 28-element Y-array, however, does appear to be sharper compared to the Mills Cross and the T-array reconstructions with better resemblance of the crests of the Spartan helmet.

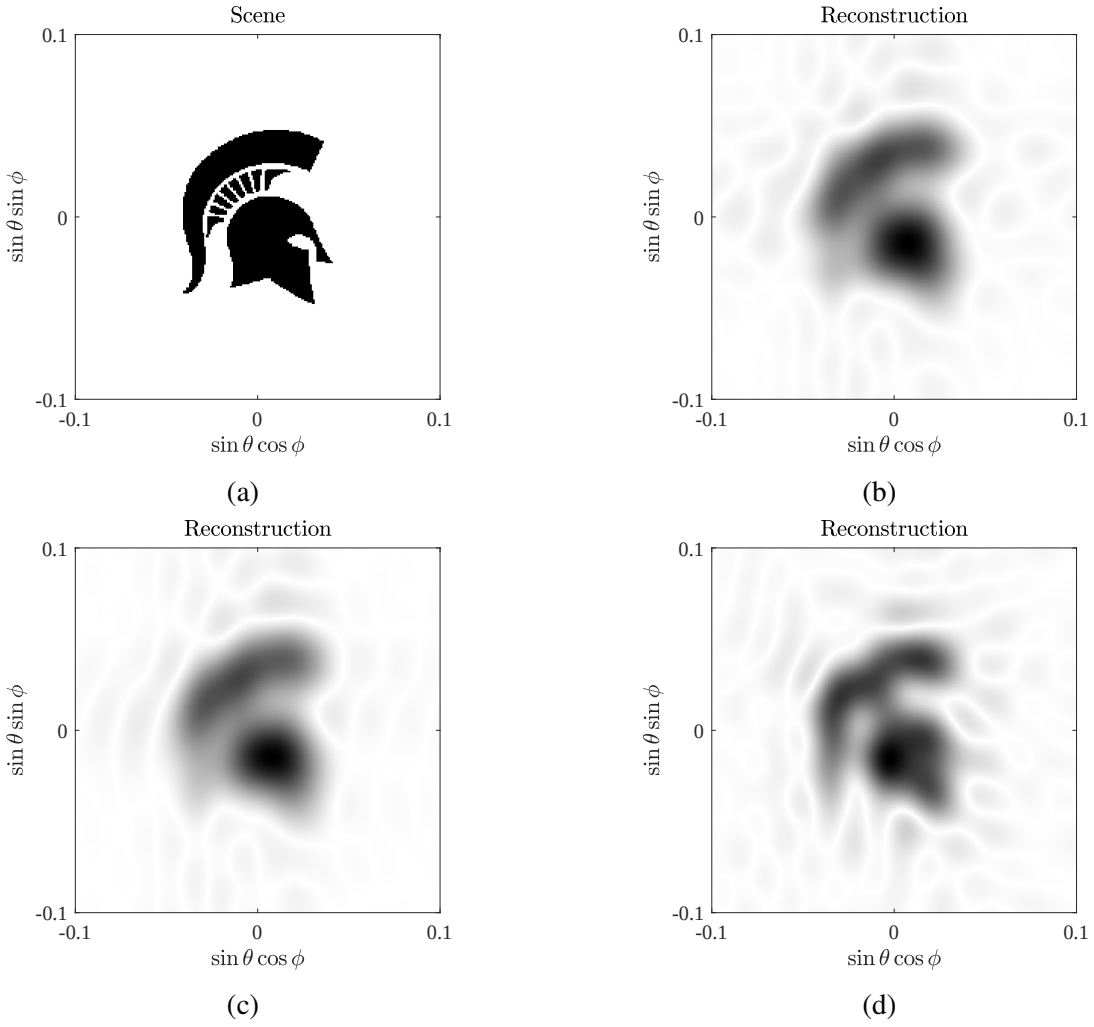

Figure 2.7: (a) The Michigan State University Spartan helmet as a simulated scene of interest for interferometric image reconstruction [2]. (b) Simulated reconstruction using the 37-element Mills Cross array. (c) Simulated reconstruction using the 28-element T-array. (d) Simulated result using the 28-element Y-array [2].

2.2 Dynamic Antenna Array Design

As demonstrated in the previous section, the design considerations of conventional static interferometric imaging arrays surround the number of antennas as well as the unique placement of individual antennas with the objective to achieve as many unique sampling points as possible in the spatial frequency domain. While it is logical to perform design optimization between iterations, it is generally impossible for a static interferometric imaging arrays to acquire additional unique spatial frequency sampling points. In radio astronomy interferometric arrays, the rotation of the Earth is frequently leveraged to modify the apparent baselines relative to a given celestial direction, where a denser sampling function, filling over time with additional unique sampling points, is achieved than the array obtains statically [45]. However, Earth rotation dynamics are nonetheless inapplicable outside of astronomical observation and are also not manipulable dynamics for design consideration; ergo, this motivates the idea of designing controllable array dynamics. This motivation is also supported by the recent works that demonstrated the capabilities of relatively fast platform dynamics for distributed arrays with improving performance by reducing radiation pattern sidelobes [61, 62].

In the remaining of this section, a dynamic antenna array design that incorporates rotational dynamics will be introduced and discussed. Lastly, the experimental implementation of the rotational dynamic antenna array is discussed in detail as it is used for both measurements presented in both Chapter 3 and 4.

2.2.1 Design for Spatial Frequency Sampling Using Rotational Array Dynamics

In contrast to designing static interferometric antenna arrays where the quantities N and M from (2.3) can only be determined by the number of antennas and their placements, a dynamic antenna array concept is proposed where rotational dynamics is designed for a sparse linear antenna array such that far less antennas are needed to generate comparable number (i.e., $N \cdot M$) of unique spatial frequency sampling points. The rotational dynamic antenna array concept is shown in Fig. 2.8

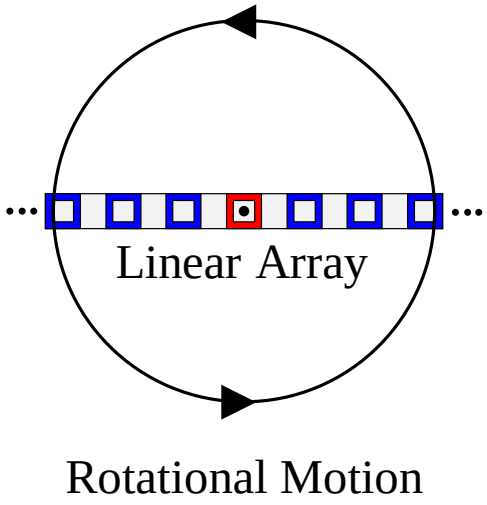

Figure 2.8: Illustration of the proposed dynamic-antenna-array-based sparse linear array with rotational dynamics with regard to the centroid of the array. The center antenna of the array is shown in red, and antennas on either side from the center are shown in blue. Via a simple rotation of the array, a significant increase in the density of the spatial frequency sampling function can be obtained with a minimal set of hardware. [2].

where the antennas are represented by the hollowed squares (red and blue) and the centroid of the sparse linear array is at the location of the antenna represented by the red hollow square. The rotational dynamics is desired because it enables multiple spatial frequency information to be sampled using the same antennas as multiple orientations of antenna pairs can be achieved (as previously illustrated in Fig. 2.3). Furthermore, the rotation concept has also been used in imaging techniques using linear arrays and Radon transform based tomographic reconstruction [63]. While a uniform linear antenna array is presented for discussion, the number of antenna elements may be further reduced with the use of a minimum-redundancy array design [64].

Incorporating both the sparse linear array design and the rotational dynamics, the modified sampling function (2.3) for a rotational dynamic array with L elements can be given in terms of the antenna baselines D_l and the set of K rotation angles $\gamma(k)$ by

$$u_{lk} = D_l \sin\left(\gamma(k)\right), \tag{2.7}$$

and

$$v_{lk} = D_l \cos\left(\gamma(k)\right), \tag{2.8}$$

where the discrete rotated angles are given in terms of the initial angle of the array γ_0, the rotational rate γ_r, and the integration time for each sample τ by

$$\gamma(k) = \gamma_0 + \gamma_r k\tau. \tag{2.9}$$

The dynamic spatial frequency sampling function is thus given by

$$S_D(u,v) = \sum_{l=0}^{L-1} \sum_{k=0}^{K-1} \delta\left(u - u_{lk}\right) \delta\left(v - v_{lk}\right). \tag{2.10}$$

Note that the sign of $\gamma(k)$ indicates whether the array rotates in the clockwise or counterclockwise direction and is a matter of design choice.

As a comparison to the previously discussed static interferometric antenna arrays, an example comprising a dynamically synthesized array from a nine-element sparse linear array with counterclockwise rotational dynamics where the sampling happens every 3° are shown in Figs. 2.9(a)-(d) at four sequential instances from start of sampling, a half-way through, three-quarters through, and at the completion of the sampling. The sparse linear array is of a uniform linear array with $L = 9$, $K = 60$, and an inter-element spacing of 12λ yielding a maximum dimension of 96λ which is comparable to the three conventional static antenna array of 95λ covered in the previous section. Furthermore, the rotational dynamics yield a synthesized array configuration that can be described as a nested concentric circular array. Similar to the synthesized arrays at four instances, Figs. 2.10(a)-(d) show the progression of the synthesized sampling function at the same instance. As the sparse linear array is uniformly spaced, the resulting sampling function also takes

the form of nested concentric circles. Note that with the assumed sampling interval of every 3° and a rotation over 180° angular span, the final synthesized sampling function comprises 1045 unique spatial frequency sampling points. Furthermore, because the two-dimensional spatial frequency domain is conjugate symmetric for image intensities, which comprise real amplitudes, a 180° rotation of the dynamic antenna array can cover a full circularly sampled visibility where continuation of rotation can yield subsequent synthesized sampling function. In addition, this concept requires no reset of the array position between measurements, i.e., continuing rotation on the other half of the circular path will generate the same sampling function thus each successful revolution of the dynamic array corresponds to two revolutions of the dynamically synthesized sampling function. It can also be seen that a counterclockwise rotational movement on the xy-plane corresponds to counterclockwise rotational course on the uv-plane. In Figs. 2.11(a)-(d), reconstructions of the same Spartan helmet from Fig. 2.7(a) for the four instances are shown to demonstrate the improvement of image formation throughout the dynamic progression of the spare linear antenna array. For the initial reconstruction, the reconstruction is simply in one dimension as the array is simple and linear. Half-way through the measurement, the two-dimensional image begins to take form, with further refinement throughout the dynamic array's progression. The final reconstruction is comparable to the result of the Y-array from Fig. 2.7(d), however the dynamic antenna array in the presented case is formed with less than 1/3 the number of antenna elements as the benchmarked 28-element Y-array.

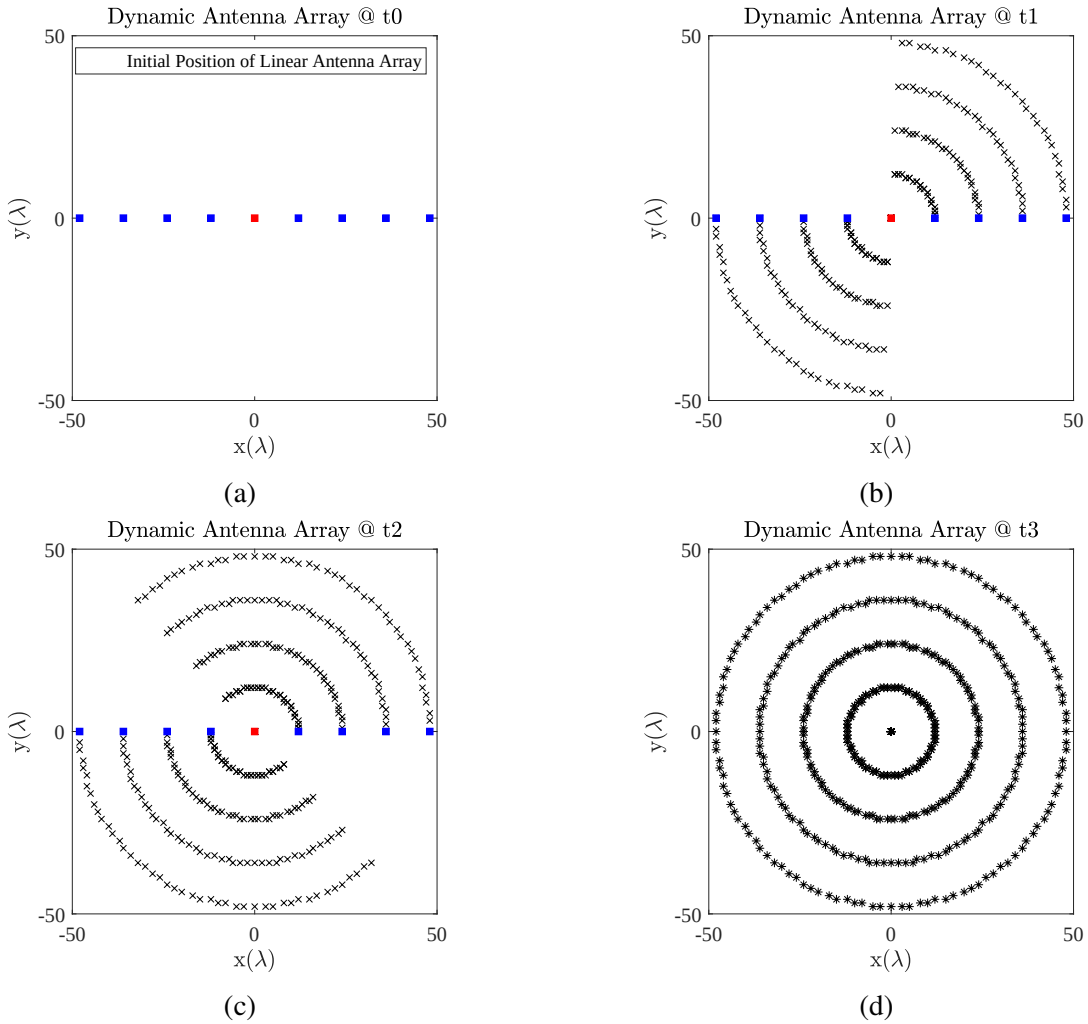

Figure 2.9: Illustration of a dynamic-antenna-array-based nine-element sparse linear array with counterclockwise rotational motion at four instances. Progression of the elapsed dynamic antenna array formation are shown. From (a) initial position of the nine-element sparse linear array with the center antenna shown in red, and the remaining in blue; to (b) elapsed dynamic antenna array formation after one quarter rotation; to (c) elapsed dynamic antenna array formation after three quarters rotation; and to (d) the total elapsed dynamic antenna array formation after a full 180° rotation. [2].

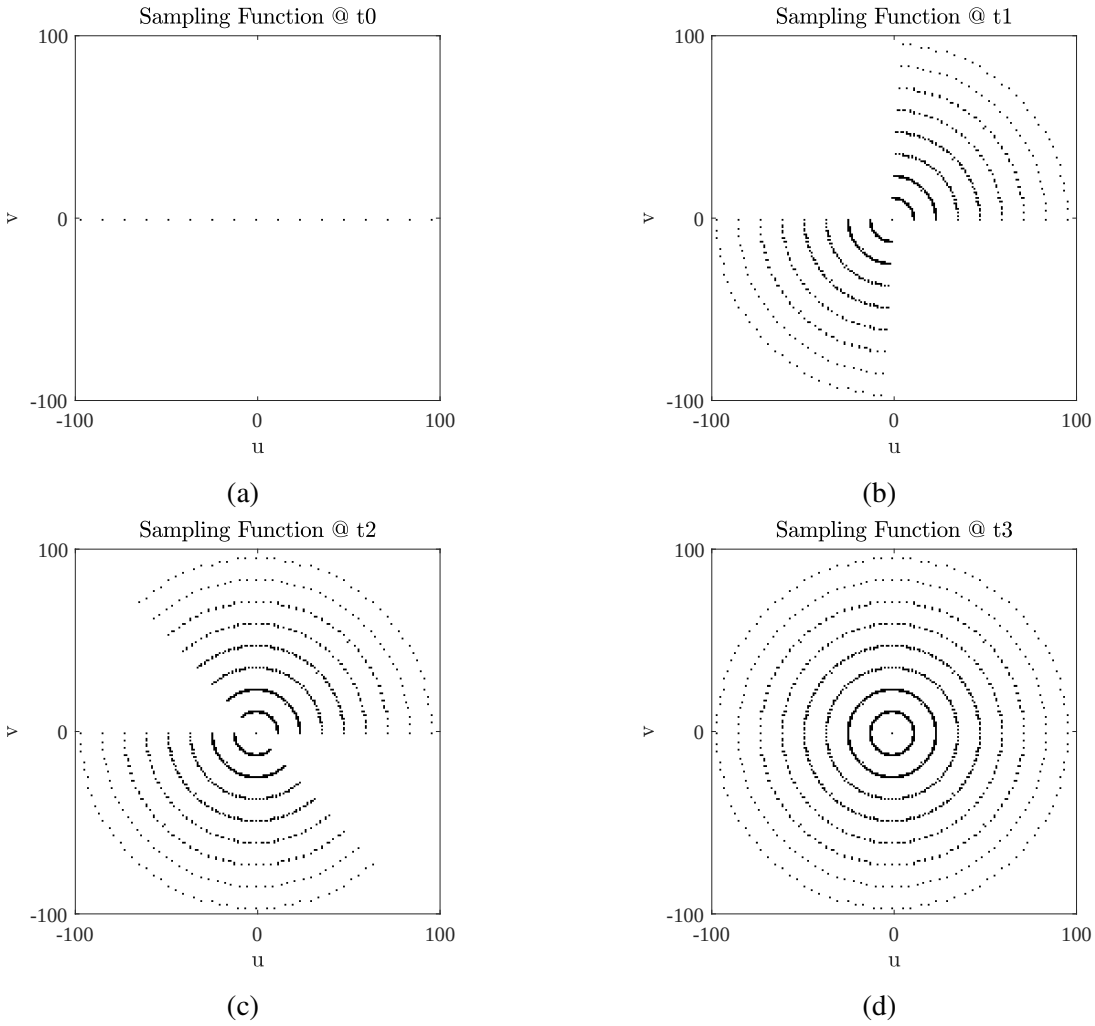

Figure 2.10: Illustration of the synthesized spatial frequency domain sampling function at four instances corresponding to Fig. 2.9 using a dynamic-antenna-array-based nine-element sparse linear array with counterclockwise rotational motion. Progression of the elapsed synthesized spatial frequency sampling function are shown. Synthesized sampling function of the nine-element sparse linear array (a) without dynamics, (b) after one quarter rotation, (c) after three quarters rotation; and to (d) after a full 180° rotation. Note that the synthesized sampling function comprises of 1045 unique spatial frequency sampling points. [2].

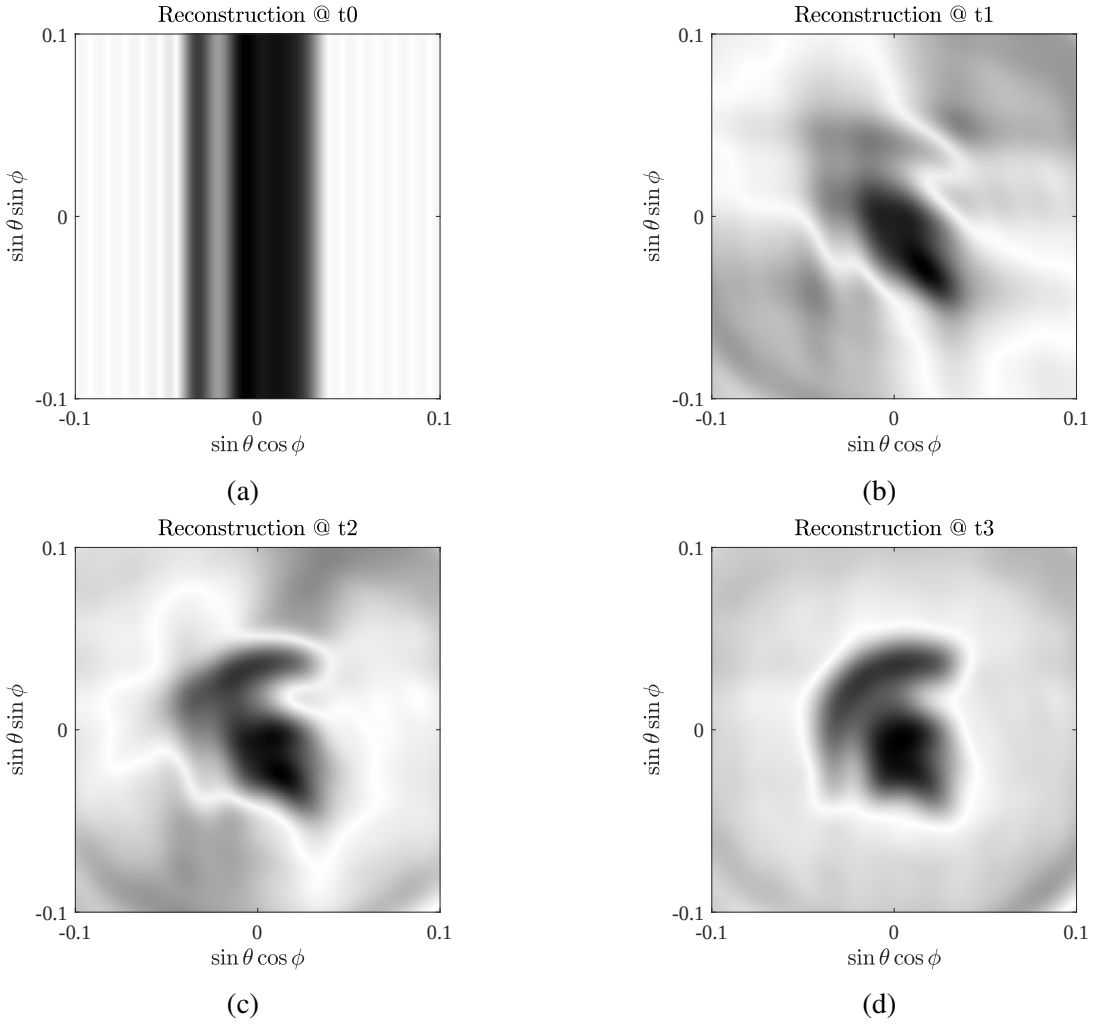

Figure 2.11: Illustration of the scene reconstruction using the corresponding synthesized spatial frequency domain sampling function at four instances from Fig. 2.10 using a dynamic-antenna-array-based nine-element sparse linear array with counterclockwise rotational motion. Progression of the improving scene reconstruction are shown. Scene reconstruction using the nine-element sparse linear array (a) without dynamics, (b) after one quarter rotation, (c) after three quarters rotation; and to (d) after a full 180° rotation. [2].

For the described spatial frequency sampling approach using a rotational dynamic antenna array, the minimum observation time T for a complete measurement, by synthesizing the desired sampling function, relies on both the number of samples k and the integration time τ that is required at each sampling point which can be expressed by $T = k\tau$. For reference, it is worth noting that the integration time of passive interferometric imagers can be on the order of seconds. In contrast, recent improvements from the aforementioned AIM imaging technique enables the imaging process with significantly less integration time to obtain equivalent sensitivities which has been demonstrated to form images at a rate of 652 frames per second [65]. Therefore, with noise illumination, the integration time τ can be designed relatively small as to the dynamics of the environment in many situations such as the use case of detection of concealed contraband. The integration time in [65] was only 64 μs, where the total measurement time per frame was 1.469 ms when considering system latencies. It is reasonable then to characterize the maximum potential rotational rate of the proposed dynamic antenna array, which a spatial frequency domain grid size in increments of 1 $\mathrm{cycles} \cdot \mathrm{rad}^{-1}$ is assumed in the uv-plane and an integration time of $\tau = 10$ ms is assumed that is well above the demonstrated capability of the referenced AIM experimental work. The rotational dynamics of the imaging array must therefore ensure that the dwell time at a spatial frequency pixel, ($u = u_{sampled}, v =_{sampled}$), is not less than the integration time. Otherwise, the received signal information will be spread across multiple spatial frequency pixels. Furthermore, the maximum dwell time is dependent on the rotational rate of the antenna that is affected by the maximum antenna baseline, D_{max}, and the number of unique spatial frequency grids/samples given by $2\pi D_{\lambda}$. The equivalent rotational rate in revolutions per minute (RPM) for an assumed dwell time of 10 ms is presented in Fig. 2.12 as a function of D_{max} up to 200λ. The ranges of baselines for the experimental setup, to be discussed later, are also shown. The rotational rate for the simulated baseline ranges is near 1000 RPM and above, indicating that the temporal dynamics of the dynamic antenna array will not be a limiting factor for image formation. In addition, these RPMs support implementation for applications such as contraband detection, remote sensing, and/or monitoring of manufacturing processes where the environmental dynamics

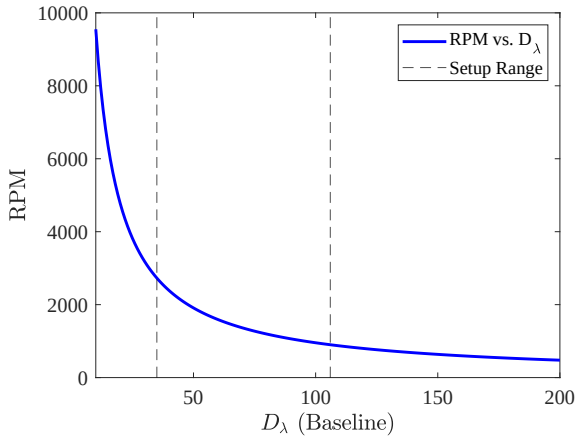

Figure 2.12: Maximum rotational speed versus baseline formed by the two receiving antennas based on a spatial frequency grid (uv-plane) increment of 1 $\mathrm{cycles} \cdot \mathrm{rad}^{-1}$ and a minimum dwell time per grid of 10 ms. The two dashed-black lines indicate the range of baselines achieved by the implemented experimental setup. [2].

are sufficiently slower such that the scene can be considered static during the dynamic rotation of the antenna array.

2.3 Rotational Dynamic Antenna Array Implementation

In this section, the experimental implementation of the aforementioned rotational dynamic antenna array concept is discussed. The rotational dynamic antenna array system is divided into two major subsystems based on functionality including transmitting and receiving. Furthermore, components such as cables, adapters and power supplies are included in a detailed list of parts along with the schematics in Appendix A.

On the transmitting end of the rotational dynamic antenna array sensing system, there are three identical circuits in the subsystem. For each circuit, a noise source (RF-GADGETS, XDM NSE15-1) was selected to generate baseband noise signal between 10–1600 MHz to fulfill the active interferometric technique as discussed previously. The generated noise signal was then boosted through four cascaded amplifiers (Mini-Circuits, ZX60-V63+) with an operational wideband of 0.05–6 GHz. The amplified noise signal was subsequently fed to the intermediate frequency (IF) port (IF1) of an upconverter (Analog Devices, HMC6787ALC5A) with its IF2 matched to a 50 Ω terminator (Amphenol RF, 132360). The particular upconverter model was selected for its desirable frequency doubling feature at the local oscillator (LO) port which was internally integrated to double the input signal that was designed at 19 GHz yielding an upconverted noise signal at 38 GHz which corresponds to a wavelength of $\approx$ 7.89 mm. The upconverted noise signal was then sent through a power amplifier (Analog Devices, HMC7229LS6) before fed to a waveguide (Sage Millimeter, SWC-28KM-E1) that connects to a 10 dBi standard gain horn antenna (L3Harris Narda-ATM, 28-440-6) for illumination of the scene.

On the receiving end of the rotational dynamic antenna array sensing system, there are two identical circuits in the subsystem. For each circuit, the backscattered noise illumination was captured through a 15 dBi standard gain horn antenna (L3Harris Narda-ATM, 28-441-6) that was mounted to a waveguide (Sage Millimeter, SWC-28KM-E1) which allows the received signal to be sent through a low noise amplifier (Analog Devices, HMC1040LP3CE). The amplified receive signal was then fed to a downconverter (Analog Devices, HMC6789BLC5A) with the same designated 19 GHz LO signal yielding two downconverted in-phase and quadrature signals.

A close-up photograph for the transmitting end and the receiving end are included in Fig. 2.13. Full photographs of the most recent improved rotational dynamic antenna array implementation are shown in Fig. 2.14, the adjustable baseline range between the two receiving antennas is [44.4 cm, 83.6 cm], or [35λ, 106λ] based on 38 GHz. Earlier iterations of the dynamic antenna array concept are also included in Appendix A where Fig. A.4 (first iteration) and Fig. A.5 (second iteration) were implemented with different mounting locations for the transmitting and receiving antennas yielding a different set of baselines that can be achieved. In the first iteration, all transmitting and receiving antennas were mounted on the same frame rail where the two receiving antennas had an adjustable baseline range of [60.0 cm, 83.6 cm], or [76λ, 106λ] based on 38 GHz. In the second iteration, two additional frame rails were added to allow the relocation of the transmitting antennas which enable a wider adjustable baseline range between the two receiving antennas which was [63.4 cm, 83.6 cm], or [50λ, 106λ] based on 38 GHz. The transmitting and the receiving antennas co-rotate with regard to the same center of rotation to guarantee co-polarization among all nodes of the sensing system which allows optimum efficiency between the transmitted noise illumination and the received signals [66]. In the case that design constraints do not allow the transmitters and receivers to co-rotate as in a manner as described above, one can possibly elect circularly polarized antennas as a design resolution without compromising the system's performance [67, 68].

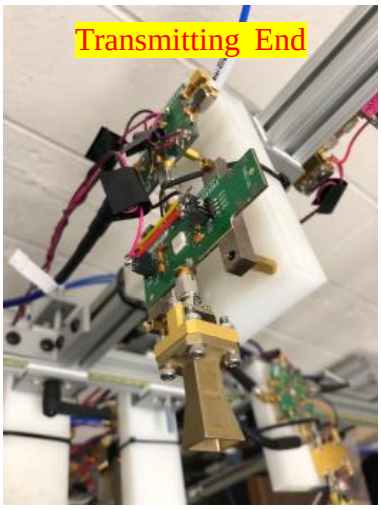

(a)

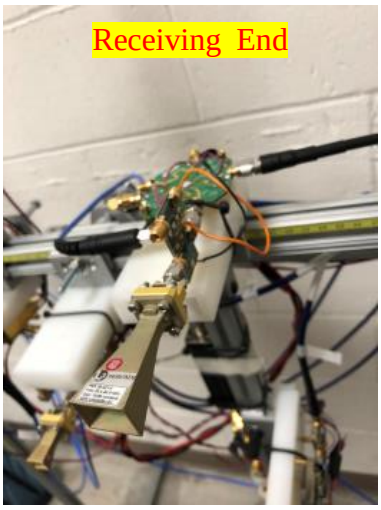

(b)

Figure 2.13: Close up photographs of the (a) transmitting end (b) receiving end of the implemented dynamic antenna array. [2].

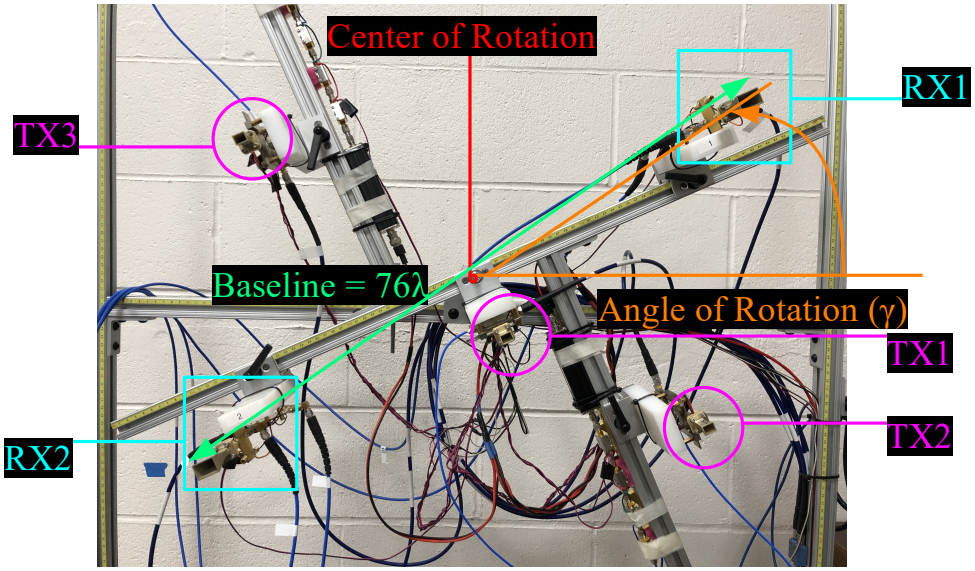

Figure 2.14: Third iteration of the implemented dynamic antenna array. Two receivers have an adjustable baseline range of [44.4 cm, 83.6 cm], or [35λ, 106λ] based on 38 GHz with the photograph showing a baseline separation of 76λ. [5].

CHAPTER 3

ACTIVE INTERFEROMETRIC IMAGING WITH ROTATIONAL DYNAMIC ANTENNA ARRAY

In this chapter, AIM imaging is realized through a rotational dynamic sparse linear array concept where the sparse linear array is synthesized using the two-element dynamic antenna array from Section 2.3 in conjunction with the rotational dynamics for two measurements: single spherical target and two spherical targets. As the dynamic antenna array rotates, cross-correlations of the received scattered signals for each antenna pair in the sparse linear array provide samples of the spatial frequency information of the scene to facilitate reconstruction via inverse Fourier transform. The rotational dynamics of the linear array enable generation of curves of sampling points in the spatial frequency domain which depend on antenna baseline vector and the rotation to yield a more accurate scene reconstruction. As pointed out in Section 2.2 that traditional static interferometric imaging arrays use nearly an order of magnitude fewer antenna elements than comparable phased arrays, the rotational dynamic sparse linear array concept requires only a simple linear array, further reducing the number of hardware elements required. The 38 GHz dynamic antenna array imaging system from Section 2.2 and the corresponding experiment setup will be first described followed by subsequent discussion between simulations and measurements.

3.1 Experimental Setup

Measurements using the active interferometric based rotational dynamic antenna array were conducted in a 7.6 m semi-enclosed arch range with backwalls constructed from radio frequency (RF) absorbers behind the measuring scene. An example of the measured scenes is included in Fig. 3.1 showing the side view of the two metallic spheres experiment. Two measurements were conducted where one contains a single spherical target and the other contains two. A reflecting spherical target is ideal for calibration or validation measurements as it appears as a single reflecting point where the radar cross-section (RCS) σ is only dependent on the physical dimension of the sphere (i.e., independent of angle and frequency) as described by $\sigma = \pi a^2$, where a is the radius of the sphere.

Figure 3.1: Side view of the experiment setup of two reflecting spherical targets backed by walls of RF absorbers in a 7.6 m semi-enclosed arch range. [2].

To ensure alignment for tracking the rotated angle of the dynamic synthesized linear array, a standard digital angle gauge with 0.1° accuracy was attached to the rotating frame of the setup shown in Fig. 2.14. To synthesize a sparse linear array for the proof-of-concept measurements using the described setup (Fig. 2.14), the two receiving antennas were fixed to a given baseline and the rotatable segment of the setup was moved to achieve the rotational dynamics. After a single 180° rotation which corresponds to a full circular curve of sampled information in the spatial frequency domain, the receiving antennas were relocated to form a different baseline and a second full circular curve of sampled information is obtained by using the same dynamic rotation. This process allows the synthesis of an equivalent linear receiving array using the available hardware resources as described in Section 2.3; a dedicated setup using multiple receivers and a multichannel digitizer could also be directly implemented with identical results to the described herein. For each of the two measurements, eight baselines, from 50λ to 106λ in 8λ increments, were implemented between the two receiving antennas to synthesize a representative sparse linear array by adjusting the separation between the two receivers of the setup as illustrated in Fig. 2.14. Furthermore, 45 angles, formed between the straight baseline separation of the two receiving antennas and the horizontal plane, were implemented in 4° increments between 0° to 176°. The combination using the selected baselines from the synthesized linear array and the designed angles generated a spatial frequency sampling function comprising 360 unique measured samples locating in the upper half of the uv-plane for image reconstruction as shown in Fig. 3.2.

Connected to the dynamic antenna array setup for the 19 GHz external local oscillator source was the Keysight N5183A signal generator. For offline processing using MATLAB, a Keysight MSO-X 92004A oscilloscope was connected to the downconverted in-phase and quadrature baseband signals for digitization and recording using a sampling rate of 2.5 GS/s with an integration time of 100 μs.

The associated MATLAB Codes for processing the recorded data are included in APPENDIX B.1 and B.2 with the results and analyses to be described in the subsequent section.

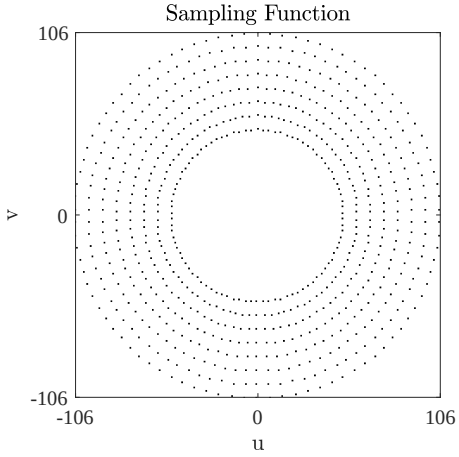

Figure 3.2: Synthesized spatial frequency sampling function from the dynamic antenna array setup using 45 angles, formed between the direct distance of the two receiving antennas and the horizontal plane, from 0° to 176° in 4° increment and eight baselines from 50λ to 106λ in 4λ increment. [2].

3.2 Simulations and Measurements

The first measurement comprises a single reflecting spherical target that is shown in Fig. 3.3(a) where the physical diameter of the sphere is 24 cm yielding an RCS value of -13.44 dBsm which is independent of the operating frequency of 38 GHz. The target was placed approximately 1.83 m from the dynamic antenna array and was positioned at a height of 1.156 m with a horizontal alignment to the dynamic antenna array's center of rotation. Note that the center of rotation of the dynamic antenna array has a height of 1.178 m. Using the described positions of the target relative to the dynamic antenna array, a simulated reconstruction using the synthesized spatial frequency sampling function (Fig. 3.2) can be seen in Fig. 3.3(b). As the spherical target was placed to horizontally align with the center of the dynamic antenna array, the expected horizontal location is near $\sin\theta\cos\phi = 0$; in the vertical direction, because the target was below the center of the dynamic antenna array, the expected vertical location is at $\sin\theta\sin\phi = -0.012$ which is slightly below $\sin\theta\sin\phi = 0$. Sidelobe structures that are due to the radially discrete nature of the spatial frequency sampling function can be observed from the simulated reconstruction. Furthermore, speckles within the simulated reconstruction are also the result of the discrete sampling process that is dependent on the rotational dynamics. The measurement of the single reflective sphere is shown in Fig. 3.3(c) where a pad factor of 1 was used prior to computing the inverse Fourier transformation for image reconstruction. The position of the spherical target in the measured reconstructed image and the sidelobe structures both show close resemblance to the simulation. To refine the measured reconstruction, the CLEAN algorithm [3], introduced in 1974 to perform iterative deconvolution on radio astronomy generated images that are assumed to comprise point sources, was implemented to remove the sidelobe artifacts as due to the synthesized sampling function as shown in Fig. 3.2. This is accomplished by subtracting the product between the loop gain l_G and the convolution between the known point source location I_{pt} and the synthesized beam, or the point spread function (PSF) of the system from the reconstructed image I_r by

$$I_{r,CLEAN} = I_r - l_G \cdot \left(I_{pt} * PSF\right). \tag{3.1}$$

The loop gain value affects how much of deconvolution is applied during each iteration. The iterative characteristic of the CLEAN algorithm not only accommodates images comprising multiple point sources, but also accounts for measurement imperfection where a single point source might be reconstructed as a cloud of closely clustered points. The refined result using 15 iterations with a loop gain value of 1 is shown in Fig. 3.3(d) where the artifacts outside the anticipated target responses are mitigated. It is evident that the location of the reconstructed point source (Fig. 3.3(c) and (d)) is close to that of the actual location as predicted by the simulation (Fig. 3.3(b)).

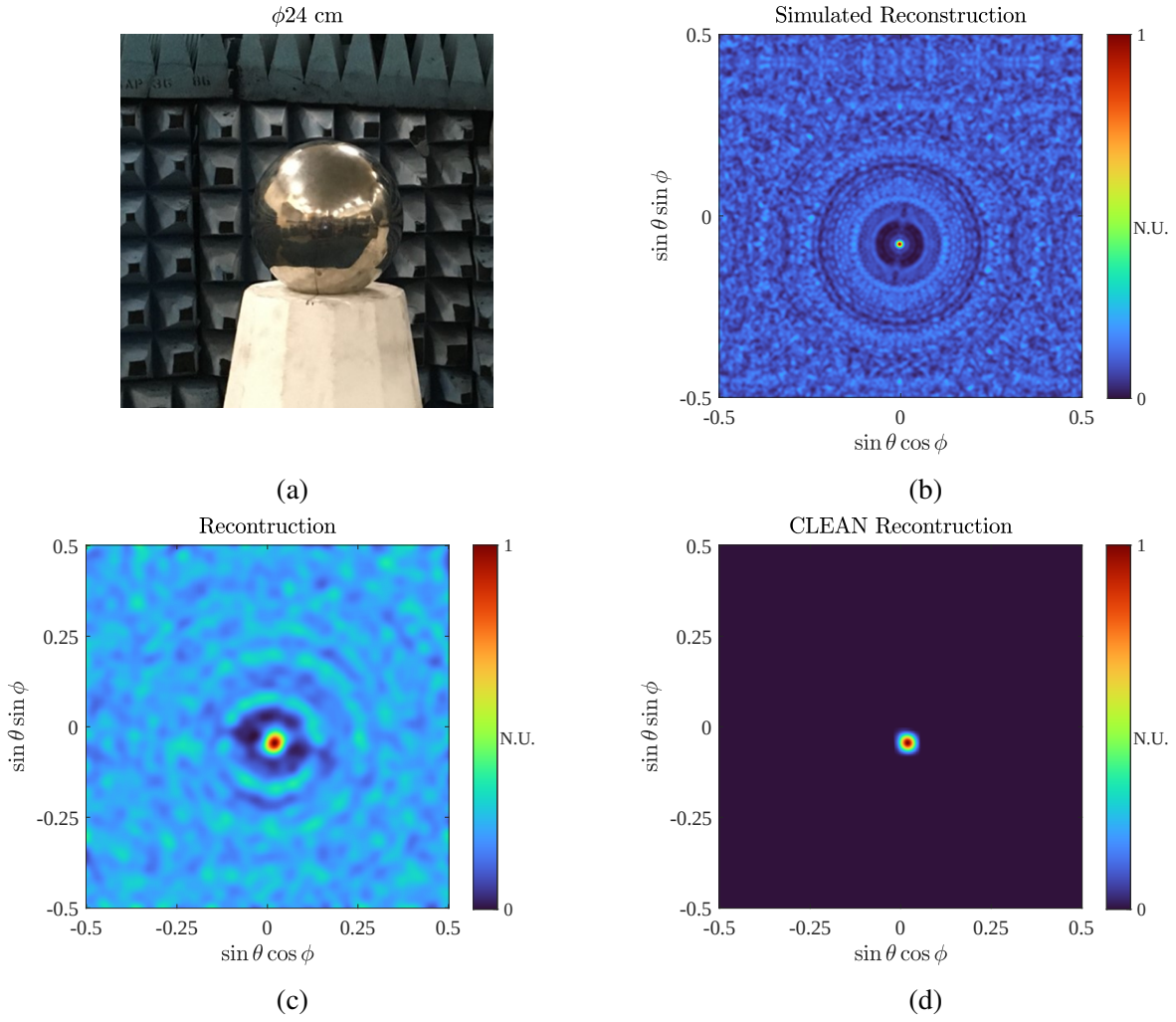

Figure 3.3: (a) Scene comprising a single point source which is a metallic sphere with a 24 cm diameter and an RCS value of -13.44 dBsm. (b) Simulated reconstruction based on RCS and position. (c) Simple interferometric reconstruction of the measurement on (a). (d) CLEAN deconvolution algorithm [3] applied to (c) using 15 iterations with a loop gain of 1. [2].

The second measured scene comprising two spherical targets as point sources each with a physical diameter of 20 cm and an associated RCS value of -15.02 dBsm is shown in Fig. 3.4(a). Similar to the single sphere measurement, the distance between the dynamic antenna array and the two spheres was 1.83 m. The sphere on the left was placed at a height of 1.168 m and the one on the right was placed at a height of 1.080 m. A horizontal separation of 0.445 m between the two spheres was implemented where the horizontal midpoint was positioned to align with the center of the dynamic antenna array. Using the positions of the two spheres relative to the dynamic antenna array, a simulated reconstruction using the synthesized spatial frequency sampling function shown in Fig. 3.2 can be seen in Fig. 3.4(b). The left sphere was placed to the left relative to the dynamic antenna array's center; hence, it has an expected horizontal position about $\sin\theta\cos\phi = -0.121$; vertically, it was slightly placed below the height of the dynamic antenna array's center giving an expected vertical position about $\sin\theta\sin\phi = -0.006$. For the spherical target on the right, it was placed to the right of relative to the dynamic antenna array's center, hence, it has an expected horizontal position about $\sin\theta\cos\phi = 0.121$; vertically, it was placed much lower than the left spheres giving an expected vertical position about $\sin\theta\sin\phi = -0.054$. The measured and the further CLEAN refined reconstructions are shown in Fig. 3.4(c) and (d), respectively. Note that the measured reconstructions are slightly higher than the anticipated locations according to the simulation (Fig. 3.4(b)). This is possibly due to specularity as the plane of the dynamic antenna array's receiver might not be completely parallel to the plane of the measurement targets due to implementation and setup, therefore introduced the small vertical shift. Without applying the deconvolution algorithm for refinement, an unexpected third response was observed between the anticipated two responses related to the spheres. In addition, the deconvolution refinement (15 iterations, loop gain of 1) only reduced and not completely removed the unexpected third response. In spite of the small vertical shift and the unexpected third response, it is still evident that the locations of the two strongest reconstructed point sources (Fig. 3.4(d)) show close resemblance to the actual locations as suggested by the simulation (Fig. 3.4(b)).

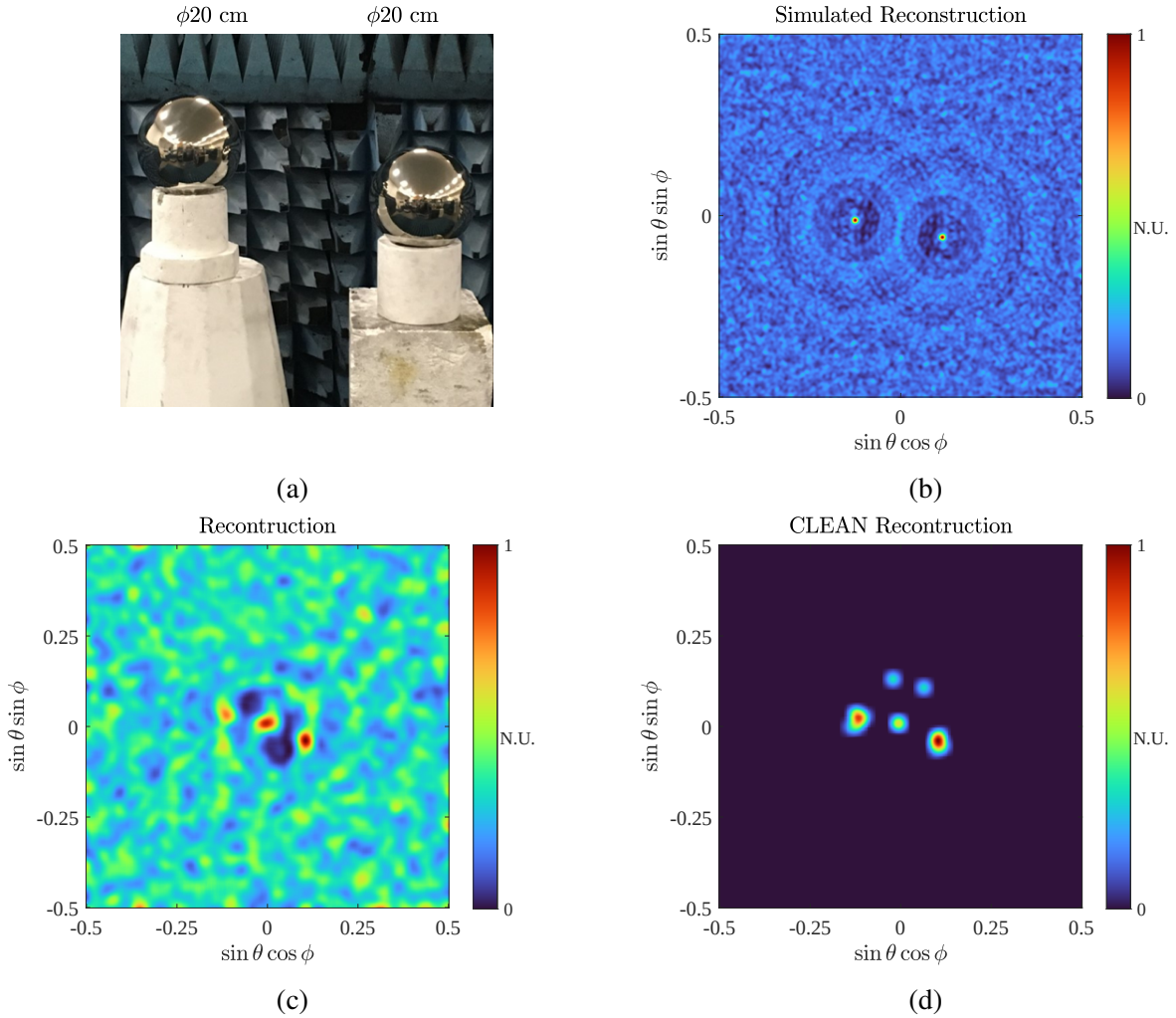

Figure 3.4: (a) Scene comprising two point sources of equal RCS without RF absorbers in between. Both point sources are metallic sphere with a 20 cm diameter yielding an RCS value of -15.02 dBsm. (b) Simulated reconstruction based on RCS and position of (a). (c) Simple interferometric reconstruction of the measurement on (a). (d) CLEAN deconvolution algorithm [3] applied to (c) using 15 iterations with a loop gain of 1. [2].

One possibility for the observed unexpected response can be that the sidelobes of the individual responses were coherently added between the two targets' responses. A second possible reason is that the illuminating noise signals experienced multipath effect where the received signals is not the direct reflection but an accumulation of reflections from one target to the next. Two modified measurements based on Fig. 3.4(a) were conducted: the first measurement separated the two spherical targets further apart such that the sidelobes overlapping effect in question will not be significant and the second measurement placed RF absorbers between the two targets to eliminate any multipath effect in question. However, neither of the two measurements mitigated the unexpected artifact and are not shown for brevity. Nevertheless, a data-drive correction was investigated. In this correcting approach, the mean of the reconstructed image is defined as $\hat{\mu}_{recon}$ and was subtracted from the reconstruction (Fig. 3.4(c)) yielding a clearer visual contrast as shown in Fig. 3.5(a) but still did not mitigate the unexpected response. The same approach was also applied to the deconvolved reconstruction (Fig. 3.4(d)) where the mean of all information determined by the CLEAN algorithm $\hat{\mu}_{clean}$ was subtracted yielding a further refined reconstruction where the unexpected response was significantly mitigated as shown in Fig. 3.5(b) and the slight shift in the positions of the responses showing better alignment with the actual locations of the spheres.

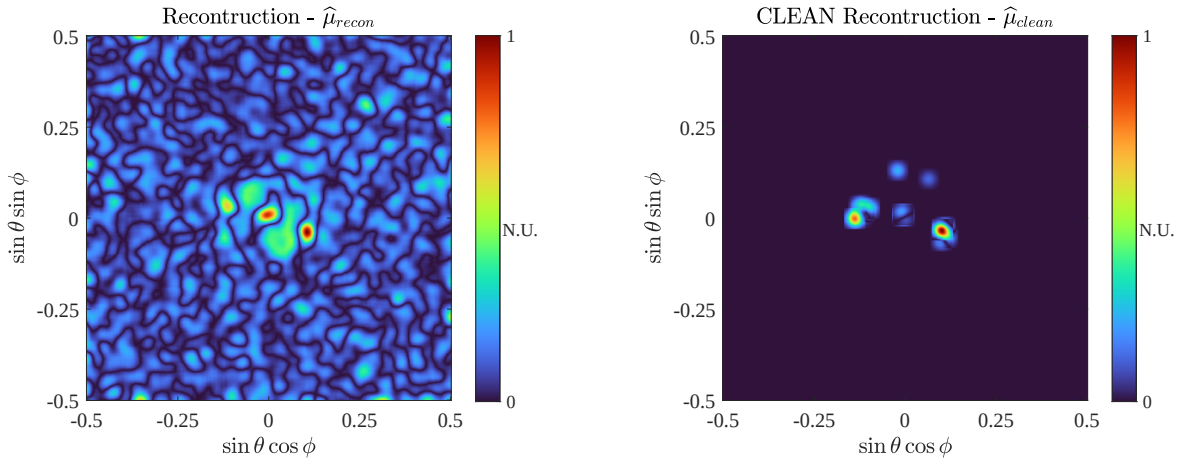

(a) (b)

Figure 3.5: (a) Further processing on the reconstruction of Fig. 3.4(c), by removing the mean of the magnitude among all information from the entire reconstructed scene, $\widehat{\mu}_{recon}$. (b) Further processing on the deconvolved reconstruction of Fig. 3.4(d), by removing the mean of the magnitude among all information determined by the CLEAN algorithm, $\widehat{\mu}_{clean}$. The artifact between the two sphere responses is reduced, and the slight shift in the positions of the responses more closely aligns to the actual locations of the spheres. [2].

CHAPTER 4

IMAGELESS CLASSIFICATION WITH ROTATIONAL DYNAMIC ANTENNA ARRAY

In this chapter, a novel rotational dynamic antenna array concept is presented and discussed where the rotational dynamics are used to synthesize a ring-shaped sampling function in the spatial frequency domain, providing a framework for imageless sharp-edged detection. Shown as an illustrative comparison in Fig. 4.1, a conventional image-based classification approach requires a fully reconstructed imagery of the scene. In contrast, the proposed imageless concept seeks to leverage specific dynamics (rotation) of antenna array to sample significantly less information in the whole spatial frequency domain that are specific to sharp edge related structures/objects. The aspect of sampling only the desired features in the spatial frequency domain not only enable classification to be implemented without a fully formed image but also prevent undesirable reconstruction of the scene as the required data for the imageless classification concept are insufficient for proper image reconstruction.

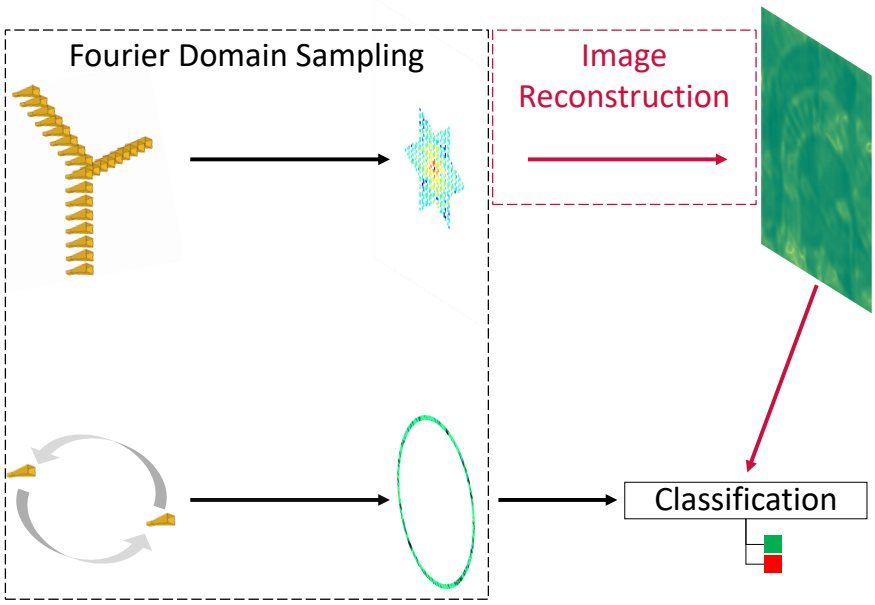

Figure 4.1: Illustrative comparison between image based classification that requires reconstruction and the proposed imageless classification where the image reconstruction process can be eliminated.

In the first half of this chapter, the idea of imageless classification is described in detail which includes the dynamic dependent spatial frequency sampling point and the synthetization of a ring-shaped sampling function (ring filter). The ring filter is designed to observe around the complete uv-plane at a specific zone of spatial frequency samples such that features related to the sharp edge structures/objects can be identified directly using the measured samples. Subsequently, a simulation-based study that aims to distinguish natural and non-natural scenes from available radar images is also described to demonstrate the potential of the imageless classification concept using a two-element rotational dynamic antenna array [1]. Furthermore, different classifiers are discussed as alternative and/or improvement for the design of imageless classification using a rotational dynamic antenna array. In the second half of this chapter, the two-element rotational dynamic antenna array introduced in Section 2.3 was used to experimentally validate the imageless classification concept by tracking the particular spatial frequency features that are related to sharp edges for six targets [5] along with an additional measurement to demonstrate the potential for concealed contraband detection application [6].

4.1 Direct Classification in the Spatial Frequency Domain

Sharp edges in a scene manifest broad spatial spectral responses that are localized at specific spatial frequency angles orthogonal to the edges' direction and extend radially outward in the uv-plane. If these spatial frequency responses (features) can be detected, direct classification in the spatial frequency domain is possible which not only eliminate the dependence on reconstructing images but can also reduce the hardware cost of the dynamically rotated linear antenna array where only two antennas are required. By rotating the pair of antennas with regard to their centroid, a fine ring-shaped sampling function (ring filter) is generated to track around the two-dimensional uv-plane where the perimeter of the ring filter is orthogonal to the radially extended spatial frequency features associated to structures/objects that have sharp physical edges.

Shown in Fig 4.2 is an illustrative example for a two-element rotational dynamic antenna array. As the dynamic antenna array rotates, the spatial frequency domain sampling point also changes accordingly where a fine ring filter [69] can be obtained assuming fast rotational dynamics and sufficient sampling rate [1]; four selected instances corresponding to different rotational angles are shown to demonstrate the relationship between the rotational dynamics dependent antenna pattern and the spatial frequency domain sampling points. One possible way to synthesize such fine ring filter is by rotating the two receiving antennas, fixed at a baseline D_λ, with regard to their centroid as shown in Fig. 4.3 where a half (180°) rotation in the spatial domain represents a full synthesized ring filter in the spatial frequency domain with a radius of D_λ $\mathrm{cycles} \cdot \mathrm{rad}^{-1}$ (diameter of $2D_\lambda$ $\mathrm{cycles} \cdot \mathrm{rad}^{-1}$). The dynamic motion of the two receiving antennas creates a spatial frequency filter that can be particular to man-made structures/objects in scenes and can thus support differentiation between natural and man-made structures/objects without the need to process a full image and requires significantly less hardware than image-based approaches requiring array of antennas. In addition to the benefit of requiring far less hardware, this method does not suffer from challenges with blurring as encountered in synthetic aperture radar (SAR) imaging when moving objects appear within the ground scene of interest, assuming the rotational dynamics are considerably fast.

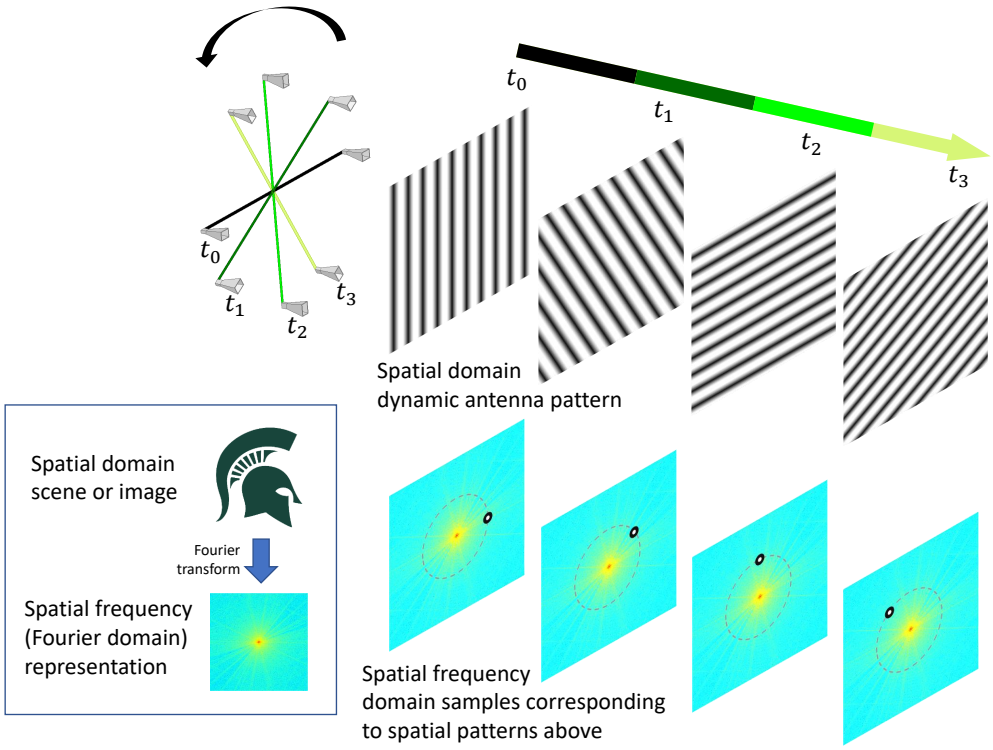

Figure 4.2: As the two-element dynamic antenna array rotates, the measured spatial frequency point also rotates. This is demonstrated with four different instances where t_0 corresponds to initial position, t_1 corresponds to 30°, t_2 corresponds to 90°, and t_3 corresponds to 120° counter-clockwise rotation from the initial position. [1].

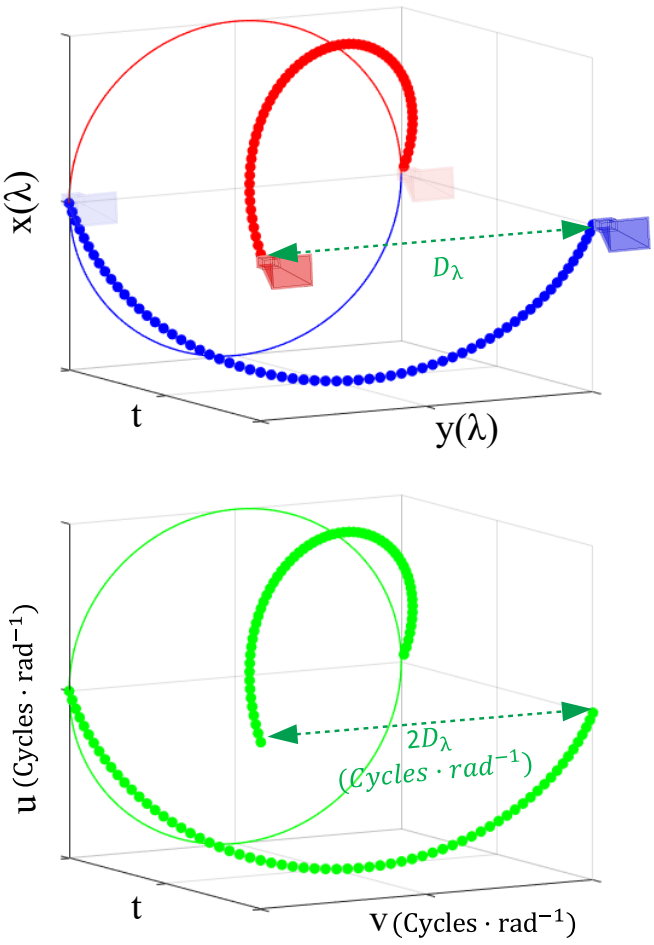

Figure 4.3: Top: Rotational dynamics of a two-element array where the receiving antennas (red/blue) are separated by D_λ for half (180°) rotation in counterclockwise direction. Bottom: Corresponding synthesized spatial frequency sampling function corresponding to the same instances of the array's rotational dynamics where every half rotation (180° rotation) yields a complete ring filter, hence, a full rotation of the dynamic antenna array synthesizes two complete ring filters. Note that a rotated baseline of D_λ corresponds to a ring filter of radius D_λ cycles $\cdot$ rad^{-1} (diameter of $2D_\lambda$ cycles $\cdot$ rad^{-1}) and the correlation between the dynamic antenna array and the synthesized ring filter's counterclockwise rotational dynamics.

The idea of performing imageless classification directly in the spatial frequency domain using only the ring-filtered samples was simulated using existing sets of measured microwave radar imagery to demonstrate the ability to classify scenes that are natural (e.g., forest, waterbody, etc.) and scenes that include man-made structures/objects (buildings, roads, etc.) using the two-element rotational dynamic array sensing system as previously described. Beyond remote sensing application, this particular concept can be applied to short-range sensing applications such as concealed contraband detection. Microwave radar aerial images of ground scenes were obtained and considered to explore the feasibility of direct classification in the spatial frequency domain with the goal of distinguishing between natural scenes (NS) without man-made structures, and non-natural scenes (NNS) comprising man-made structures/objects such as buildings and/or roadways. The described application is generally applicable to a broader set of microwave and millimeter-wave use cases; the particular set of microwave ground images were selected for the following reasons: large data sets of ground scenes captured by SAR are available, allowing sufficient data to conduct rigorous statistical analysis of the proposed imageless ring-filter based classification; radar images selected from [4] were processed to establish a common image resolution of 1 m/pixel. Furthermore, the described rotational dynamic antenna array concept is proposed for implementation at millimeter-wave frequencies, hence, microwave radar ground images provide similar resolutions and reflectivity to the ones obtained at lower millimeter-wave frequencies (i.e., 40 GHz, which neighbors the implemented dynamic antenna array at 38 GHz as discussed in Section 2.3). Finally, a system implementation near 40 GHz of a two-element antenna array with spatio-temporal dynamics provides image resolution and field-of-view that are commensurate with the chosen data set is explored for ground-based scene classification. Note that while the use of measured SAR data sets is not a precise model of the presented implementation, the contention is that this approach is the most reasonable for exploring the feasibility of the imageless spatial frequency subspace scene classification method.

The enabler for the sparse spatial frequency domain scene classification without full image reconstruction is based on the prominence of spatial frequency domain features that are present

in non-natural scenes (NNS) but absent in natural scenes (NS). In particular, scenes with sharp edges, commonly associated with man-made structures/objects but infrequent in natural scenes, manifest strong discrete directional signals in the spatial frequency domain where such discrete directional components are generally not apparent for natural scenes. Examples of natural scene (NS) type imagery represented by region of vegetation and non-natural scene (NNS) type imagery comprised of highway and buildings that have a spatial field-of-view of 1000 m by 1000 m are shown in Fig. 4.4(a) and (b) along with their corresponding visibility in Fig. 4.4(c) and (d). The visibility of NS shows smoother spatial frequency content while the visibility of NNS presents strong discrete directional components; these discrete directional components are oriented orthogonal to the direction of the sharp edges of the associated structures/objects in the spatial domain scene. For the fact that these components are discrete and manifest in highly directional orientation enables a relatively simple method of classifying between NS and NNS using only a small subset of visibility data that can be captured by the previously described ring filter.

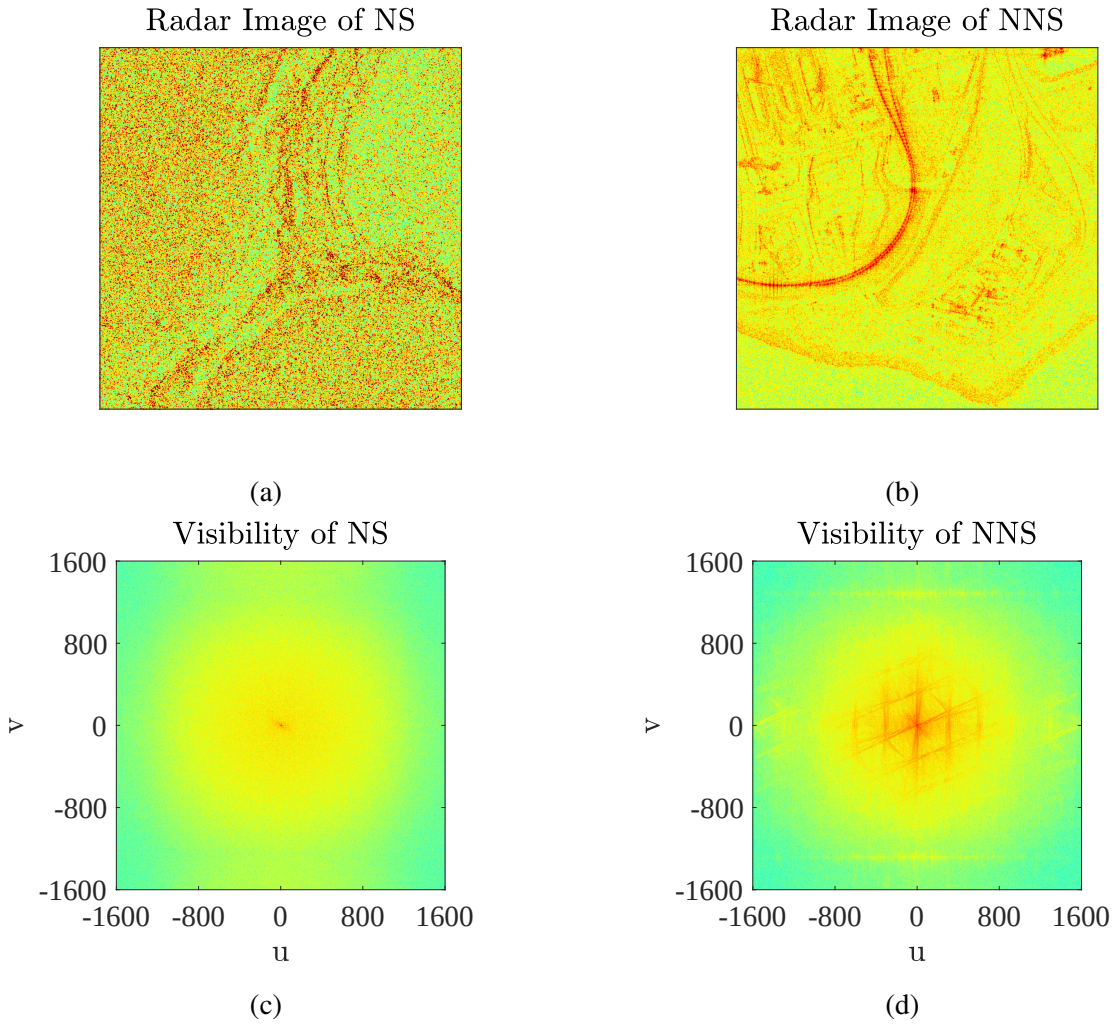

Figure 4.4: Microwave radar images of (a) a natural scene (NS) of a vegetation region of Campo Grande, Brazil and (b) a non-natural scene (NNS) of highway and building cluster from region of Port Hedland, Western Australia with their corresponding visibility in (c) and (d), respectively (data from [4]). [1].

The described ring filter, synthesized by a two-element rotational dynamic antenna array, is capable of sampling a ring of scene visibility in the uv-plane at a given radius related to the baseline separation, providing the ability to detect the discrete changes in visibility response as a function spatial frequency domain angle that can be found in NNS data but absent in NS data. An alternative way to generate the ring filter using two receiving antennas as to the one described in Fig. 4.3 is to place the first antenna at the center of a circle and that a second antenna is placed to move on the parameter of the circle where the circle's radius is the physical baseline separation matching the center spatial frequency of the spatial spectral bandwidth of the ring filter. Similar to the co-rotating concept, by cross-correlating the received signals between the outer antenna and the center antenna, a ring filter can be obtained. This concept is demonstrated in Fig. 4.5(a) representing the ring filter synthesized by fast rotational dynamics and sufficient sampling rate with an illustration of only 30 discretely sampled angles from the rotational dynamics and the corresponding spatial frequency samples shown in Fig. 4.5(b) and (c) for discussion of the ring filter's composition. It can be seen that the physical separation between the center antenna and the outer antenna corresponds to the radius of the radius of the ring filter in the uv-plane; the particular ring filter segment shares the same direction as the relative spatial angle between the two receiving antennas; and that a half rotation in the spatial domain corresponds to a full ring of sampling function in the spatial frequency domain. These relationships are the same as observed from the co-rotated dynamic antenna array shown in Fig. 4.3 as expected that unique spatial frequency sampling points are determined by baseline separation and orientation. Most importantly, shown in the right-hand side of Fig. 4.5(b) is the thickness aspect of the spatial frequency domain ring filter where the median radius is dependent on the center frequency in addition to the baseline separation and that the extension outward and inward represents the sampled spatial frequency region that are due to the elected antenna hardware's bandwidth.

The effective sampling function representation of a single ring filter can be represented by modifying the described expressions, (2.7)–(2.10), of the rotational dynamic sparse linear array in Section 2.2.1. For the fact there is only one baseline separation being considered for a ring filter,

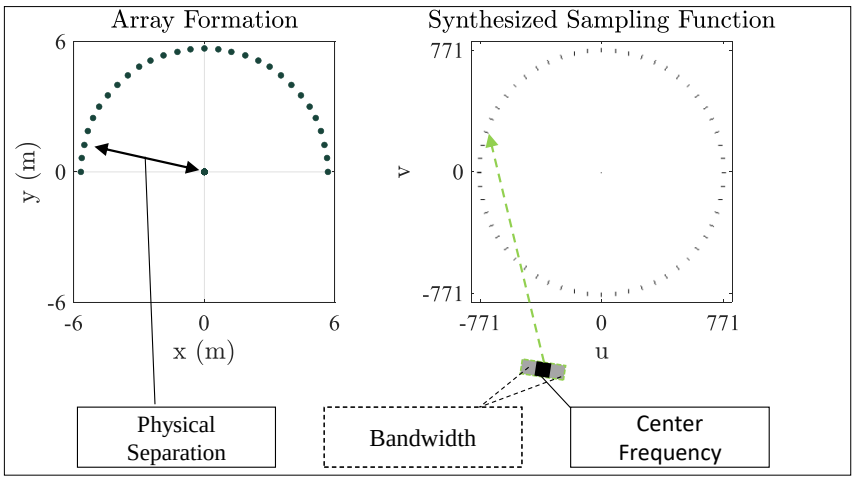

Figure 4.5: (a) Example of a proposed ring filter with a radius of 761 $\text{cycles} \cdot \text{rad}^{-1}$. (b) 30 discrete sampling instances of the two-element rotational dynamic antenna array (left) and the corresponding discretely synthesized ring filter (right). The black double arrow in (b) denotes the physical separation, or baseline between the two receiving antennas. The corresponding segment of the resulting sampling function is in the same direction as annotated by the green dashed arrow. The thickness of the ring filter within the uv-plane is dependent on both the center frequency of the sensing system and the bandwidth of the elected antenna hardware as annotated by the solid and dashed lines right below, respectively. [1].

(2.7) and (2.8) reduces to the following

$$u_k = D_{ring} \sin(\gamma(k)), \tag{4.1}$$

and

$$v_k = D_{ring} \cos(\gamma(k)), \tag{4.2}$$

where D_{ring} is the single selected baseline between the two receivers and terms described by (2.9) remain unaltered. Thus, the ring filter specific sampling function of the two-element rotational dynamic antenna array can be given by

$$S_{ring}(u, v) = \sum_{k=0}^{K-1} \delta\left(u - u_k\right) \delta\left(v - v_k\right). \tag{4.3}$$

The design of the specific baseline and spatial frequency bandwidth of the described ring filter is dependent on the application such that the ring filter is within a spatial frequency region where the useful discrete, broadband spatial spectral signals have adequate signal strength

compared to surrounding visibility information. In general, scenes contain a significant amount of visibility information at low spatial frequencies, meaning that strong visibility contents appear near the location ($u = 0, v = 0$), as demonstrated in Fig. 4.4(c), thus it is beneficial to design the ring filter with a radius beyond the strong low spatial frequency content, but still sufficiently near the discrete signals of interests whose signal strength are still adequately strong for detection. For the selected data set, as suggested by the visibility data shown in Fig. 4.4(d), a ring filter covering a spatial spectral bandwidth near $700 - 800$ cycles $\cdot$ rad^{-1} is desired. It was determined heuristically that the discrete spectral signals still exhibit good signal strength near 761 cycles $\cdot$ rad^{-1} when comparing to the surrounding visibility. Applications of different scenes will be associated with different visibility distribution, therefore affecting design decision such as the spatial spectral bandwidth of the ring filter, the rotational dynamic antenna array's frequency, and the physical baseline all need to be considered for application specific use case.

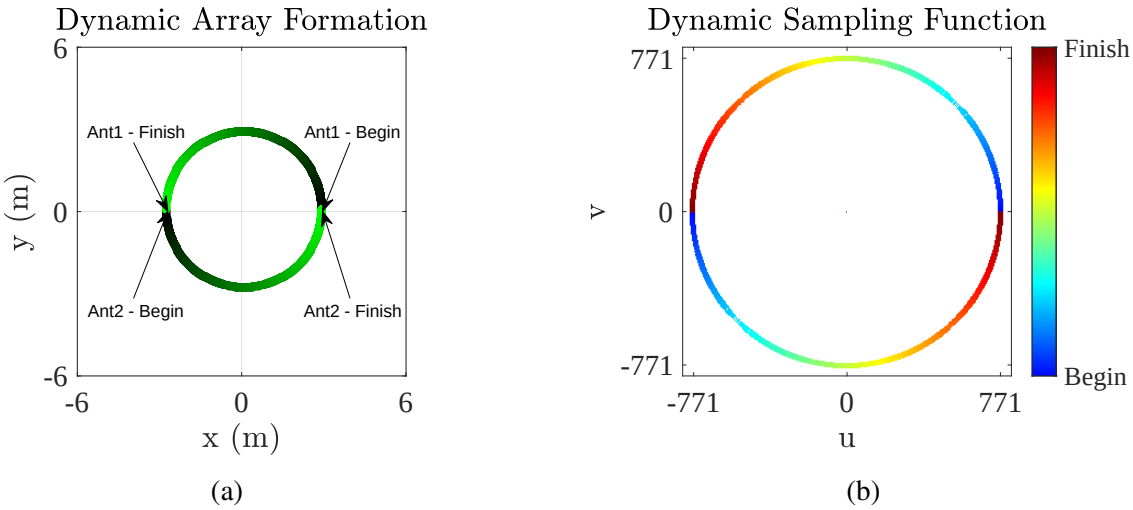

Figure 4.6: Array dynamics and sampling function formation using the single platform concept shown in 4.9. (a) Dynamic array formation due to the movement of two antennas. (b) Corresponding elapsed sampling function. [1].

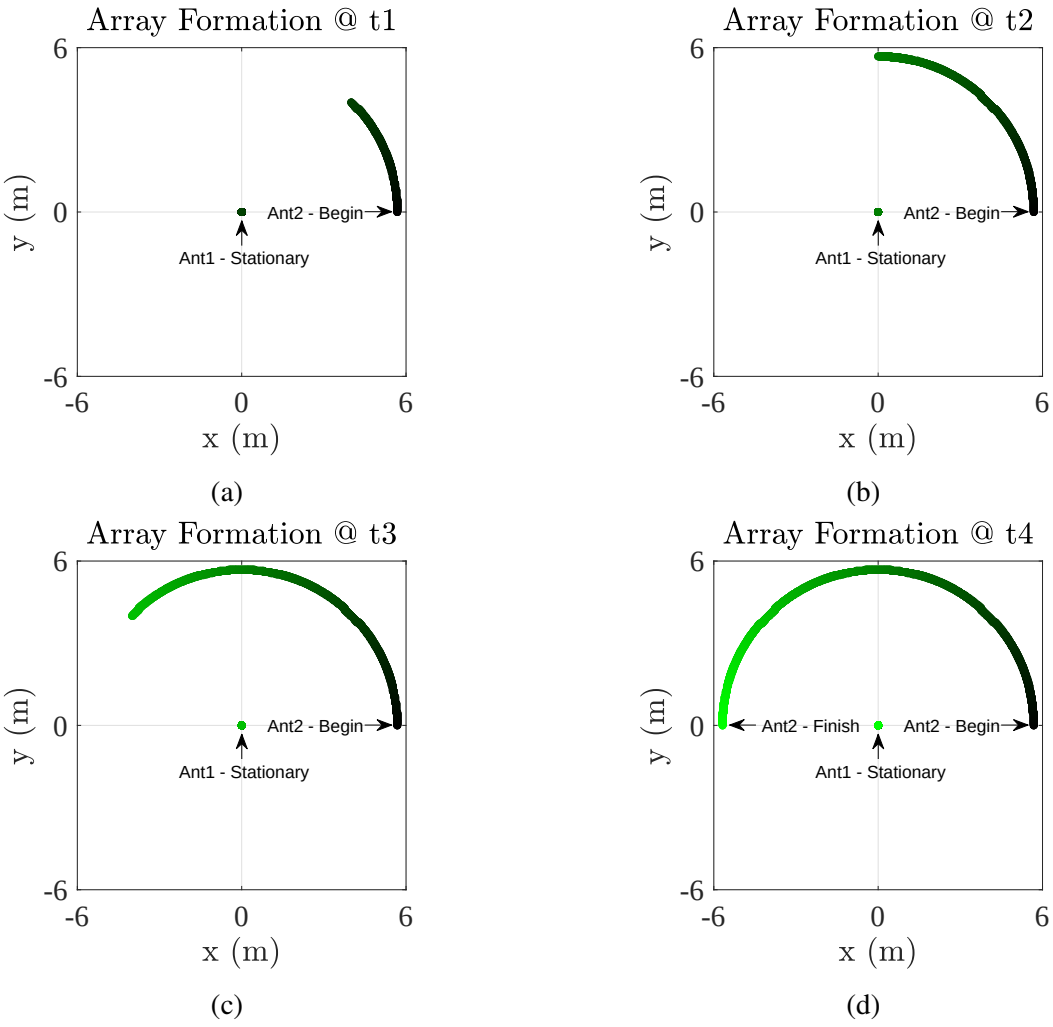

Figure 4.7: Formation of the spatial frequency sampling function using two receiving antennas with one fixed at the center of a semi-circle and the second moving along the semi-circular path. (a)-(d) Representation of the cumulative array formations over a full semi-circular path at four different instances. [1].

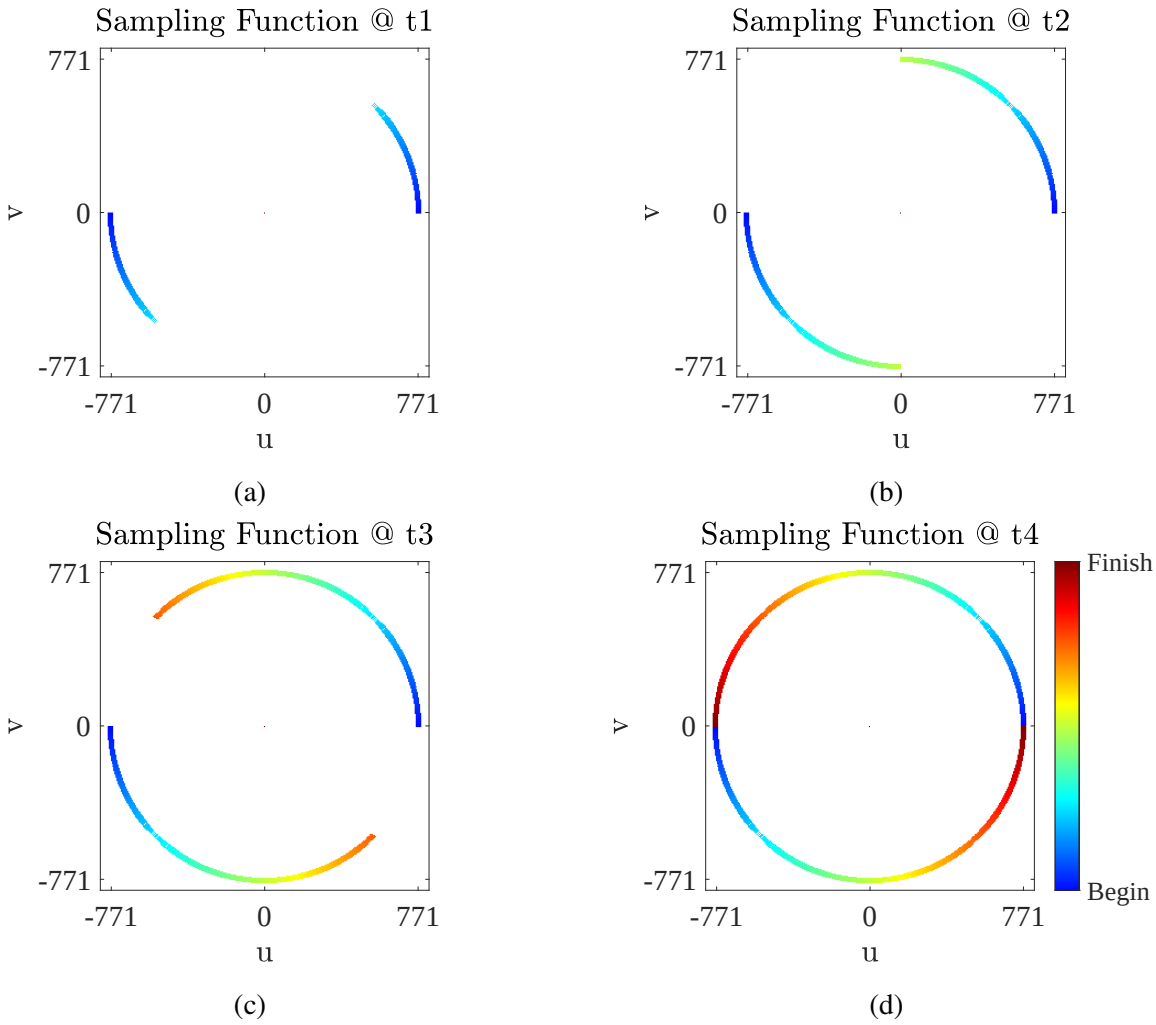

Figure 4.8: (a)-(d) Representation of the synthesized spatial frequency sampling function correspond to the four instances as shown in Fig. 4.7(a)-(d). [1].

As the design of the rotational dynamic antenna array concept can be application dependent, despite the fact the single platform co-rotated implementation was the most suitable design for the works discussed in this thesis, it is also important to describe other possible design options knowing that application specific requirements or constraints can deem them useful. So far, two types of rotational dynamics using a two-element dynamic antenna array have been presented: the co-rotated implementation as shown in Fig. 4.3, or the "fixing one moving the other" mentioned in Fig. 4.5 during the ring filter discussion. The former requires a smaller implementation footprint when considering the same baseline separation between the antennas (Fig. 4.6(a) versus Fig. 4.7(a)); this approach also benefits from wider antenna selection because co-polarization can be ensured by enabling the two antennas to move collaboratively as presented in Section 2.3. In contrast, the latter implementation will constrain antenna selection to circularly polarized antennas to ensure co-polarization. Both concepts require no reset of the antennas' positions, i.e., continuing the rotational dynamics will synthesize the same ring filter hence each successful revolution on the dynamic antenna array will yield two complete ring filters. This aspect is demonstrated in Figs. 4.7 and 4.8 for the "fixing one moving the other" implementation where the former shows four sequential elapsed array formations from (a)-(d) and the latter shows the corresponding synthesized sampling function at the same instances from (a)-(d). By allowing the moving antenna to continue through the other half of the circular path, a second ring filter can then be generated. Similarly, the dynamic array formation and associated dynamic sampling function shown in Fig. 4.6 also suggest that by allowing the two moving antennas to continue through the other the other half of the circular path, a new ring filter is thus obtained.

Building on top of the co-rotating implementation shown in Fig. 4.6, a possible single platform implementation is shown in Fig. 4.9 where the two receiving antennas are implemented on the rotor blades of aerial vehicle that can provide sufficient spatial coverage for the desired spatial frequency ring filter. In this particular implementation, appropriate sampling is ensured because the receiving antennas remain co-polarized and that either an active or passive type interferometric sensing approaches can be elected which is application specific. While single-platform

design can be feasibly compact by placing the two receiving antennas on the same platform, for certain applications, implementation requiring multiple platforms might be preferred. For example, multi-platform distributed array concepts can be beneficial [61, 62] as single source of failure can be easily remedied due to the ability to wirelessly coordinate the operations of sensors carrying distributed platforms [70–72]. This is demonstrated in Fig. 4.10 where three platforms each carrying a receiving antenna can move collaboratively to obtain the ring filter using only half of the time when comparing to Figs. 4.7. While platform 1 in Fig. 4.10 remains stationary, the other two platform (2 and 3) each complete half of the semicircular path as shown in Fig. 4.11(a) and (c) that will each synthesize non-overlapping sampling points in the spatial frequency domain as shown in Fig. 4.11(b) and (d), respectively. The reduction of ring filter generation time is due to the additional third platform/antenna to synthesize non-redundant segments of the ring filter. This particular idea of adding additional platforms can thus be extended beyond three and remains a topic for application specific design.

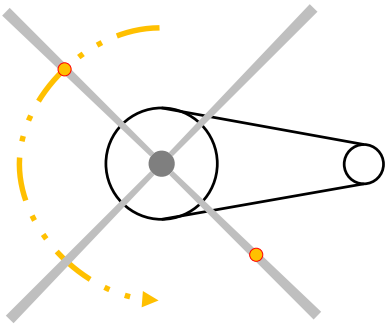

Figure 4.9: Illustration of a notional dynamic array implementation using the concept shown in Fig. 4.6 on a platform with rotors. [1].

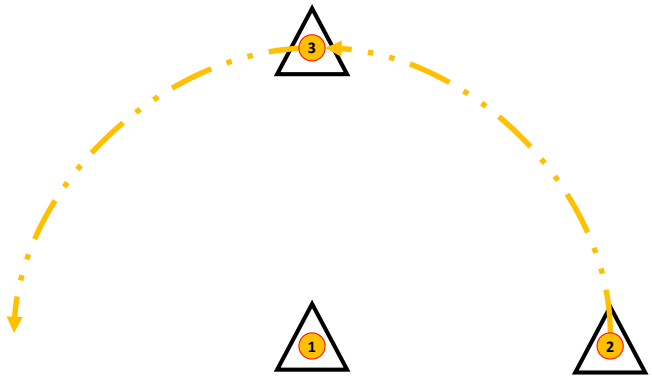

Figure 4.10: Illustration of a multiple platform concept to acquire the ring filter. Each platform noted by 1, 2, and 3 consists of one integrated antenna. Platform 1 holds stationary, while 2 and 3 move around the segmented semicircular path with respect to platform 1. [1].

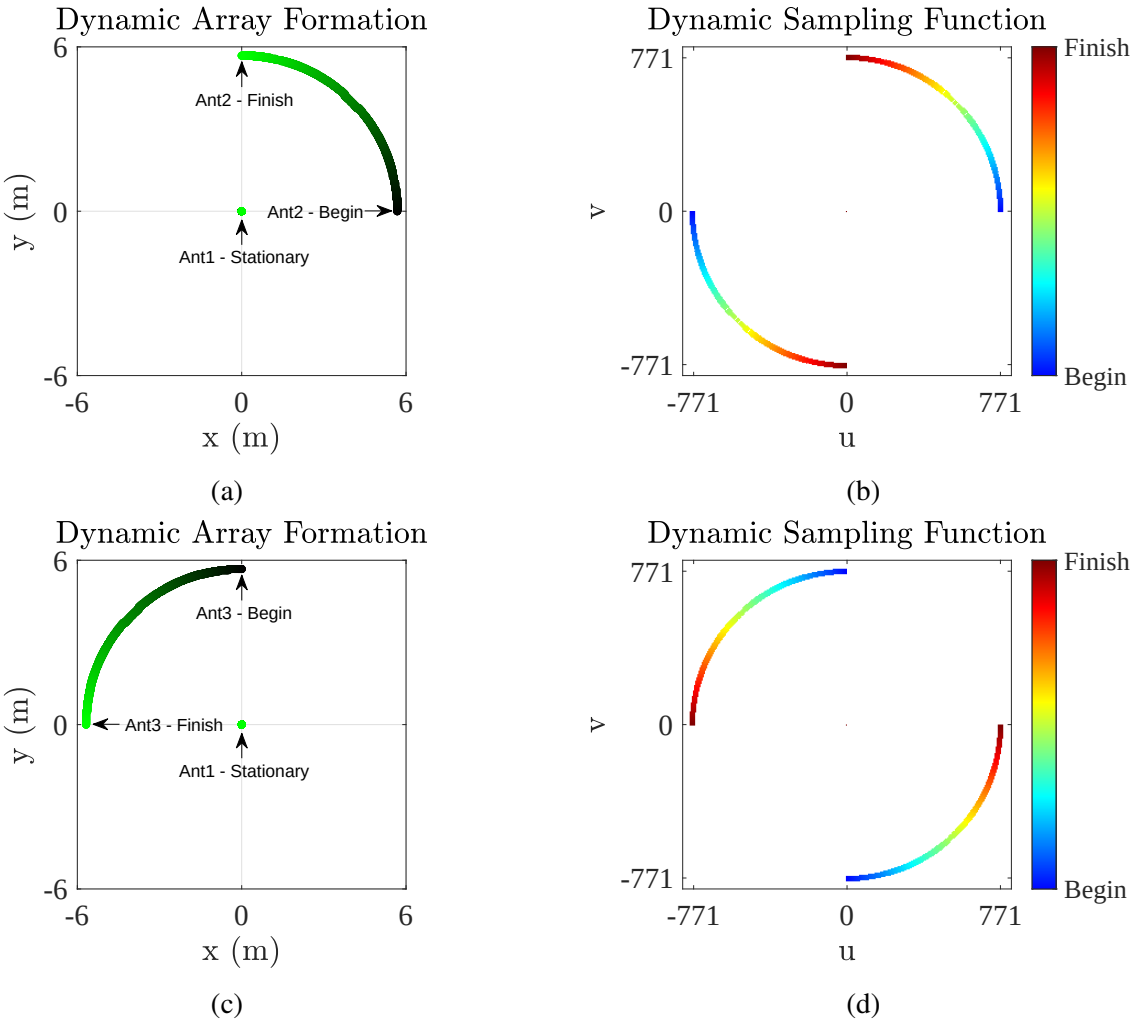

Figure 4.11: Dynamically synthesized sampling function using three receiving antennas integrated separately on three platforms as shown in Fig. 4.10. (a) Dynamic array formation with counter-clockwise antenna (Ant2) movement in the first quadrant on the xy-plane and (b) the corresponding dynamic sampling function formed in counterclockwise direction in the first and third quadrant on the uv-plane. (c) Dynamic array formation with counterclockwise antenna (Ant3) movement in the second quadrant on the xy-plane and, (d) the corresponding dynamic sampling function formed in counterclockwise direction in the second and fourth quadrant on the uv-plane. [1].

To refine the two-element rotational dynamic array concept by consider a millimeter-wave array amenable to implementation on the co-rotating rotors of a compact aerial vehicle, a center frequency of 40 GHz, a bandwidth of 3%, and an antenna half-power beamwidth θ_{BW} of 60° were considered. The considered beamwidth commensurate with the beamwidth of a planar patch antenna that can be reasonably implemented conformally on the underside of the rotors [68, 73, 74]. Using these parameters, a design approach to balance feasible antenna separation and aerial platform altitude to maintain a ground scene resolution of 1 m, which is commensurate with the processed data from [4]. The one-dimensional spatial resolution $\Delta\theta$ of a single antenna is related to the antenna beamwidth as

$$\Delta\theta = \frac{\tan\theta_{BW}}{R}, \tag{4.4}$$

where R represents the distance between the antenna and the point of interest which is the altitude when considering an airborne based implementation. For a two-element array, the spatial resolution is governed by the maximum antenna baseline D_{max} and wavelength λ as described in [37]

$$\Delta\theta \approx 0.88 \cdot \frac{\lambda}{D_{max}}. \tag{4.5}$$

Thus, for the considered parameters, the relationships between altitude, baseline, and antenna beamwidth are shown in Fig. 4.12 which was generated using (4.4) and (4.5). With the stated assumptions, the calculated altitude is approximately 886 m, and the calculated baseline is approximately 761 λ which translates to a physical separation of 5.7 m. The calculated altitude and the required physical dimension resemble that of a typical specification of a medium sized unmanned aerial vehicle (UAV) as described in [75] where an average end to end rotor blade length (wingspan) is $5 - 10$ m. Thus, the proposed concept is amenable to be implemented on research/industrial-grade UAV helicopters such as the StarLite-2A [76]. For a physical separation fixed at 5.7 m, an antenna of 3% bandwidth sill contribute to a spatial frequency range between 751 λ and 771 λ at 40 GHz as shown in TABLE 4.1.

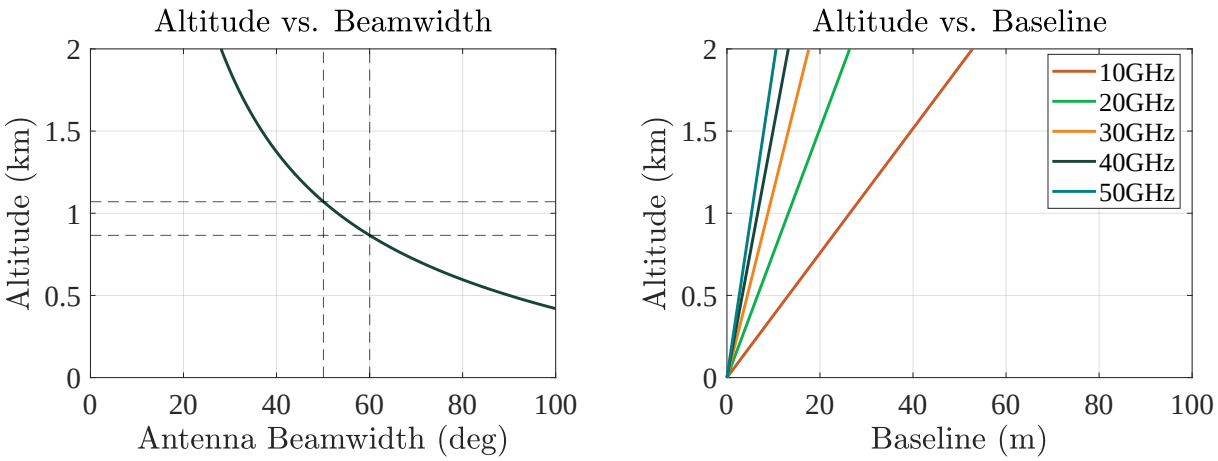

(a) (b)

Figure 4.12: (a) Altitude versus antenna beamwidth, with markers indicating beamwidth values between 50°and 60°, matching that of a feasible patch antenna. (b) Altitude versus maximum system baseline for center frequency of 10 GHz, 20 GHz, 30 GHz, 40 GHz, and 50 GHz. [1].

Bandwidth	Frequency	Wavelength	Baseline
-1.5%	39.4 GHz	7.6 mm	751 λ
$\pm 0\%$	40.0 GHz	7.5 mm	761 λ
$+1.5\%$	40.6 GHz	7.4 mm	771 λ

Table 4.1: Assumed system parameters with a center frequency of 40 GHz and a bandwidth of 3%. [1].

4.1.1 Imageless Classification using Single Ring Filter

4.1.1.1 Threshold-Based Decision Boundary

A simulation-based analysis using a single spatial frequency ring filter to the classification of ground scenes in discussed. The objective for the classifier is to demonstrate the ability to distinguish between NSs, which as previously stated, lack of strong broad spatial spectral responses shown in Fig. 4.4(c), and NNSs containing man-made structures/objects generating such features shown in Fig. 4.4(d). The analysis demonstrates that the broad spatial spectral responses of man-made structures/objects are sufficiently persistent in a large set of real-life data where the described two-element rotational dynamic antenna array can be designed such that capturing the desirable spatial frequency information is possible and enables direct classification without image formation. For each ring-filtered visibility, a one-dimensional signal is calculated by averaging the ring-sampled visibility at every rotation angle within the filtered output, providing a measure of the radial spatial frequency intensity residing in the designed ring filter bandwidth as a function of angle in the uv-plane. In general, visibilities of NS demonstrate comparably fewer variations as a function of angle than the visibilities of NNS. The data set described in Section 4.1 was divided into training and testing subsets where standard metrics were calculated based on statistical measures of the resulting signals from the training subset. These metrics are used to determine features that yield the most separation between the probability distributions of the two classes in consideration (NS and NNS); ideally, larger separation represents better potential for successful classification. From a set of the most prominent features, analytical threshold values were determined and compared to an "ideal" threshold calculated empirically by evaluating all thresholds over the entire data set. For evaluation of the classification performance, standard set of metrics are used which include the true positive rate (TPR) that indicates actual positives that are correctly identified; the true negative rate (TNR) that indicates actual negatives that are correctly identified; the positive predictive value (PPV) that indicates actual positives in proportion to all identified positives; the negative predictive value (NPV) that indicates actual negatives in proportion to all identified nega-

tives; the accuracy (ACC) that provides insight to the measure of all the correctly identified cases; and the F1 Score (F1) that is the harmonic mean between PPV and TPR that gives a measure of the incorrectly classified cases than ACC [77, 78]. These metrics are defined as follows:

$$\mathrm{TPR} = \frac{\mathrm{TP}}{\mathrm{TP} + \mathrm{FN}}, \tag{4.6}$$

$$\mathrm{TNR} = \frac{\mathrm{TN}}{\mathrm{TN} + \mathrm{FP}}, \tag{4.7}$$

$$\mathrm{PPV} = \frac{\mathrm{TP}}{\mathrm{TP} + \mathrm{FP}}, \tag{4.8}$$

$$\mathrm{NPV} = \frac{\mathrm{TN}}{\mathrm{TN} + \mathrm{FN}}, \tag{4.9}$$

$$\mathrm{ACC} = \frac{\mathrm{TP} + \mathrm{TN}}{\mathrm{TP} + \mathrm{FN} + \mathrm{TN} + \mathrm{FP}}, \tag{4.10}$$

and

$$\mathrm{F1} = 2 \cdot \frac{\mathrm{PPV} \cdot \mathrm{TPR}}{\mathrm{PPV} + \mathrm{TPR}}. \tag{4.11}$$

For a ring-sampled visibility, the filtered spatial frequencies can be transformed into a one-dimensional vector S_s such that the average response at each angle that spans around the complete uv-plane, given by

$$S_s(\gamma) = \frac{\sum_{r=M}^{N} V_s(r\cos(\gamma), r\sin(\gamma))}{N - M}, \tag{4.12}$$

where γ denotes the angle with respect to the positive u-axis, V_s represents the ring-sampled visibility, r represents the radius of the ring filter, N and M represent the furthest and closest uv pair that are sampled as the result of the ring filter's upper and lower bandwidth. Examples of the S_s vector is shown in Fig. 4.13(a) where the red and green responses represent the corresponding visibility shown in Fig. 4.4 (c) and (d) that were ring-filtered at 761 $\mathrm{cycles} \cdot \mathrm{rad}^{-1}$. Although apparent differences in S_s can be observed between NS and NNS, it is preferable to further compute the first derivative

$$S_s'(\gamma) = \frac{d}{d\gamma} S_s(\gamma), \tag{4.13}$$

for two reasons: the first derivative weight more on the changes in S_s that are associate more with the discrete nature of NNS and less on the smoother response from NS; furthermore, variations

in the magnitude are mitigated because the responses can fluctuate as different regions and/or operating conditions are encountered.

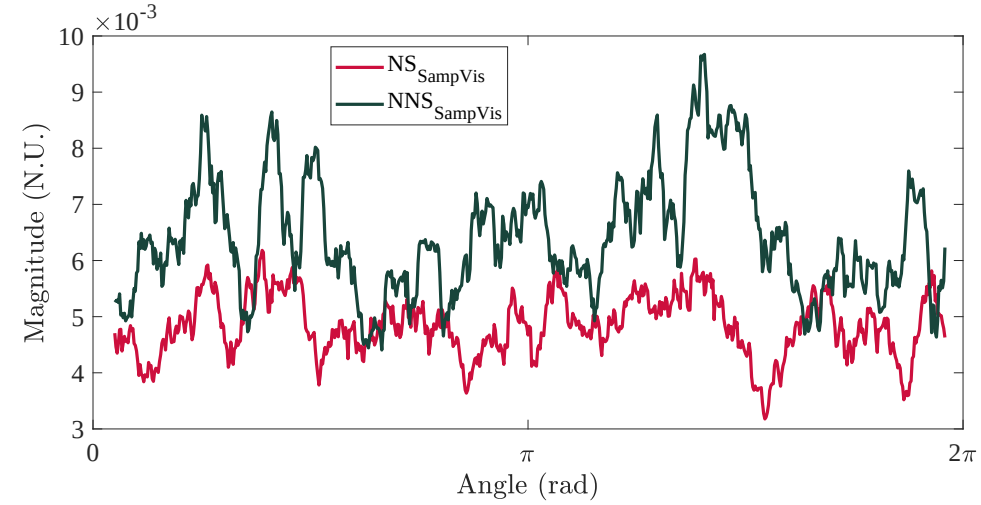

(a)

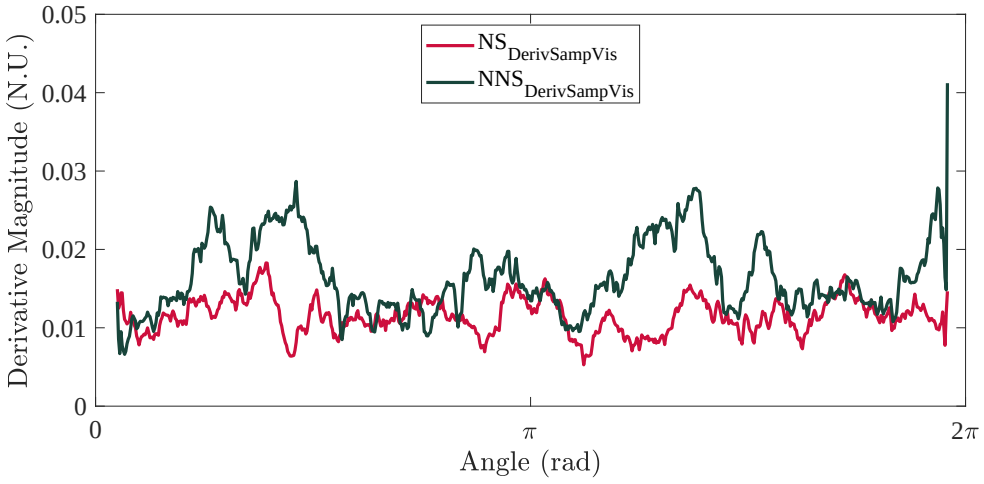

(b)

Figure 4.13: (a) Visualization of the transformed one-dimensional sampled visibility vector (S_s) of NS and NNS from Fig. 4.4 (a) and (b) by averaging the response at each angle with respect to the center of the uv-plane. (b) Corresponding first derivatives (S'_s). [1].

A set containing a total of 2076 microwave radar images from [4], including 1038 NS and 1038 NNS, were processed where corresponding two-dimensional Fourier transforms and the ring filter based on the described rotational dynamic antenna array design and the corresponding $S'_s(\gamma)$ were computed. Six simple statistics of the computed $S'_s(\gamma)$ were computed and compared to determine the best statistic that can be used to facilitate the binary classification between NS and NNS. The statics were the maximum, mean, median, minimum, standard deviation, and the variance of the computed $S'_s(\gamma)$ vector. Determination of the most desirable statistic was aided by computing the receiver operating characteristic (ROC) curve that is commonly used in binary classification to compare different potential features as classifier for their performance among a range of quantitative decision boundary by parametrically plotting their corresponding TPR against false positive rate (FPR) which can be easily obtain if the TNR is known [77] by the following:

$$\mathrm{FPR} = 1 - \mathrm{TNR}. \tag{4.14}$$

The ROC curves of the six potential statistics are shown in Fig. 4.14. For the fact that the distance

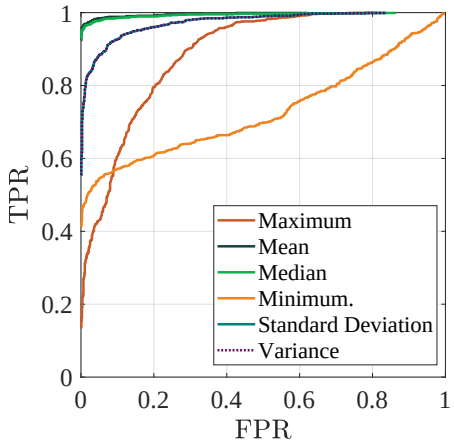

Figure 4.14: Receiver operating characteristic curves (ROC) of the selected statistics. Using the man as the binary classifier (i.e., NS and NNS) yields the best performance; followed by median, standard deviation/variance, maximum and minimum.

from a particular ROC curve to the top left corner (i.e., point (0,1)) represents how well the prediction outcome is for the particular statistic as classifier, it provides a good insight to select the

most desirable parameters for classification, which are in descending order mean, median, standard deviation/variance, maximum and minimum. Thus, a threshold-based decision boundary was computed using the mean value of the $S'_s(\gamma)$ vector as a function of angle

$$\mu S'_s = \mathrm{mean}\{S'_s(\gamma)\}. \tag{4.15}$$

Because the desirable discrete responses from NNS are stronger as shown in Fig. 4.13, the threshold was based on the maximum (NS) and minimum (NNS) values from the training set given by

$$\mathrm{T} = \frac{1}{2}\left(\max\{\mathrm{NS\_S'_s}\} + \min\{\mathrm{NNS\_S'_s}\}\right). \tag{4.16}$$

Using the threshold-based decision boundary, S'_s within testing set with $S'_s < \mathrm{T}$ are classified as NS, whereas $S'_s >= \mathrm{T}$ are classified as NNS. To address the potential bias by unintentionally selecting the best or worst-case scenario as a result of grouping specific training and testing set combinations, the Monte Carlo method [79] was elected by repeating the following three steps 1 000 000 times.

1. Approximately 70% of NS and NNS ring-filtered visibilities (727) are uniformly selected at random as the training set where the non-selected 311 (≈30%) forms the testing set.

2. The threshold-based decision boundary is computed using the testing set according to (4.16).

3. The calculated threshold is applied to the testing set for classification and the associated metrics note previously are calculated.

In practical applications, threshold-based decision boundaries are determined above using a training and testing set. To evaluate the threshold stated above, an ideal threshold value was determined by applying (4.16) to the full data set. Note that while this ideal threshold provides the best possible classification outcomes, it is however overfitted to the entire data set and thus is only useful for comparison of the analytical threshold above. The range of the ideal threshold is thus bounded by lowest and highest S'_s values among the 2076 ring-filtered visibilities. 1000 equally spaced steps between the determined upper- and lower-boundary were generated and applied to all 2076

ring-filtered visibilities. The results are shown in TABLE 4.2 where individual column represents the highest possible value of the specific classification metric with its associated values on other metrics and a normalized threshold for S'_s. Suppose that an application requires guaranteed classification of NNS (i.e., TPR $= 1.000$), the tradeoff will be a lower ACC of 0.667 and F1 of 0.750. Similarly, if an application requires guaranteed classification of NS (i.e., TNR $= 1.000$), the associated ACC and F1 will be 0.961 and 0.959, respectively. Of the various thresholds, a value of 0.613 N.U. (normalized units) provided the best performance among the various metrics. Shown in TABLE 4.3 are the comparisons of the analytical threshold and the aforementioned ideal threshold. The mean analytical threshold from the Monte Carlo simulations had a value of 0.158 N.U. which is close to the ideal threshold value of 0.163 N.U. that was calculated using the entire data set indicating that the described analytical approach for calculating the threshold is a reasonable sub-optimal approach. In Fig. 4.15, the probability density functions as function of S'_s for NS and NNS are shown where a clear null point between the distribution, an indication of a desirable location for choosing the threshold as decision boundary. The empirical ideal threshold and the analytical threshold are both near this null point, further supporting that the analytical approach can be expected to produce a desirable decision boundary. Furthermore, classification metrics between the mean analytical and empirical results are within 3% differences. Thus, the capability of a two-element rotational dynamic antenna array is demonstrated where imageless classification using spatial frequency domain information is demonstrated.

	TPR =1.000	TNR =1.000	PPV =1.000	NPV =1.000	ACC =0.979	F1 =0.979
TPR	-	0.922	0.922	1.000	0.968	0.968
TNR	0.334	-	1.000	0.334	0.990	0.990
PPV	0.600	1.000	-	0.600	0.990	0.990
NPV	1.000	0.928	0.928	-	0.969	0.969
ACC	0.667	0.961	0.961	0.667	-	0.979
F1	0.750	0.959	0.959	0.750	0.979	-
Threshold (N.U.)	0.139	0.177	0.177	0.139	0.163	0.163

Table 4.2: Metric interdependency using empirical threshold. [1].

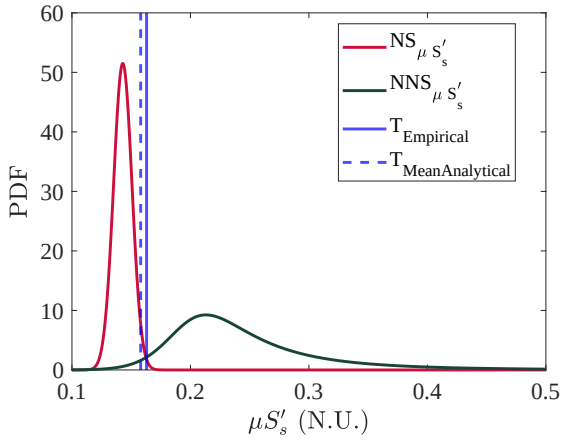

Figure 4.15: Probability density function of $\text{NS}_{\mu S'_s}$ (shown in red) and $\text{NNS}_{\mu S'_s}$ (shown in green) with the empirical and mean analytical threshold value shown in solid- and dashed-blue lines, respectively. [1].

	Empirical Value	Mean Analytical Value	% Error
T (N.U.)	0.163	0.158	3.1
ACC	0.979	0.971	0.9
F1	0.979	0.971	0.8
TPR	0.968	0.982	1.4
TNR	0.990	0.960	3.1
PPV	0.990	0.961	3.0
NPV	0.969	0.981	1.3

Table 4.3: Classification results using empirical and analytical thresholds. [1].

4.1.1.2 Alternative K-Nearest Neighbor Classifier

While the analytical threshold-based decision boundary yielded a reasonable classification result of an ACC of 0.971 and F1 of 0.971, it is inevitable to explore alternative approaches with an objective to improve the imageless classification performance. Therefore, the K-nearest neighbor (K-NN) classifier was elected as an alternative for the reason that the analytical threshold-based approach only relies on the two extreme patterns from the training set as described in (4.16) which might not be the most efficient approach to utilize the training set. For the considered binary classification (NS and NNS) with a large training set of N patterns, $N-2$ patterns will not be

utilized as a result of using (4.16). However, it is equally problematic to use all available patterns as outliers within the training set can also affect the outcome of computing a threshold-based decision boundary. The K-NN classifier was selected because it evaluates significant number of training patterns (by design choice) that are local to each of the individual incoming unknown pattern for classification. The K-NN classifier assigns the class of an unknown pattern by evaluating the K-nearest known patterns from the prototype (i.e., training set), where the final classification is determined by a voting mechanism such that the majority class type among the K-nearest neighbors is chosen [80, 81].

The same considerations as in the previous analytical based threshold simulation was used: system baseline of 761 $\text{cycles} \cdot \text{rad}^{-1}$, same 2076 data set from [4], and a 70%-30% training and testing data set split. For each incoming pattern's classification, the 37 nearest patterns, the closest odd integer as determined by K= $\sqrt{K_{training}}$, where $K_{training}$ is the total number of patterns in the training set (i.e., 737 NS and 737 NNS). An odd number of neighbors is particularly useful for binary classification problem to avoid a tie in the voting mechanism. A total of 100 Monte Carlo simulations were performed where the training and testing set between each iteration are randomized to avoid bias. Since the objective is to compare the overall ACC and F1, the averaged value from the 100 K-NN results and the corresponding mean analytical result of the threshold-based classifier is compared in TABLE 4.4 where an improvement of 0.75% was observed for ACC at 0.9780 and an improvement of 0.67% was observed for F1 at 0.9776. These improvements in performance further supported the ring filter based imageless classification approach that uses the two-element rotational dynamic antenna array concept.

Classifier	ACC	ACC Improvement	F1	F1 Improvement
Analytical Threshold	0.9705	-	0.9709	-
K-NN Classifier	0.9780	0.75%	0.9776	0.67%

Table 4.4: Comparison between the classification results using analytical threshold-based decision boundary and the K-NN classifier.

4.2 Experimental Identification Features Using Spatial Frequency Samples

In this section, experimental measurements were made to validate the specific spatial frequency features that are associated to structures/objects with sharp edges. Six measurements comprising simple shapes that contain one or more sharp edges were measured to better quantify the spatial domain attributes and their associated spatial frequency domain responses captured by a ring filter. Furthermore, a concealed contraband measurement was also conducted to consider clothing as an obscurant in a security application. Not only do the measurements validate the imageless concept that was only demonstrated by simulation in Section 4.1, but they also provide a proof-of-concept that the two-element rotational dynamic antenna array synthesized ring filter is capable of being applied to short-range sensing security application as shown in Fig 4.16. The same two-element rotational dynamic antenna array described in Section 2.3 was used for all measurement in this section. Furthermore, similar setup as described in the imaging measurements in Section 3.1 were also used. The differences are that only one baseline separation, namely $76\ \lambda$, between the two receiving antennas was used to synthesize a single ring filter in the spatial frequency domain and that a total of 180 angles in 1° increment were captured for a half spatial rotation which represents a full ring filter on the uv-plane. The measurements presented in this section uses the same code for processing as shown in APPENDIX B.1.

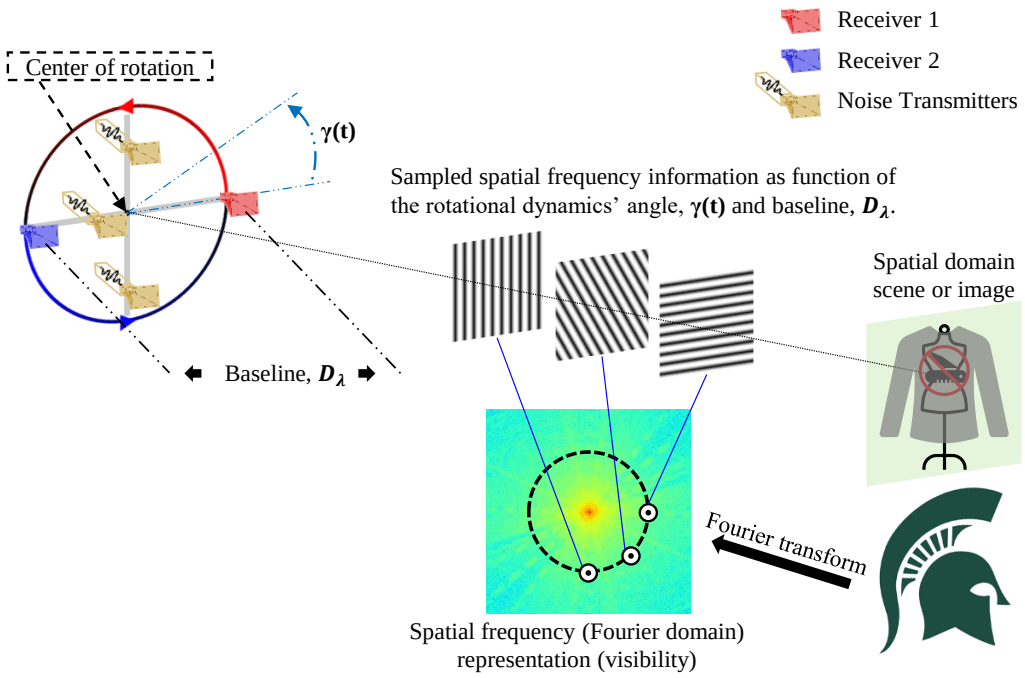

Figure 4.16: Overview of the imageless concept of the implemented millimeter-wave rotational dynamic antenna array. The two receiving antennas (red and blue) co-rotate in a counterclockwise direction with respect to their centroid to dynamically synthesized the proposed ring filter in the spatial frequency domain. The sampled spatial frequency information are dependent on the rotational dynamics' angle $\gamma(t)$ and the baseline separation D_λ between the two receiving antennas which is illustrated by the three far field grating lobe patterns in the middle of the diagram which corresponds to a specific spatial frequency sample point as illustrated on the visibility of the Michigan State University Spartan helmet. [5].

4.2.1 Shapes and Their Spatial Domain Attributes

Targets were fabricated using copper foil tape for the shapes and a foam board as background. The copper foil tape is highly reflective whereas the foam board is almost transparent at the operating 38 GHz. For this reason, the sharp contrast of reflectivity between the copper foil tape and the transparent background board enables the fabrication of shapes with identifiable spatial frequency features related to sharp edges that are intended to be validated using the imageless sparse Fourier domain sampling approach using the proposed ring filter synthesized by the two-element rotational dynamic antenna array.

The first measurement was a horizontal stripe as shown in Fig. 4.17(a) where the expected sharp edges related broad spectrum spatial frequency features are expected in orthogonal direction as demonstrated in the simulated visibility in Fig. 4.17(b). A ring-filtered visibility was simulated using the intended 76 λ baseline separation that is shown in Fig. 4.17(c) showing that the orthogonal spatial frequency features are still strong comparing to neighboring visibility information. In Fig. 4.17(d), the transformed one-dimension vector, similar to (4.12), represents the upper-half of the uv-plane comprising the 180 angles are shown in red for the simulation and in blue for the actual measurement. Furthermore, a separate measurement of a background was made as a control comparison to demonstrate that the measured target had significant higher magnitude of reflected noise illumination than the referenced background. Close resemblance was observed between the simulated (red) and the measured (blue). The second measurement was a Chi-shape forming a 45° acute angle as shown in Fig. 4.18(a) with its simulated visibility in Fig. 4.18(b) showing the orthogonal relationship between the edges' direction and the spatial frequency features' direction. Similarly, the simulated ring-filtered visibility is shown in Fig. 4.18(c) where significant discrete response orthogonal to the physical edges are still expected to be captured. In Fig. 4.18(d), the one-dimensional transformed results of the simulation is shown in red, and the measurement results is shown in blue where close resemblance was observed. Both measured responses are evidently close to the simulated responses which motivate measurements that can be related to an object's spatial domain attributes such as rotation and superposing.

It is reasonable to consider a scenario where target within the sensing system's field-of-view (FOV) can be displaced thus it is worth to validate that the ring filtered Fourier domain features can still be observed upon movement of the object. Common movements include translation or rotation. For the proposed dynamically synthesized ring filter, translation of target does not manifest an angular shift in the spatial frequency domain assuming that the target does not leave the system's FOV. Unlike translational movement, if a target is rotated while remaining in the system's FOV the sharp edges related spatial frequency features must also be rotated by the same quantity as suggested by their orthogonal relationship. Therefore, a third measurement was a vertical stripe as shown in Fig. 4.19(a). Not only does the vertical stripe serve as an additional simple target but it can also be considered as a horizontal stripe (Fig. 4.17(a)) spatially rotated by 90°. The simulated visibility and the ring-filtered visibility are shown in Fig. 4.19(b) and (c), respectively. The one-dimensional responses are shown in Fig. 4.19(d) where the simulation result is in red, and the measurement is in blue validating the assumption of 90° shift of spatial frequency features that are associated to target's rotation. A fourth measurement was a cross target as shown in Fig. 4.20(a) that was intended as a reference measurement for the subsequent spatial rotation measurement. The corresponding simulated visibility and the ring-filtered visibility are shown in Fig. 4.20(b) and (c), respectively. In Fig. 4.20(d), the simulated one-dimensional ring-filtered response is shown in red, and a closely matching measured response is shown in blue. A fifth measurement was the cross target rotated by 45° as shown in Fig. 4.21(a). The associated simulations of visibility and ring-filtered visibility are shown in Fig. 4.21(b) and (c), accordingly. In Fig. 4.21(d), the simulation of the one-dimensional ring-filtered response is shown in red, and the measured response is shown in showing close resemblance and demonstrating the ring filter's capability to identify shapes regardless of a target's spatial rotation. A sixth measurement was a rectangle target as shown in Fig. 4.22(a) with its corresponding simulated visibility and ring filtered visibility in Fig. 4.22(b) and (c). Note that when comparing to the vertical stripe (Fig. 4.19(a)), the rectangle target is shorter in the vertical direction (y) and wider in the horizontal direction (x), which suggest that the visibility should be narrower in the u-direction and wider in the v-direction.

In Fig. 4.22(d), the simulated result is shown in red, and the measurement results is shown in blue showing reasonable resemblance.

The six measurements validate that the discrete and directional dependent spatial frequency features can be captured and identified using the presented two-element rotational dynamic antenna array. Furthermore, two analyses using specific measurements were done to further validate the ring filter concept. First is the fact that the cross target (Fig. 4.20(a)) can also be considered as superposing the horizontal (Fig. 4.17(a)) and vertical (Fig. 4.19(a)) stripes. The one-dimensional ring-filtered responses from both the simulation and measurement are overlapped as shown in Fig. 4.23(a) and (b), respectively. While it is clear that the exact responses are not identical, the strongest spatial frequency features, namely due to the horizontal and vertical components of the cross, are however apparent at the angle 90° and $0/180^\circ$, respectively, which closely resemble that of the horizontal or vertical targets by themselves. Furthermore, the measurements show similar results to the simulation. The second analysis is between the vertical (Fig. 4.19(a)) and the rectangle (Fig. 4.22(a)) targets. The two targets share the same area in terms of the reflective copper foil tape where the vertical target has a dimension of 60.96 cm by 5.08 cm and the rectangle has a dimension of 35.05 cm by 8.89 cm. The simulations and measurements of the one-dimensional ring-filtered responses for the two targets are overlapped a normalized to the vertical target as shown in Fig. 4.23(c) and (d), respectively. By evaluating the two targets together, it is easier to observe the correlation between the spatial shape changes and the associated spatial frequency features. As discussed in Fig. 4.22 that as the size of the vertical edges are shortened, the spatial frequency features along the u-direction also narrows such that the measured responses are comparably weaker for the same 76 λ ring filter.

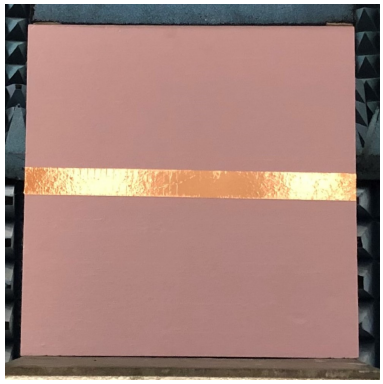

(a)

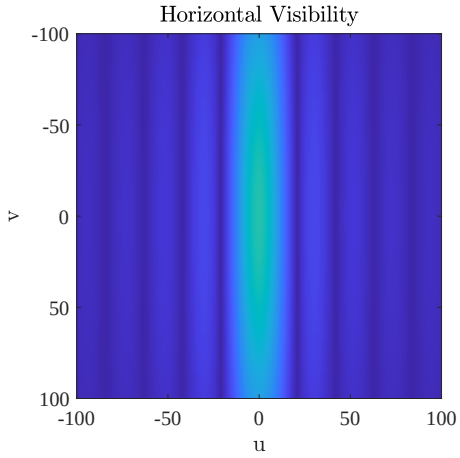

(b)

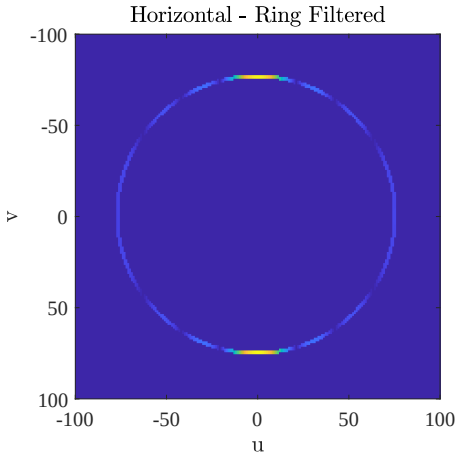

(c)

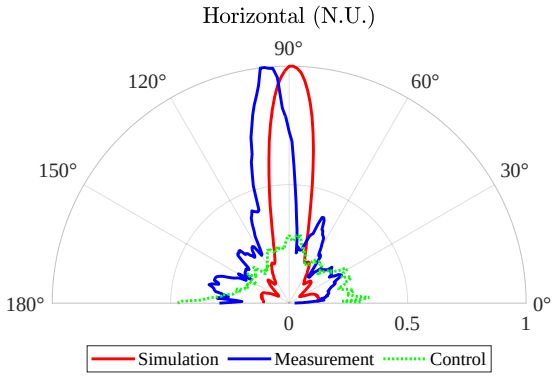

(d)

Figure 4.17: (a) Fabricated target of a horizontal stripe. (b) Simulated visibility of the horizontal stripe. (c) Simulated ring-filtered visibility using a 76λ baseline separation between the two receiving antennas of the dynamic array. (d) Close resemblance between the simulated (red) and measured (blue) linearized ring-filtered responses as a function of the rotational angle for the upper-half of the uv-plane. A background measurement as control is shown in green demonstrating that the measured target had significant higher magnitude of reflected noise illumination than the referenced background. N.U.: Normalized Units. [5].

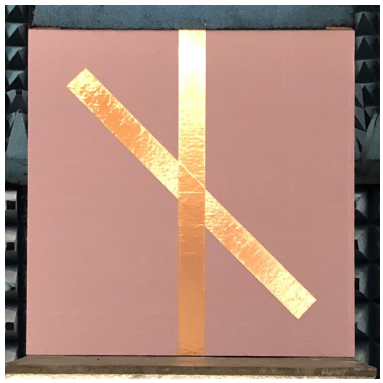

(a)

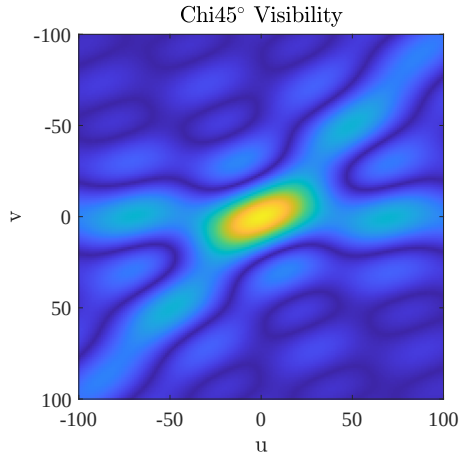

(b)

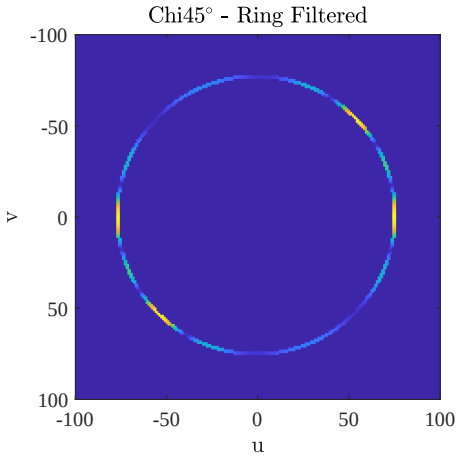

(c)

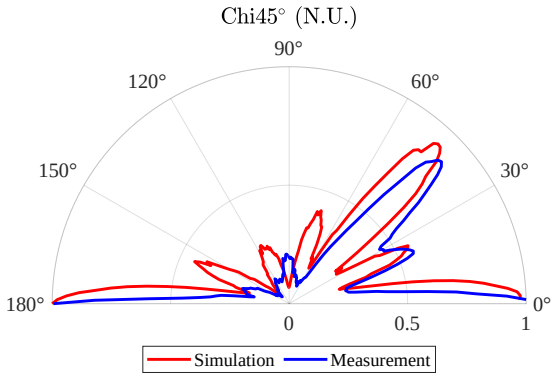

(d)

Figure 4.18: (a) Fabricated target of a Chi-shape with 45° acute angle. (b) Simulated visibility of the Chi-shape with 45° acute angle. (c) Simulated ring-filtered visibility using a 76λ baseline separation between the two receiving antennas of the dynamic array. (d) Close resemblance between the simulated (red) and measured (blue) linearized ring-filtered responses as a function of the rotational angle for the upper-half of the uv-plane. N.U.: Normalized Units. [5].

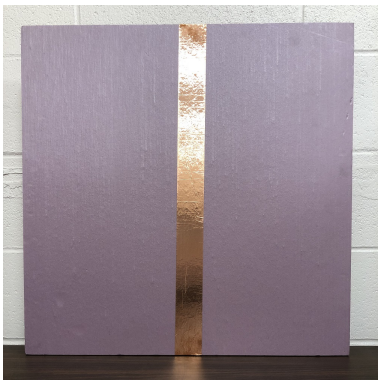

(a)

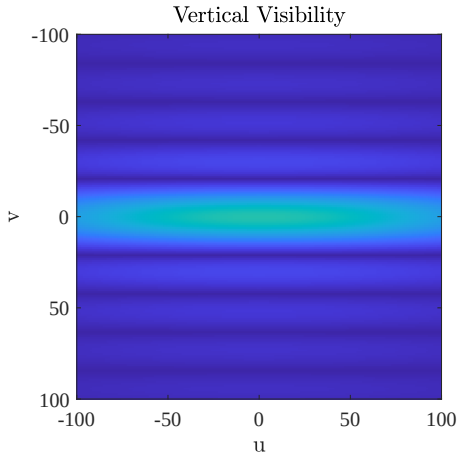

(b)

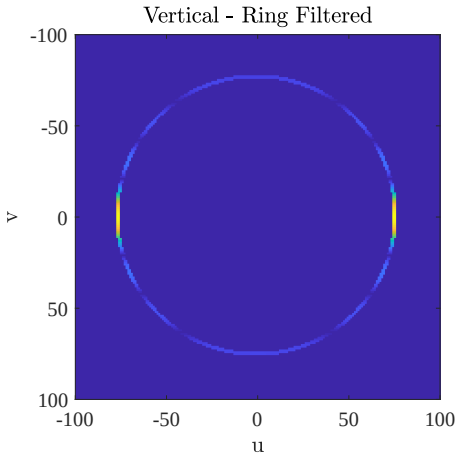

(c)

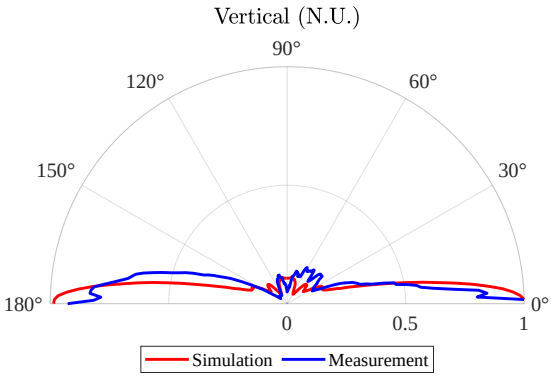

(d)

Figure 4.19: (a) Fabricated target of a vertical stripe. (b) Simulated visibility of the vertical stripe. (c) Simulated ring-filtered visibility using a 76λ baseline separation between the two receiving antennas of the dynamic array. (d) Close resemblance between the simulated (red) and measured (blue) linearized ring-filtered responses as a function of the rotational angle for the upper-half of the uv-plane. N.U.: Normalized Units. [5].

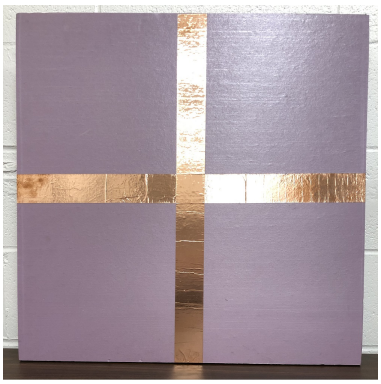

(a)

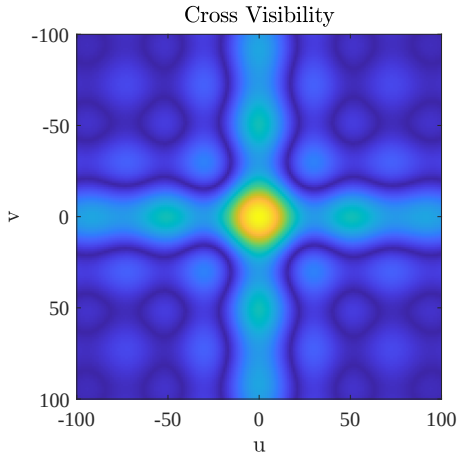

(b)

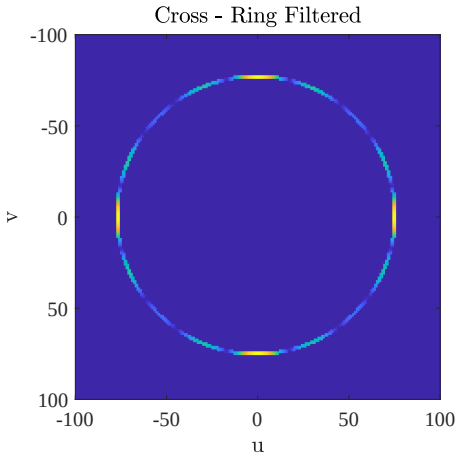

(c)

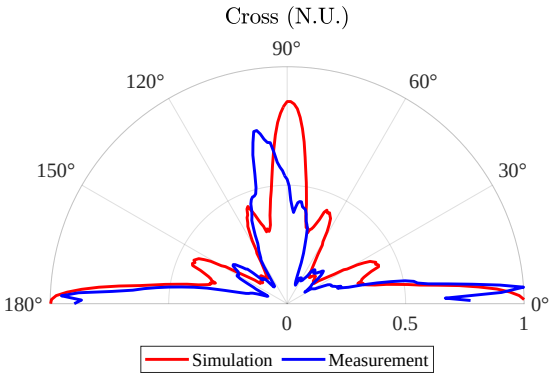

(d)

Figure 4.20: (a) Fabricated target of a cross shape. (b) Simulated visibility of the cross shape. (c) Simulated ring-filtered visibility using a 76λ baseline separation between the two receiving antennas of the dynamic array. (d) Close resemblance between the simulated (red) and measured (blue) linearized ring-filtered responses as a function of the rotational angle for the upper-half of the uv-plane. N.U.: Normalized Units. [5].

(a)

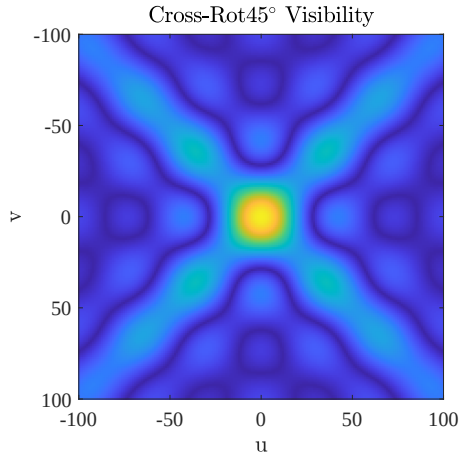

(b)

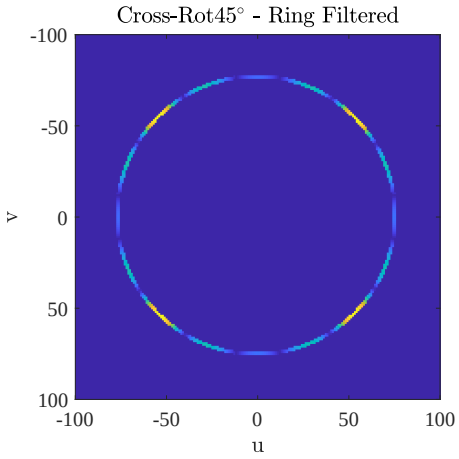

(c)

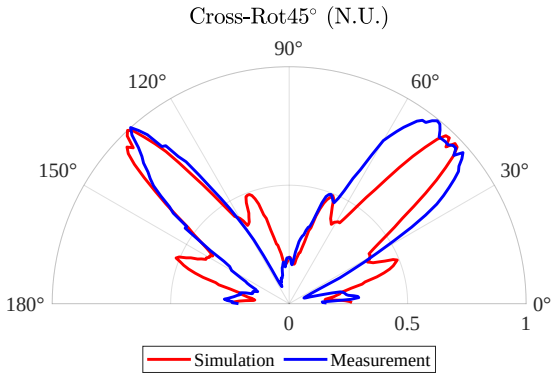

(d)

Figure 4.21: (a) Fabricated target of a cross shape rotated by 45°. (b) Simulated visibility of the cross shape rotated by 45°. (c) Simulated ring-filtered visibility using a 76λ baseline separation between the two receiving antennas of the dynamic array. (d) Close resemblance between the simulated (red) and measured (blue) linearized ring-filtered responses as a function of the rotational angle for the upper-half of the uv-plane. N.U.: Normalized Units. [5].

(a)

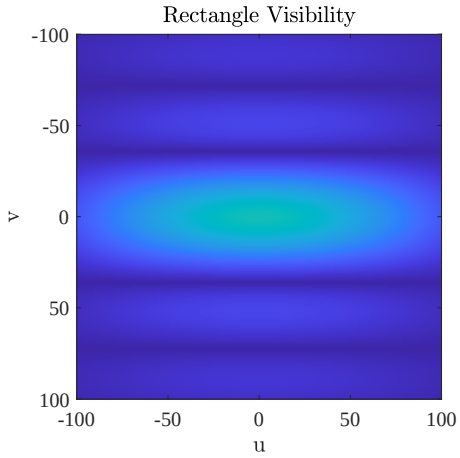

(b)

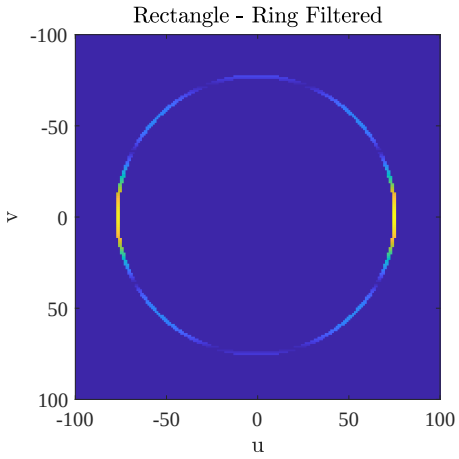

(c)

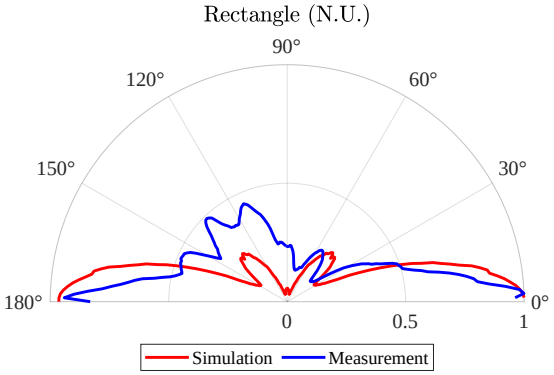

(d)

Figure 4.22: (a) Fabricated target of a rectangle. (b) Simulated visibility of the rectangle. (c) Simulated ring-filtered visibility using a 76λ baseline separation between the two receiving antennas of the dynamic array. (d) Close resemblance between the simulated (red) and measured (blue) linearized ring-filtered responses as a function of the rotational angle for the upper-half of the uv-plane. N.U.: Normalized Units. [5].

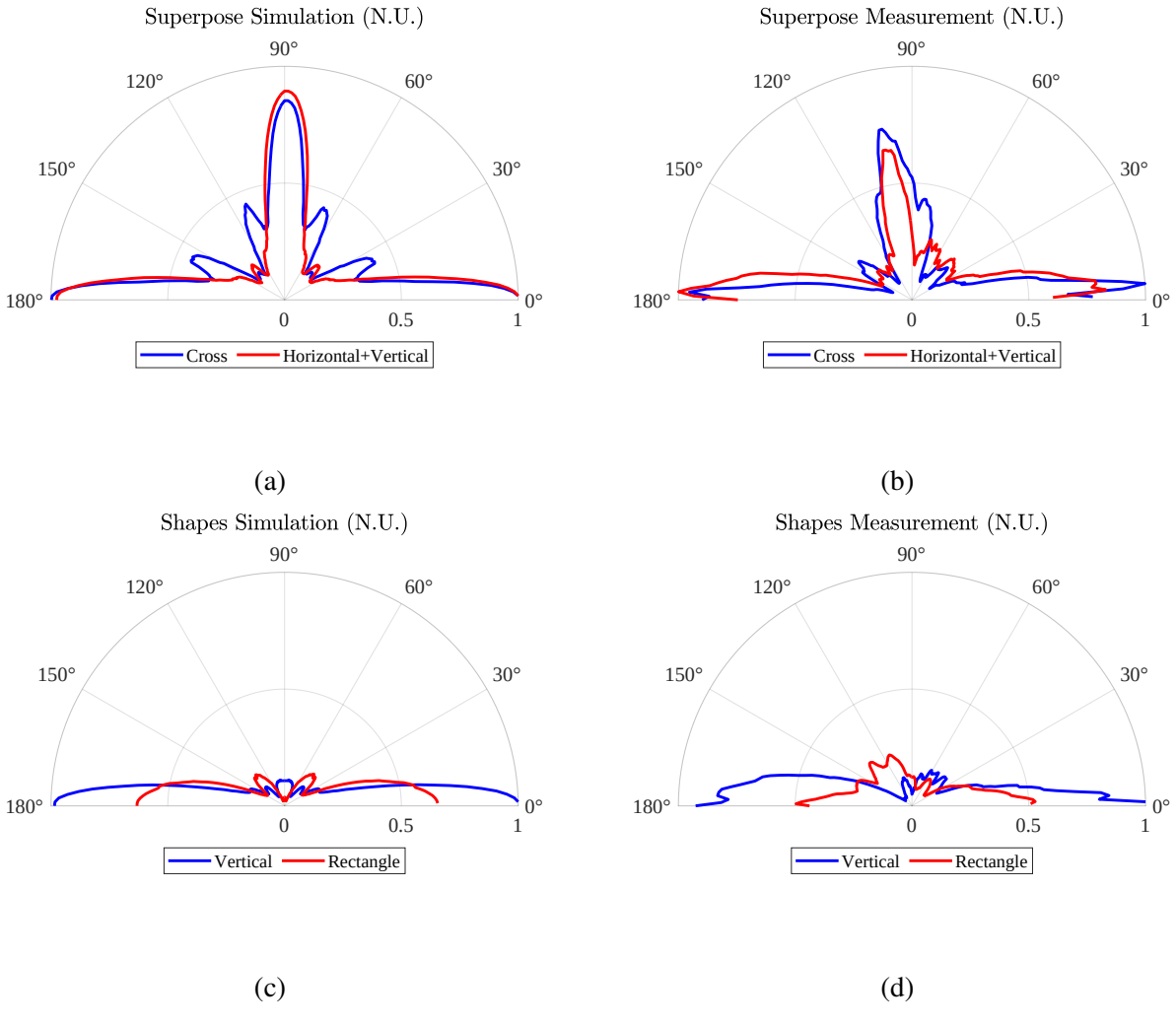

Figure 4.23: (a) Comparison of the simulated results between the cross target in blue and superposing the horizontal and vertical stripes in red. (b) Comparison of the measured results between cross target in blue and superposing the horizontal and vertical stripes in red showing close resemblance to the simulations. (c) Comparison of the simulated results between the vertical stripe in blue and the rectangle in red where all responses are normalized to the vertical stripe to demonstrate that the sharp edge associated Fourier domain signatures changes as the dimension of the physical edge changes when using specific ring filter. (d) Comparison of the measured results between the vertical stripe in blue and the rectangle in red where similar reduction (as in (c)) of the measured signature's magnitude was observed. N.U.: Normalized Units. [5].

4.2.2 Concealed Contraband Identification

While the previously described simple shape measurements help to validate the identification of spatial frequency samples without relying on full image reconstruction, additional measurements were conducted to mimic the possible use case in the area of short range sensing application for concealed contraband detection. For the experiment, a common mannequin torso clothed with a shirt where a fabricated knife prop was concealed underneath the shirt was measured and a separate measurement of only the clothed mannequin torso as control comparison was conducted. The setups for these measurements are shown in Fig. 4.24, where the top is a side view of a measurement in progress, bottom left is the clothed mannequin torso with the fabricated knife prop as concealed contraband, and the bottom right is the unclothed mannequin torso showing the exact position and orientation of the fabricated knife prop. The fabricated knife prop has physical length of 45 cm from base to tip, width of 3.81 cm, and tip that has a measured angle of 27°. Similar to the simple shape measurements, the two-element rotational dynamic antenna array was set at a baseline of 76λ and 180 angles in 1° increment that maps out the upper-half of the uv-plane. The measurement results are shown in Fig. 4.25 where the control scene, absent of the fabricated knife, is in dotted-black and the observation of evident responses for the contraband present scenario in red. The blue line indicates the location of the response due to the knife's edge, which manifests orthogonality to the largest physical edge that is clearly apparent in both simulation and measurement matching the expected locations of response which are absent in the control measurement. Furthermore, the angular positions between the two strongest responses form an angle of approximately 29° that closely resemble the fabricated knife prop's tip angle of 27°. Thus, the similarity between the angles of actual sharp edges of the knife prop and the ring-filtered spatial frequency responses further validates the imageless approach enabled by the rotational dynamic antenna array concept.

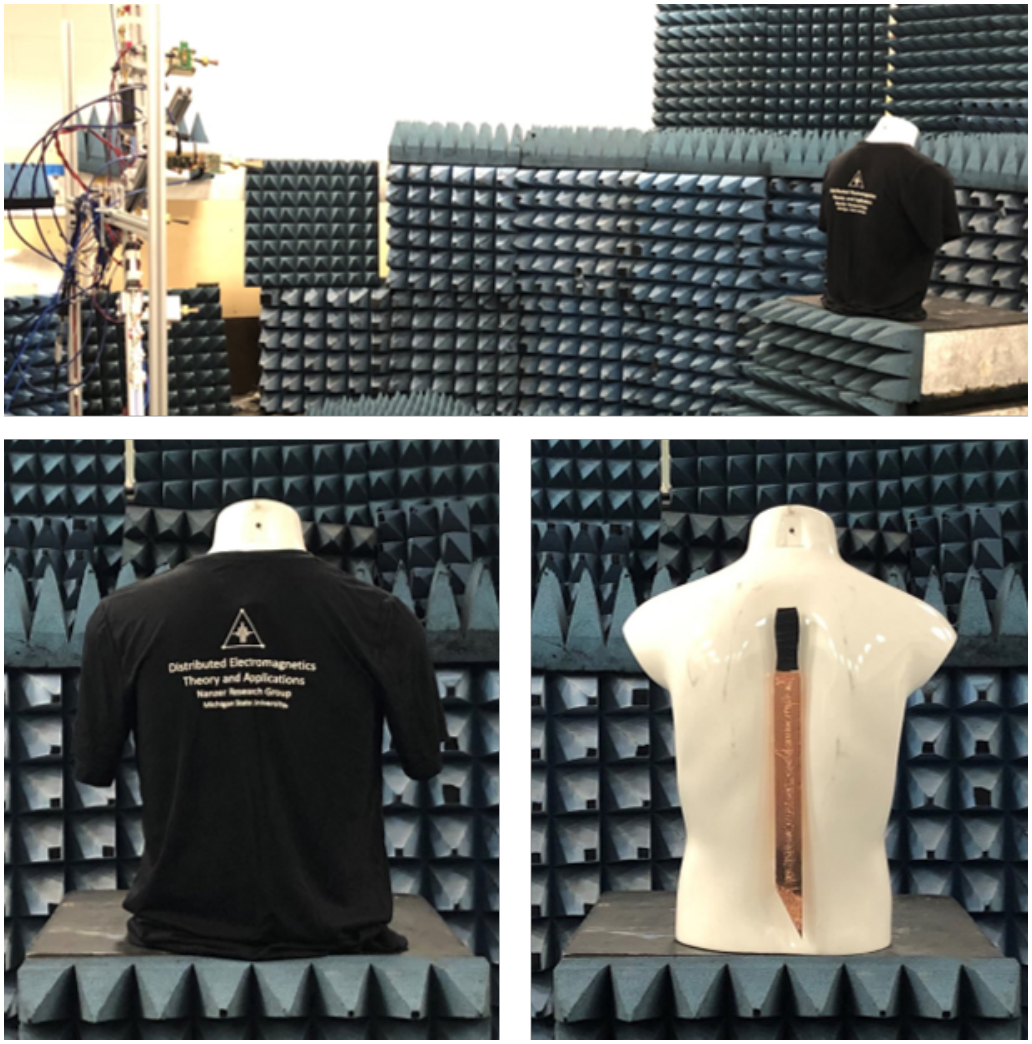

Figure 4.24: Top: Measurement setup. Bottom Left: Clothed mannequin torso with knife prop as concealed contraband. Bottom Right: Unclothed mannequin torso showing the position and orientation of the knife prop. [6].

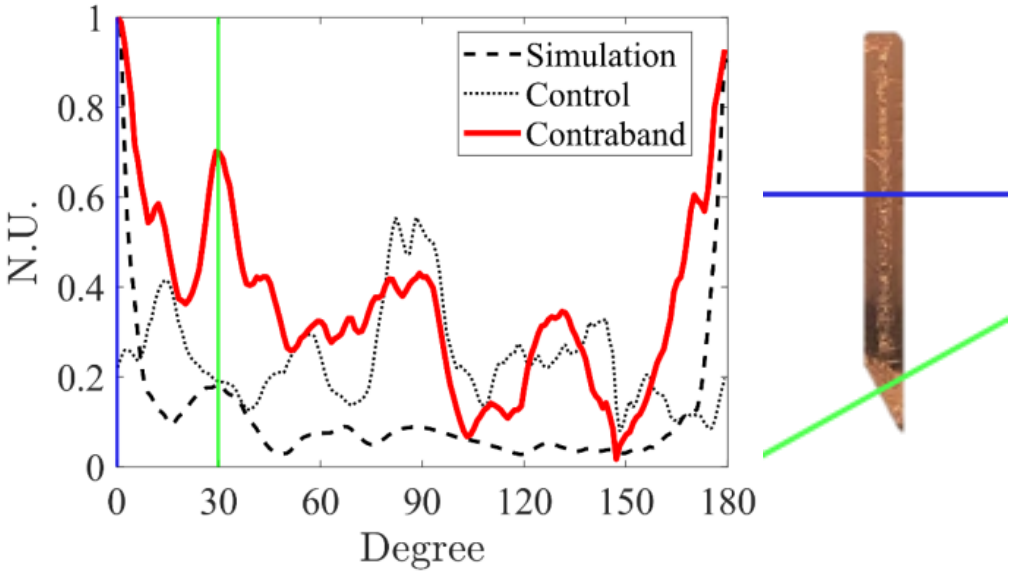

Figure 4.25: Experimental results of the spatial frequency samples collected by the rotating dynamic antenna array over a 180° angular span in 1° increments. The strongest responses manifest orthogonally to the largest edge of the object (blue line). The smaller angled knife edge is also visible (green line). N.U.: Normalized Units. [6].

CHAPTER 5

CONCLUSION

An active incoherent millimeter-wave (AIM) based sensing system using a rotational dynamic antenna array was presented. The dynamic array sensing system operates at 38 GHz (millimeter-wave) comprises three transmitting channels as noise illuminating sources (active incoherent), two receiving channels with adjustable baseline separation, and a dynamically rotatable structure such that the two receiving antennas can co-rotate to generate ring-like spatial frequency sampling points while maintaining co-polarization with the noise illuminating transmitters. The implemented system collects spatial frequency samples that are dependent on the two receiving antennas physical separation, operating frequency, and the signal bandwidth. The received signals at the two-receiving antennas are subsequently downconverted to baseband signals that were stored and processed offline where the complex cross-correlation were used to generate the measured spatial frequency samples. Upon generating the measured spatial frequency samples, an inverse Fourier transform operation can be leveraged for image reconstruction of the sensed scene when sufficient amount of samples are collected; or, an imageless detection approach can be conducted where the measured spatial frequency are mapped to the particular measured angle over a finer ring of spatial frequency samples such that the discrete and directional oriented strong Fourier domain responses related to spatial sharp edges can be identified.

The system was used to image two scenes containing metallic spherical targets to demonstrate the capability of the dynamic-antenna-array-based AIM sensing technique where conclusive observations were made from the close resemblance between the spherical targets' location in the reconstructed and simulated imagery which were generated based on the physical locations of the targets. An imageless spatial frequency domain classification approach using a ring-shaped spatial frequency sampling function (ring filter) was also presented as a simulation-based study where large number of radar ground imagery of natural and non-natural (man-made structures/objects) scenes were successfully distinguished using both an analytical threshold-based decision bound-

ary and the K-nearest neighbor classifier. Furthermore, the implemented two-element rotational dynamic antenna array setup was used to experimentally synthesized the ring filter to measure various simple scenes that validated the presented orthogonal relationships between spatial sharp edges and the discrete but broadband spatial frequency responses; additional spatial attributes such as rotational displacement and superposing of the simple targets were also measured and evaluated. Lastly, the rotational dynamic antenna array setup was used to evaluate the use case of short-range security sensing for concealed contraband detection. Conclusive results indicating that a real-life sized knife prop, as the concealed contraband under clothing, was identified from the imageless ring filter approach using the setup.

APPENDICES

APPENDIX A

DYNAMIC ANTENNA ARRAY PARTS, SCHEMATICS, PHOTOS

A.1 Parts

Manufacturer (Part Number)	**Schematic Label(s)**
MEAN WELL USA Inc. (RS-15-24)	P24V
XP Power (VCS100US05)	P6V
MEAN WELL USA Inc. (RS-25-5)	P5V
MEAN WELL USA Inc. (RSP-320-3.3)	P3V1, P3V2
Mini-Circuits (ZN4PD1-183W-S+)	1:4 Splitter
MIDISCO (MDC2288)	1:2 Splitter
Mini-Circuits (ULC-6FT-SMSM+)	CALO0, CAI**x**, CAQ**x**
Mini-Circuits (FLC-6FT-SMSM+)	CALO1, CALO**x** (CALO2, CALO3, CALO4, CALO5)
RF-GADGETS (XDM NSE15-1)	NS**x**
Mini-Circuits (ZX60-V63+)	A**x**1, A**x**2, A**x**3, A**x**4
Linx Technologies Inc. (ADP-SMAM-SMAM)	ADP1, ADP**x**1, ADP**x**2, ADP**x**3, ADP**x**4
Mini-Circuits (086-24SM+)	CA**x**1
Amphenol RF (132360)	T50**x**
Analog Devices (HMC6787ALC5A)	UC**x**
Mini-Circuits (KM-KM50+)	ADP**x**5, ADP**x**6
Analog Devices (HMC7229LS6)	PA**x**
Sage Millimeter (SWC-28KM-E1)	WG**x**
L3Harris Narda-ATM (28-440-6)	TX**x**
L3Harris Narda-ATM (28-441-6)	RX**x**
Analog Devices (HMC1040LP3CE)	LNA**x**
Analog Devices (HMC6789BLC5A)	DC**x**

Table A.1: Manufacturer part number and the associated labels in the subsequent schematics. Bold '**x**'s indicate common parts in multiple channels. Standard insulated (i.e., stranded/solid) electrical wires for power supply related connections are not listed.

A.2 Schematic of Power Supply Subsystem

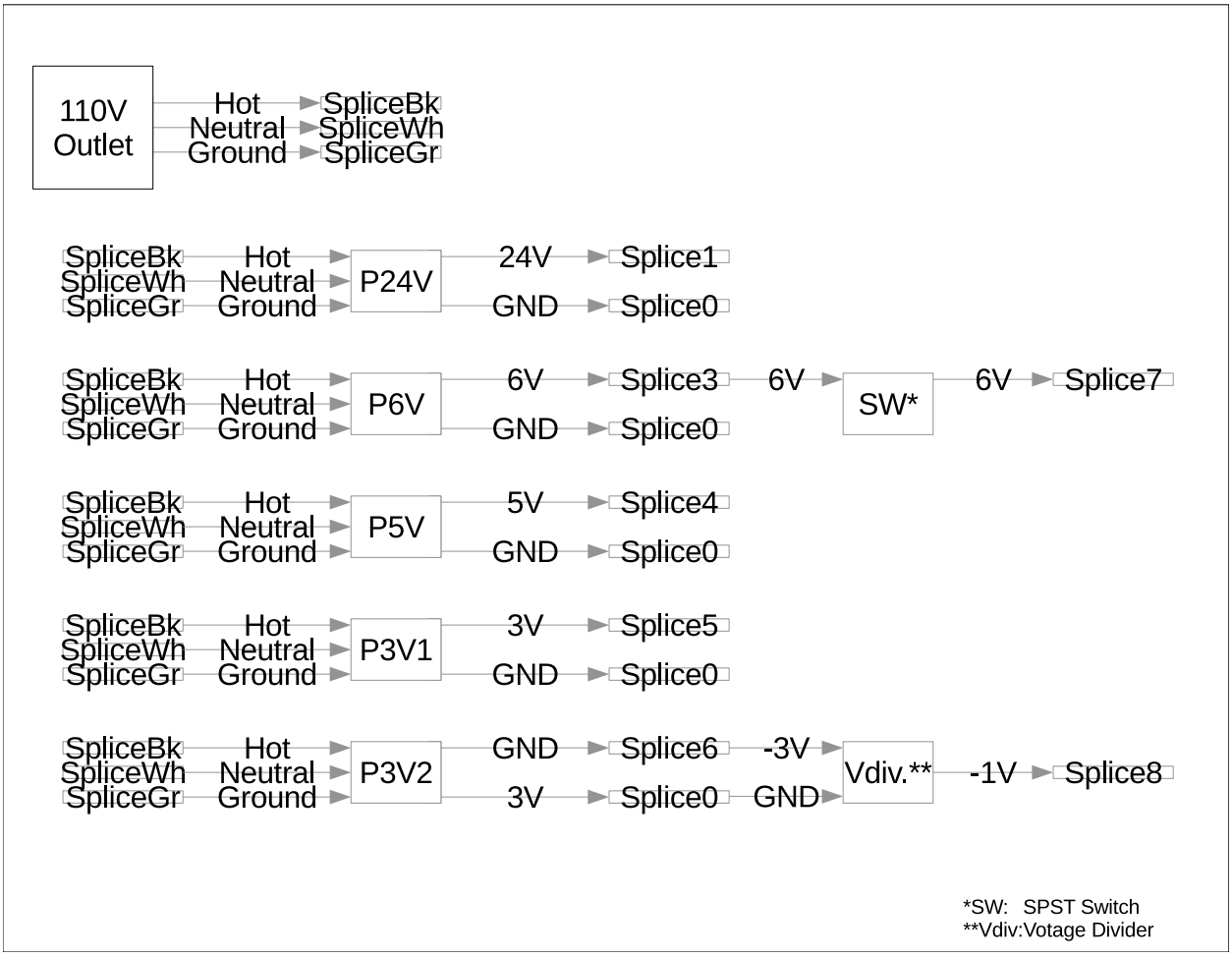

Figure A.1: Schematic of power supply subsystem for the dynamic antenna array.

A.3 Schematic of Transmitting Subsystem

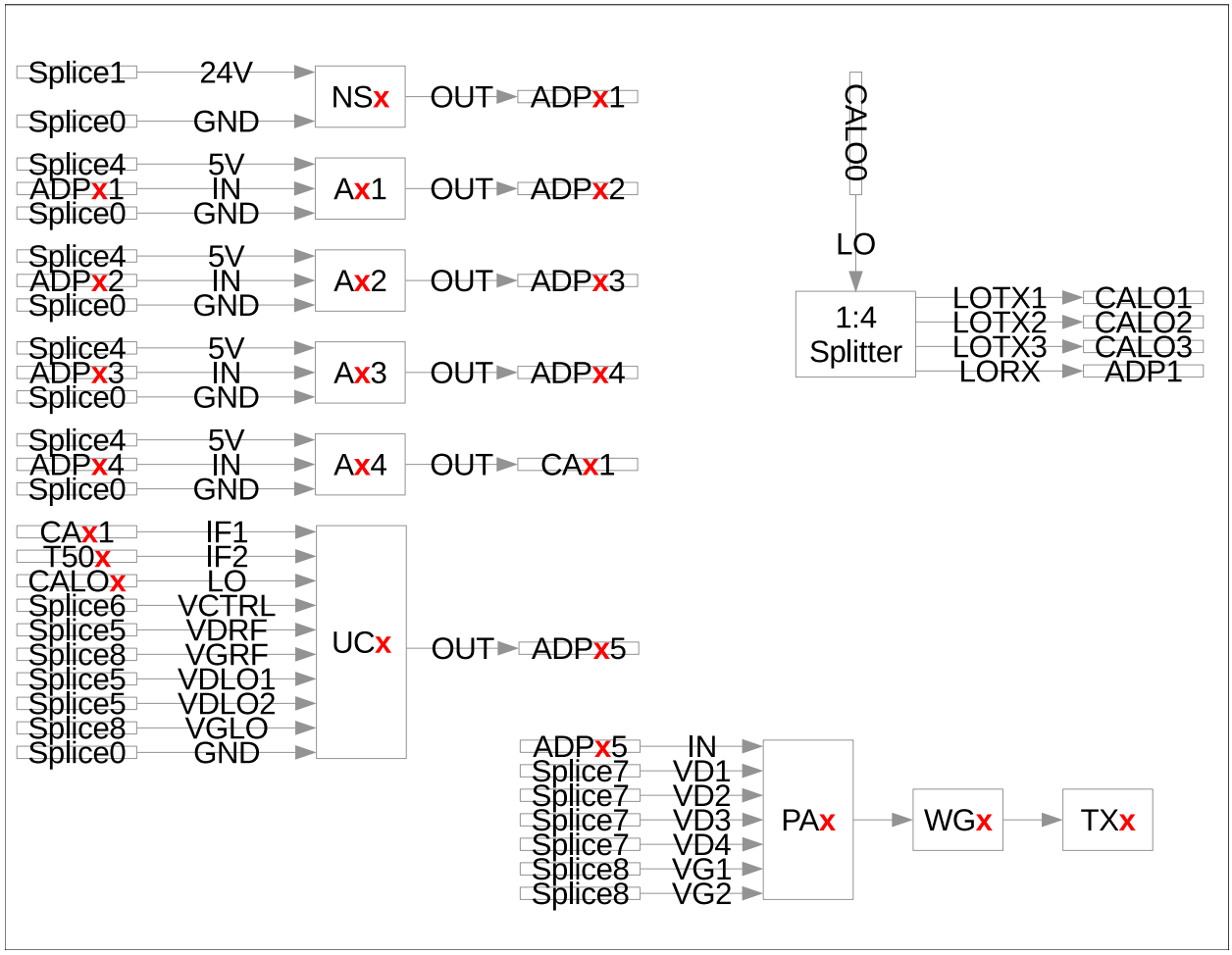

Figure A.2: Schematic of transmitting subsystem for the dynamic antenna array. The red '**x**'s indicate the three transmitting channels (i.e., 1, 2, and 3).

A.4 Schematic of Receiving Subsystem

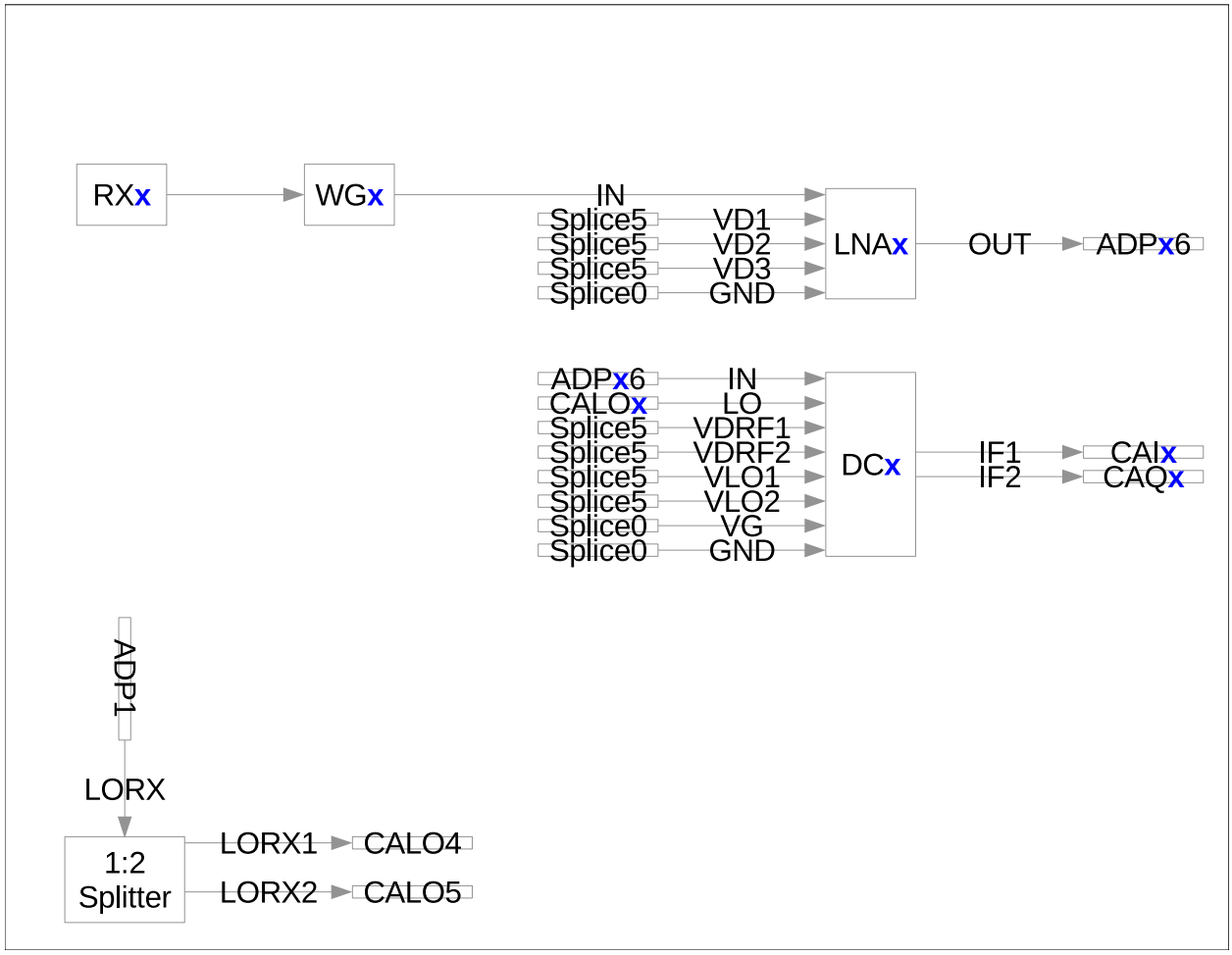

Figure A.3: Schematic of receiving subsystem for the dynamic antenna array. The blue '**x**'s indicate the two receiving channels (i.e., 1 and 2).

A.5 Earlier Implementation of Dynamic Antenna Array

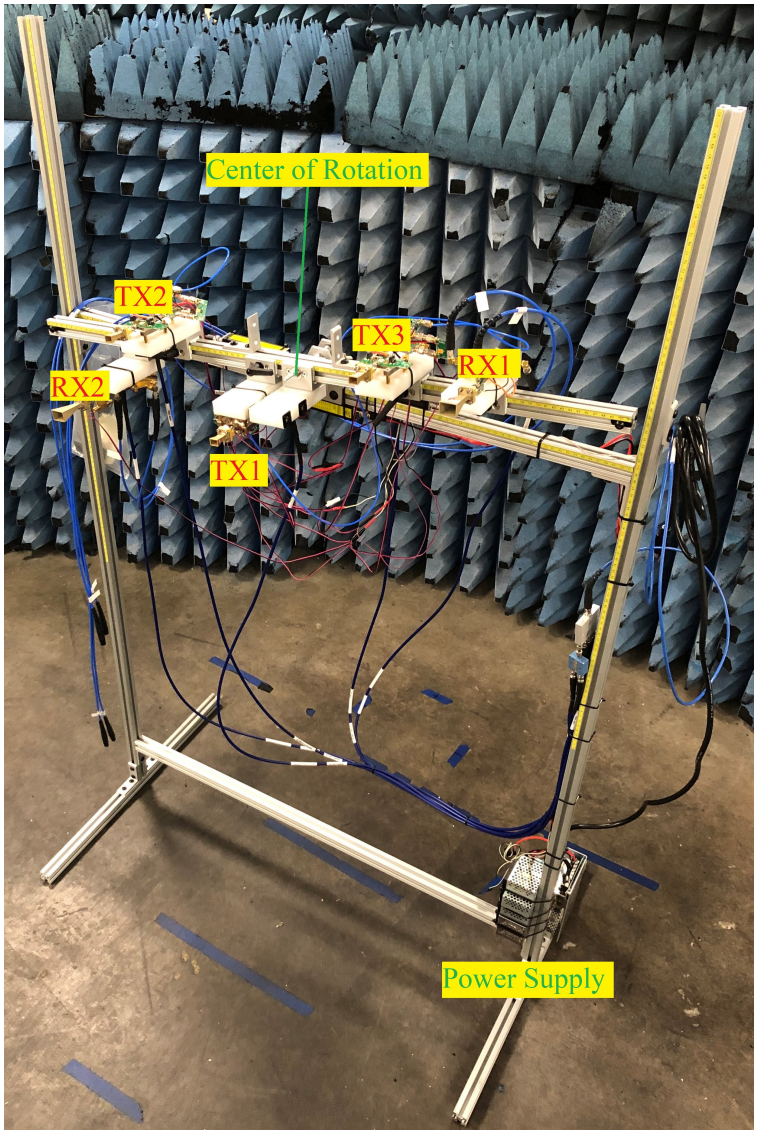

Figure A.4: First iteration of the implemented dynamic antenna array. Two receivers' adjustable baseline range was [60.0 cm, 83.6 cm], or [76λ, 106λ] based on 38 GHz.

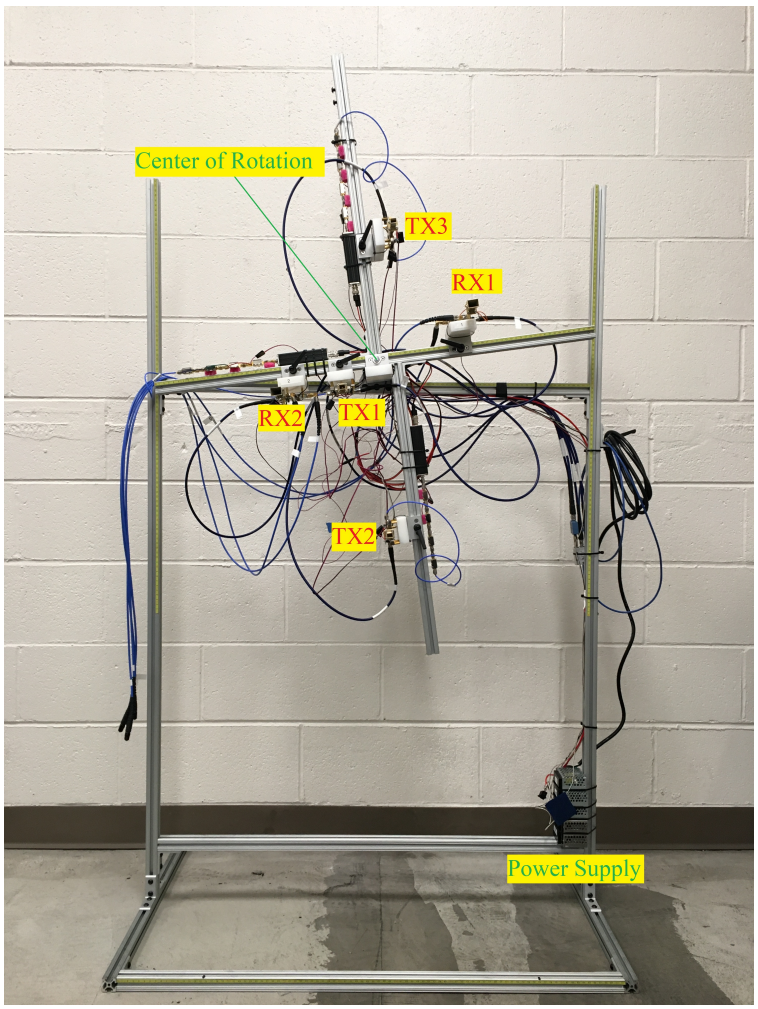

Figure A.5: Second iteration of the implemented dynamic antenna array. Two receivers' adjustable baseline range was [63.4 cm, 83.6 cm], or [50λ, 106λ] based on 38 GHz.

APPENDIX B

CODES

B.1 Processing Oscilloscope Data

```
%================================================================%
% Importing the data from the Agilent MSO-X 92004A Oscilloscope.
% Data are in .csv format with five columns:
% Column 1: time, or duration of the recorded signals.
% Column 2: in-phase signal of receiver 1.
% Column 3: quarature signal of receiver 1.
% Column 4: in-phase signal of receiver 2.
% Column 5: quarature signal of receiver 2.
% File naming convention: XX-OOO, where
% 'XX' is the baseline in wavelength, and
% 'OOO' is the angle (degree) formed with the horizontal plane.
%----------------------------------------------------------------%
% Low Pass Filter
fs = 2.5e9; % GSample/s
fcut = 12e8; % Hz
[b,a] = butter(5,fcut/(fs/2),'low');
freqz(b,a)
%----------------------------------------------------------------%
% Path to the directory of the .csv files
path = 'SPECIFIC_TO_WORKSTATION';
% Read in files that has .csv extension in the directory
cd(path);
```

```
path = strcat(path,"\*.csv");
csv_file = dir(path);
%-------------------------------------------------------------%
% Assign each data column to the corresponding in-phase and
% quadrature channel and perform complex cross-correlation
% for each measured angle.
my_data(length(csv_file)) = struct();
for n = 1:length(csv_file)
temp_all_data = filter(b,a,importdata(csv_file(n).name));

% Map oscilloscpe data to each receivers' I, Q channels.
% Remove the offset and scaling setting on the oscilloscope.
% Normalize all data and assigned to corresponding RX.
rx1 = (temp_all_data(:,2) - nanmean(temp_all_data(:,2)))...
    /max(temp_all_data(:,2) - nanmean(temp_all_data(:,2))) +...
    1i*((temp_all_data(:,3) - nanmean(temp_all_data(:,3)))...
    /max(temp_all_data(:,3) - nanmean(temp_all_data(:,3))));
rx2 = (temp_all_data(:,4) - nanmean(temp_all_data(:,4)))...
    /max(temp_all_data(:,4) - nanmean(temp_all_data(:,4))) +...
    1i*((temp_all_data(:,5) - nanmean(temp_all_data(:,5)))...
    /max(temp_all_data(:,5) - nanmean(temp_all_data(:,5))));

% Baseline Information
string = split(csv_file(n).name,"-");
my_data(n).baseline = str2double(string(1));
% Angle Information
string = split(string(2),".");
```

```
my_data(n).angle = str2double(string(1));
% Receiver Response
my_data(n).response = rx1.*conj(rx2);
end
%=========================================================%
```

B.2 Image Reconstruction and CLEAN

```
%=========================================================%
% Image Reconstrsuction using the processed oscilloscope data
%---------------------------------------------------------%
% Recontruction
largest_D = 106; % Largest baseline
total_scene = zeros(2*largest_D+1);

% Construct the Sample Visibility in uv-space
sample_vis = total_scene;
for n = 1:length(my_data)
    sample_vis = samp_vis_construction(my_data(n).baseline,...
        my_data(n).angle, my_data(n).response, sample_vis);
end

%Pad Factor 1 and 2D inverse Fourier transform
pad = 2;
recon = ifftshift(...
    ifft2(...
    sample_vis,pad*length(sample_vis),pad*length(sample_vis)));
%---------------------------------------------------------%
```

```
% Recontruction with Further Deconvolution
recon = CLEAN(recon, PSF, 15, 1);
%-----------------------------------------------------------------%
% Constructing Sampled Visibility
function updated_samp_vis = samp_vis_construction(baseline,...
    angle, response, current_samp_vis)
[x,y] = pol2cart(angle*pi()/180, baseline);
[x1,y1] = pol2cart((angle+180)*pi()/180, baseline);
current_samp_vis(round(length(current_samp_vis)/2+y),...
    round(length(current_samp_vis)/2+x)) = sum(response);
current_samp_vis(round(length(current_samp_vis)/2+y1),...
    round(length(current_samp_vis)/2+x1)) = sum(conj(response));
updated_samp_vis = current_samp_vis;
end
% CLEAN
function cleaned_image =...
    CLEAN(dirty_img, dirty_beam, iteration, masking)
if masking == 0
mask = ones(size(dirty_img));
end
if masking == 1
x = linspace(-1,1,length(dirty_img));
y = linspace(1,-1,length(dirty_img))';

x = repmat( x , [ length(dirty_img) , 1 ] );
y = repmat( y , [ 1 , length(dirty_img) ] );
```

```
index = sqrt(x.^2+y.^2);
mask = index;
mask(index<=.40) = 1;
mask(index>.40) = 0;
end
loop_gain = 1;
model = zeros(size(dirty_img));
wip_dirty_img = mask.*dirty_img;

for i = 1:iteration
index = wip_dirty_img==max(wip_dirty_img,[],'all');
model(index) = dirty_img(index);
wip_dirty_img =...
    mask.*(dirty_img-loop_gain.*conv2(model,dirty_beam,'same'));
end
cleaned_image = model;
end
%=================================================================%
```

BIBLIOGRAPHY

BIBLIOGRAPHY

[1] D. Chen, S. Vakalis, and J. A. Nanzer. Dynamic antenna array design for scene classification through fourier-domain filtering. *IEEE Transactions on Antennas and Propagation*, pages 1–1, 2021.

[2] D. Chen, S. Vakalis, and J. A. Nanzer. Millimeter-wave imaging using a dynamic antenna array and noise illumination. *IEEE Transactions on Antennas and Propagation*, submitted on 2021.06.22.

[3] J. A. Hogbom. Aperture Synthesis with a Non-Regular Distribution of Interferometer Baselines. *Astron. Astrophys. Suppl. Ser.*, 15:417–426, 1974.

[4] https://www.iceye.com/downloads/datasets, 2019 (accessed March 17, 2020).

[5] D. Chen, S. Vakalis, and J. A. Nanzer. Imageless shape detection using a millimeter-wave dynamic antenna array and noise illumination. *IEEE Transactions on Microwave Theory and Techniques*, submitted on 2021.07.16.

[6] D. Chen and J. A. Nanzer. A dynamic antenna array for imageless contraband detection. In *2021 IEEE International Symposium on Antennas and Propagation and USNC-URSI Radio Science Meeting*, to be published.

[7] L. Satyanarayan, Ajith Muralidharan, Chittivenkata Krishnamurthy, and Krishnan Balasubramaniam. Application of a matched filter approach for finite aperture transducers for the synthetic aperture imaging of defects. *IEEE Transactions on Ultrasonics, Ferroelectrics, and Frequency Control*, 57(6):1368–1382, 2010.

[8] Smriti Agarwal and Dharmendra Singh. An adaptive statistical approach for non-destructive underline crack detection of ceramic tiles using millimeter wave imaging radar for industrial application. *IEEE Sensors Journal*, 15(12):7036–7044, 2015.

[9] Nasim Moallemi and Shahram Shahbazpanahi. A novel spatio-temporal frequency-domain imaging technique for two-layer materials using ultrasonic arrays. *IEEE Access*, 6:8977–8989, 2018.

[10] B.F. Jones. A reappraisal of the use of infrared thermal image analysis in medicine. *IEEE Transactions on Medical Imaging*, 17(6):1019–1027, 1998.

[11] E. C. Fear, X. Li, S. C. Hagness, and M. A. Stuchly. Confocal microwave imaging for breast cancer detection: localization of tumors in three dimensions. *IEEE Transactions on Biomedical Engineering*, 49(8):812–822, 2002.

[12] A. Godavarty, S. Erickson, J. Gonzalez, U. Chaudhary, M. Hall, M. Roman, and R. Roche. Non-invasive optical imaging technology: Breast cancer imaging and functional brain mapping. In *2012 Pan American Health Care Exchanges*, pages 125–125, 2012.

[13] L. M. Neira, B. D. Van Veen, and S. C. Hagness. High-resolution microwave breast imaging using a 3-d inverse scattering algorithm with a variable-strength spatial prior constraint. *IEEE Transactions on Antennas and Propagation*, 65(11):6002–6014, 2017.

[14] P. M. Meaney, M. W. Fanning, Dun Li, S. P. Poplack, and K. D. Paulsen. A clinical prototype for active microwave imaging of the breast. *IEEE Transactions on Microwave Theory and Techniques*, 48(11):1841–1853, Nov 2000.

[15] Andreas S. Panayides, Amir Amini, Nenad D. Filipovic, Ashish Sharma, Sotirios A. Tsaftaris, Alistair Young, David Foran, Nhan Do, Spyretta Golemati, Tahsin Kurc, Kun Huang, Konstantina S. Nikita, Ben P. Veasey, Michalis Zervakis, Joel H. Saltz, and Constantinos S. Pattichis. Ai in medical imaging informatics: Current challenges and future directions. *IEEE Journal of Biomedical and Health Informatics*, 24(7):1837–1857, 2020.

[16] J. P. P. Gomes, J. F. B. Brancalion, and D. Fernandes. Automatic target recognition in synthetic aperture radar image using multiresolution analysis and classifiers combination. In *2008 IEEE Radar Conference*, pages 1–5, 2008.

[17] U. Srinivas, V. Monga, and R. G. Raj. Sar automatic target recognition using discriminative graphical models. *IEEE Transactions on Aerospace and Electronic Systems*, 50(1):591–606, 2014.

[18] Shuanghui Zhang, Yongxiang Liu, and Xiang Li. Bayesian bistatic isar imaging for targets with complex motion under low snr condition. *IEEE Transactions on Image Processing*, 27(5):2447–2460, 2018.

[19] Joakim Lindblad and Nataša Sladoje. Linear time distances between fuzzy sets with applications to pattern matching and classification. *IEEE Transactions on Image Processing*, 23(1):126–136, 2014.

[20] Dengxin Dai and Wen Yang. Satellite image classification via two-layer sparse coding with biased image representation. *IEEE Geoscience and Remote Sensing Letters*, 8(1):173–176, 2011.

[21] Sanping Zhou, Jinjun Wang, Le Wang, Jimuyang Zhang, Fei Wang, Dong Huang, and Nanning Zheng. Hierarchical and interactive refinement network for edge-preserving salient object detection. *IEEE Transactions on Image Processing*, 30:1–14, 2021.

[22] Yake Zhang, Fang Liu, Licheng Jiao, Shuyuan Yang, Lingling Li, and Meijuan Yang. Discriminative sketch topic model with structural constraint for sar image classification. *IEEE Journal of Selected Topics in Applied Earth Observations and Remote Sensing*, 13:5730–5745, 2020.

[23] Biao Hou, Chao Chen, Xiaojuan Liu, and Licheng Jiao. Multilevel distribution coding model-based dictionary learning for polsar image classification. *IEEE Journal of Selected Topics in Applied Earth Observations and Remote Sensing*, 8(11):5262–5280, 2015.

[24] Tsung-Han Chan, Kui Jia, Shenghua Gao, Jiwen Lu, Zinan Zeng, and Yi Ma. Pcanet: A simple deep learning baseline for image classification? *IEEE Transactions on Image Processing*, 24(12):5017–5032, 2015.

[25] Hui Li and Xiao-Jun Wu. Densefuse: A fusion approach to infrared and visible images. *IEEE Transactions on Image Processing*, 28(5):2614–2623, 2019.

[26] Jie Wang, Yalan Zheng, Min Wang, Qian Shen, and Jiru Huang. Object-scale adaptive convolutional neural networks for high-spatial resolution remote sensing image classification. *IEEE Journal of Selected Topics in Applied Earth Observations and Remote Sensing*, 14:283–299, 2021.

[27] Jianpeng Zhang, Yong Xia, Yutong Xie, Michael Fulham, and David Dagan Feng. Classification of medical images in the biomedical literature by jointly using deep and handcrafted visual features. *IEEE Journal of Biomedical and Health Informatics*, 22(5):1521–1530, 2018.

[28] K.L. Boyer, A. Herzog, and C. Roberts. Automatic recovery of the optic nervehead geometry in optical coherence tomography. *IEEE Transactions on Medical Imaging*, 25(5):553–570, 2006.

[29] Shay Keren, Olivier Gheysens, Craig S. Levin, and Sanjiv S. Gambhir. A comparison between a time domain and continuous wave small animal optical imaging system. *IEEE Transactions on Medical Imaging*, 27(1):58–63, 2008.

[30] Qianqian Fang, Stefan A. Carp, Juliette Selb, Greg Boverman, Quan Zhang, Daniel B. Kopans, Richard H. Moore, Eric L. Miller, Dana H. Brooks, and David A. Boas. Combined optical imaging and mammography of the healthy breast: Optical contrast derived from breast structure and compression. *IEEE Transactions on Medical Imaging*, 28(1):30–42, 2009.

[31] Ching-Cheng Chuang, Chia-Yen Lee, Chung-Ming Chen, Yao-Sheng Hsieh, Tsan-Chi Liu, and Chia-Wei Sun. Diffuser-aided diffuse optical imaging for breast tumor: A feasibility study based on time-resolved three-dimensional monte carlo modeling. *IEEE Transactions on Biomedical Engineering*, 59(5):1454–1461, 2012.

[32] R. Highnam and M. Brady. Model-based image enhancement of far infrared images. *IEEE Transactions on Pattern Analysis and Machine Intelligence*, 19(4):410–415, 1997.

[33] T.D. Tosteson, B.W. Pogue, E. Demidenko, T.O. McBride, and K.D. Paulsen. Confidence maps and confidence intervals for near infrared images in breast cancer. *IEEE Transactions on Medical Imaging*, 18(12):1188–1193, 1999.

[34] A. Dawoud, M.S. Alam, A. Bal, and C. Loo. Target tracking in infrared imagery using weighted composite reference function-based decision fusion. *IEEE Transactions on Image Processing*, 15(2):404–410, 2006.

[35] Valentina Agostini, Silvia Delsanto, Marco Knaflitz, and Filippo Molinari. Noise estimation in infrared image sequences: A tool for the quantitative evaluation of the effectiveness of registration algorithms. *IEEE Transactions on Biomedical Engineering*, 55(7):1917–1920, 2008.

[36] K. Hossain, C. Mantel, and S. Forchhammer. Evaluation of prediction of quality metrics for ir images for uav applications. In *2019 Data Compression Conference (DCC)*, pages 578–578, 2019.

[37] J. A. Nanzer. *Microwave and Millimeter-Wave Remote Sensing for Security Applications*. Artech House, 2012.

[38] N.C. Currie and C.E. Brown. *Principles and Applications of Millimeter-Wave Radar*. Artech House, 1987.

[39] D. M. Sheen, D. L. McMakin, and T. E. Hall. Three-dimensional millimeter-wave imaging for concealed weapon detection. *IEEE Transactions on Microwave Theory and Techniques*, 49(9):1581–1592, 2001.

[40] L. C. Graham. Synthetic interferometer radar for topographic mapping. *Proceedings of the IEEE*, 62(6):763–768, 1974.

[41] D. Moller, S. Hensley, G. A. Sadowy, C. D. Fisher, T. Michel, M. Zawadzki, and E. Rignot. The glacier and land ice surface topography interferometer: An airborne proof-of-concept demonstration of high-precision ka-band single-pass elevation mapping. *IEEE Transactions on Geoscience and Remote Sensing*, 49(2):827–842, 2011.

[42] R. Seu, S. Smrekar, S. Hensley, and P. Lombardo. A sar interferometer experiment to explore the surface of venus. In *Proceedings of EUSAR 2016: 11th European Conference on Synthetic Aperture Radar*, pages 1–3, 2016.

[43] T. Sleasman, M. Boyarsky, L. Pulido-Mancera, T. Fromenteze, M. F. Imani, M. S. Reynolds, and D. R. Smith. Experimental synthetic aperture radar with dynamic metasurfaces. *IEEE Transactions on Antennas and Propagation*, 65(12):6864–6877, 2017.

[44] M. F. Imani, J. N. Gollub, O. Yurduseven, A. V. Diebold, M. Boyarsky, T. Fromenteze, L. Pulido-Mancera, T. Sleasman, and D. R. Smith. Review of metasurface antennas for computational microwave imaging. *IEEE Transactions on Antennas and Propagation*, 68(3):1860–1875, 2020.

[45] A. R. Thompson, J. M. Moran, and G. W. Swenson. *Interferometry and Synthesis in Radio Astronomy*. John Wiley and Sons, 2001.

[46] A. Ferretti, C. Prati, and F. Rocca. Permanent scatterers in sar interferometry. *IEEE Transactions on Geoscience and Remote Sensing*, 39(1):8–20, 2001.

[47] K. Schulz, D. Brunner, and M. Boldt. Comparison of covamcoh and ilu image products for interferometric very high resolution sar image pairs. In *2011 IEEE International Geoscience and Remote Sensing Symposium*, pages 313–315, 2011.

[48] J. A. Nanzer. Millimeter-wave interferometric imaging sensors. In *SENSORS, 2013 IEEE*, pages 1–4, Nov 2013.

[49] Y. Álvarez, Y. Rodriguez-Vaqueiro, B. Gonzalez-Valdes, F. Las-Heras, and A. García-Pino. Fourier-based imaging for subsampled multistatic arrays. *IEEE Transactions on Antennas and Propagation*, 64(6):2557–2562, 2016.

[50] D. Soncco, C. Barbanson, M. Nikolova, A. Almansa, and Y. Ferrec. Fast and accurate multiplicative decomposition for fringe removal in interferometric images. *IEEE Transactions on Computational Imaging*, 3(2):187–201, 2017.

[51] E. Kpré, C. Decroze, M. Mouhamadou, and T. Fromenteze. Computational imaging for compressive synthetic aperture interferometric radiometer. *IEEE Transactions on Antennas and Propagation*, 66(10):5546–5557, 2018.

[52] S. Vakalis and J. A. Nanzer. Microwave imaging using noise signals. *IEEE Transactions on Microwave Theory and Techniques*, 66(12):5842–5851, Dec 2018.

[53] S. Vakalis, L. Gong, and J. A. Nanzer. Imaging with wifi. *IEEE Access*, 7:28616–28624, 2019.

[54] S. Vakalis, L. Gong, Y. He, J. Papapolymerou, and J. A. Nanzer. Experimental demonstration and calibration of a 16-element active incoherent millimeter-wave imaging array. *IEEE Transactions on Microwave Theory and Techniques*, pages 1–1, 2020.

[55] C. S. Ruf, C. T. Swift, A. B. Tanner, and D. M. Le Vine. Interferometric synthetic aperture microwave radiometry for the remote sensing of the earth. *IEEE Transactions on Geoscience and Remote Sensing*, 26(5):597–611, Sep. 1988.

[56] F. Zernike. The concept of degree of coherence and its application to optical problems. *Physica*, 5(8):785–795, 1938.

[57] Max Born, Emil Wolf, A. B. Bhatia, P. C. Clemmow, D. Gabor, A. R. Stokes, A. M. Taylor, P. A. Wayman, and W. L. Wilcock. *Principles of Optics: Electromagnetic Theory of Propagation, Interference and Diffraction of Light*. Cambridge University Press, 7 edition, 1999.

[58] T. Amiot, F. Douchin, E. Thouvenot, J. C. Souyris, and B. Cugny. The interferometric cartwheel: a multi-purpose formation of passive radar microsatellites. In *IEEE International Geoscience and Remote Sensing Symposium*, volume 1, pages 435–437 vol.1, 2002.

[59] K. van 't Klooster. A few examples of interferometry applications in space-related active and passive remote sensing. In *2004 Second International Workshop Ultrawideband and Ultrashort Impulse Signals (IEEE Cat. No.04EX925)*, pages 55–58, 2004.

[60] P. Bei and W. Ji. 2-d frequency spectrum features and error analysis for interferometric passive microwave imager. In *2007 International Symposium on Microwave, Antenna, Propagation and EMC Technologies for Wireless Communications*, pages 1454–1457, 2007.

[61] J. A. Nanzer. Spatial filtering of grating lobes in mobile sparse arrays. In *2016 IEEE Radio and Wireless Symposium (RWS)*, pages 26–28, 2016.

[62] P. Chatterjee and J. A. Nanzer. Using platform motion for improved spatial filtering in distributed antenna arrays. In *2018 IEEE Radio and Wireless Symposium (RWS)*, pages 253–255, 2018.

[63] P. C. Theofanopoulos, M. Sakr, and G. C. Trichopoulos. Multistatic terahertz imaging using the radon transform. *IEEE Transactions on Antennas and Propagation*, 67(4):2700–2709, 2019.

[64] A. Moffet. Minimum-redundancy linear arrays. *IEEE Transactions on Antennas and Propagation*, 16(2):172–175, 1968.

[65] Stavros Vakalis, Daniel Chen, and Jeffrey A. Nanzer. Millimeter-wave imaging at 652 frames per second. *IEEE Journal of Microwaves*, pages 1–9, 2021.

[66] Constantine Balanis. *Antenna theory: analysis and design*. Wiley-Interscience, 2016.

[67] Misao Haneishi, Shinichiro Yoshida, and Masashi Tabeta. A design of back-feed type circularly polarized microstrip disk antennas having symmetrical perturbation element by one-point feed. *Electronics and Communications in Japan (Part I: Communications)*, 64(7):52–60, 1981.

[68] S. P. Singh, A. Kumar, V. K. Singh, and Sagar. A broadband wide beamwidth circulary polarized microstrip patch antenna with conformal radome for high-speed airborne communication. In *2017 International Conference on Innovations in Electronics, Signal Processing and Communication (IESC)*, pages 155–158, 2017.

[69] D. Chen, S. Vakalis, V. Holmes, and J. A. Nanzer. Spatial frequency filter design for interferometric image classification without image reconstruction. In *2020 IEEE USNC-CNC-URSI North American Radio Science Meeting (Joint with AP-S Symposium)*, pages 23–24, 2020.

[70] S. M. Ellison, S. Mghabghab, J. J. Doroshewitz, and J. A. Nanzer. Combined wireless ranging and frequency transfer for internode coordination in open-loop coherent distributed antenna arrays. *IEEE Transactions on Microwave Theory and Techniques*, 68(1):277–287, 2020.

[71] H. Ouassal, T. Rocco, M. Yan, and J. A. Nanzer. Decentralized frequency synchronization in distributed antenna arrays with quantized frequency states and directed communications. *IEEE Transactions on Antennas and Propagation*, pages 1–1, 2020.

[72] S. M. Ellison and J. A. Nanzer. High-accuracy multi-node ranging for coherent distributed antenna arrays. *IEEE Transactions on Aerospace and Electronic Systems*, pages 1–1, 2020.

[73] P. Knott. Design and experimental results of a spherical antenna array for a conformal array demonstrator. In *2007 2nd International ITG Conference on Antennas*, pages 120–123, 2007.

[74] G. S. Karthikeya, N. Agnihotri, S. S. Siddiq, K. S. Mehul, and T. Thyagaraj. A conformal uhf antenna for cargo helicopter belly. In *2016 IEEE 5th Asia-Pacific Conference on Antennas and Propagation (APCAP)*, pages 285–286, 2016.

[75] Paul Gerin. Fahlstrom and Thomas J. Gleason. *Introduction to UAV systems*. Wiley, 2012.

[76] http://fettersaerospace.com/uav-helicopters.html, 2017 (accessed June 16, 2020).

[77] Tom Fawcett. An introduction to roc analysis. *Pattern Recognition Letters*, 27(8):861 – 874, 2006. ROC Analysis in Pattern Recognition.

[78] Douglas G Altman and J Martin Bland. Statistics notes: Diagnostic tests 2: predictive values. *BMJ*, 309(6947):102, 1994.

[79] Nicholas Metropolis and S. Ulam. The monte carlo method. *Journal of the American Statistical Association*, 44(247):335–341, 1949.

[80] T. Cover and P. Hart. Nearest neighbor pattern classification. *IEEE Transactions on Information Theory*, 13(1):21–27, 1967.

[81] Richard O. Duda, Peter E. Hart, and David G. Stork. *Pattern Classification*. Wiley, New York, 2 edition, 2001.